A Full Wave Electromagnetic Framework for Optimization and Uncertainty Quantification of Communication Systems in Underground Mine Environments

by
Weitian Sheng

A dissertation submitted in partial fulfillment
of the requirements for the degree of
Doctor of Philosophy
(Electrical Engineering)
in The University of Michigan
2018

Doctoral Committee:

Professor Eric Michielssen, Chair
Professor Anthony Grbic
Professor Robert Krasny
Professor Leung Tsang

Weitian Sheng

wtsheng@umich.edu

ORCID iD: 0000-0002-6193-403X

To My Family and All My Friends,

ACKNOWLEDGMENTS

I would like to first express my gratitude to my advisor, Prof. Eric Michielssen. This work would not have been possible without his constant intellectual, financial and spiritual support. Most importantly, his scientific enthusiasm and sincerity will keep inspiring and guiding me in all aspects of my future life. I would like to thank Professors Anthony Grbic, Robert Krasny, and Leung Tsang for serving on my thesis committee and providing valuable comments on this work. I also would like to thank to Professor Meisong Tong for his mentorship and guidance during my undergrad years. He introduced me into the beautiful world of computational electromagnetics.

Sincere thanks go to Dr. Abdulkadir C. Yücel, Dr. Luis Gomes, Dr. Yang Liu, and Dr. Han Guo for working closely with me on the work presented in this dissertation. Their research work greatly helped me with my research progress and their valuable life experience also enlightened my own choices. I would also like to thank all current and past fellow students I have met in the Radiation Lab. A few of them are: Shuren Tan, Tai Qiao, Huanting Huang, Weihui Gu, Zhanni Wu, Xiuzhang Cai, Menglou Rao, Fatemeh Akbar, Seyed Mohammad Amjadi, Shuo Huang, Morteza Sheikhofla, Peng Tian, Tianlin

Wang, Behzad Yektakhah, Milad Zolfagharloo Koohi, Omar Abdellatty, Chenhui Qu, Jiyue Zhu, etc.

Special thanks go to all my beloved friends accompanying me throughout my PhD. Among them, I would like to thank Pengxiang Jiang and Ziang You for living with me during my first year in the United States and helping me settle down in an entirely new society. I also would like to thank Sihui Han, Xuanhua Zhang, Keke Lyu, Xingtong Zhou, Yifei Li, Qiang Chen, Siyu Wu, and Long Qian for staying with me in our big house and holding our lively parties that swept all the haze away in my second year. Nexy, I would like to thank Shiyang Deng and Xing Chen for their excellent cuisine that prevented me from losing weight during the last two and a half years of my PhD. Meanwhile, I would like to thank Luna Cheung, Lu Shi, Yanyan Xiang, Yali Luo, Lily Li, Tingfang Luo, and Yi Yu for playing with me and listening to me whenever I wanted to share my memorable life moments, or felt bad, and needed suggestions. Finally, I would also like to thank Yuyan Li for encouraging me during my hardest times. Without the warmth of her friendship, I could not overcome the miserable freezing winter in Michigan.

My greatest gratitude goes to my family. Their love, support, and encouragement pulled me back to life whenever I was close to my limit.

TABLE OF CONTENTS

LIST OF FIGURES

LIST OF TABLES

ABSTRACT

Wireless communication, sensing, and tracking systems in mine environments are essential for protecting miners' safety and daily operations. The design, deployment, and post-event reconfiguration of such systems greatly benefits from electromagnetic (EM) frameworks that can statistically analyze and optimize the wireless systems in realistic mine environments. This thesis proposes such a framework by developing two fast and efficient full-wave EM simulators and coupling them with a modern optimization algorithm and an efficient uncertainty quantification (UQ) method to synthesize system configurations and produce statistical insights. The first simulator is a fast multipole method – fast Fourier transform (FMM-FFT) accelerated surface integral equation (SIE) simulator. It relies on Muller and combined fields SIEs to account for scattering from mine walls and conductors, respectively. During the iterative solution of the SIE system, the computational and memory costs are reduced by using the FMM-FFT scheme. The memory costs are further reduced by compressing large data structures via singular value and Tucker decomposition. The second simulator is a domain decomposition (DD)-based SIE simulator. It first divides the physical domain of a mine tunnel or gallery into subdomains and then characterizes EM wave propagation in each subdomain separately. Finally, the DD-based SIE simulator assembles the solutions of subdomains and solves

an inter-domain system using an efficient subdomain-combining scheme. While the DD-based SIE simulator is faster and more memory-efficient than the FMM-FFT accelerated SIE simulator when characterizing EM wave propagation in electrically large mine environments, it does not apply to certain scenarios that the FMM-FFT accelerated SIE simulators can handle. The optimization algorithm and UQ method that are coupled with the EM simulators are the dividing rectangles (DIRECT) algorithm and the high dimensional model representation (HDMR)-enhanced multi-element probabilistic collocation (ME-PC) method, respectively. The DIRECT algorithm is a Lipschitzian optimization method but does not require the knowledge of the Lipschitz constant. It performs a series of moves that explore the behavior of the objective function at a set of points in the carefully picked sub-regions of the search space. The HDMR-enhanced ME-PC method permits the accurate and efficient construction of surrogate models for EM observables in high dimensions. The HDMR expansion expresses the observable as finite sums of component functions that represent independent and combined contributions of random variables to the observable and hence reduces the complexity of UQ by including only the most significant component functions to minimize the computational cost of building the surrogate model. This research numerically validated and verified the two EM simulators and demonstrated the efficiency and applicability of the EM framework via its application to optimization and UQ problems in large and realistic mine environments.

CHAPTER 1
Introduction

1.1 Background

In mining operations, wireless sensing, communication, and tracking systems are essential for planning and conducting routine mining operations, as well as safeguarding miners' health and planning life-saving actions after catastrophic events [1]. The 2006 MINER Act [2] requires operators to implement wireless communication systems capable of surviving disasters and supporting two-way post-event communication and tracking functions. The design and configuration of such systems in mine tunnels and galleries greatly benefit from the use of electromagnetic (EM) frameworks that incorporate EM simulators to optimization algorithms and uncertainty quantification (UQ) methods to provide quantitative data and synthesize system configurations. Ideally, the EM simulator should be able to accurately characterize EM propagation in realistic large-scale mine tunnels with possible internal structures and can be efficiently executed in a repetitive manner. The optimization algorithm should be efficient and robust when used to improve the performance of a wireless communication system. The UQ method should also be able to efficiently and accurately characterize uncertainties in received signal

strength due to conductivities, the presence and positions of miners, and communication and mining equipment. Since mine environments are electrically very large, the optimization algorithm and UQ method incorporated with EM simulators must be able to converge rapidly. Hence, the development of novel EM simulators and careful choices of optimization algorithms and UQ methods are required for the EM framework to efficiently synthesize and statistically analyze practical wireless communication systems in realistic mine environments.

In recent years, various EM simulators based on approximate and full wave techniques have been developed and discussed for analyzing EM wave propagation in mine environments [1]. Frequently-used approximate techniques in these simulators include, but are not limited to, single/multi-mode waveguide models [3, 4], Ray-tracing (or ray optics) methods [5-7], and cascaded-impedance methods [8]. Typically, these methods involve either simplifying assumptions about the physics (e.g. ray optics approximation) or the geometry (e.g. waveguide model) limiting their utility for accurately analyzing wireless communication systems inside complex mine environments. For example, these methods are usually restricted to certain frequency bands and cannot readily account for the presence of wall roughness, unstructured debris, or mine equipment and workers. In contrast, simulators based on full-wave techniques normally do not require simplifying assumptions about the physics or geometries. Full-wave techniques, such as finite-difference-time-domain (FDTD) method [9-12], finite elements method and surface integral equation (SIE) methods [13], can account for all the elements that affect wave propagations inside a tunnel and thus provide a complete and detailed solution for signal transmission information through the mine tunnels or galleries. More

concretely, they can model realistic mine environments that have rough walls and are occupied with conductors, miners and other objects. That said, given large size of tunnels and the high operating frequency, the computational costs for these full-wave simulators are prohibitively expensive and could exceed the capacity of existing computers by orders of magnitude when it comes to statistical characterization and wireless network (re)configurations. As an effort to reduce the computational burden, this research developed a fast multipole method – fast Fourier transform (FMM-FFT) accelerated surface integral equation (SIE) simulator allowing for analyzing mine tunnels and galleries that span more than a thousand meters. This effort is extended further by developing a more computational and memory efficient domain decomposition (DD) based SIE simulator, resulting another novel EM simulator that can analyze realistic and large mine environments.

Optimization algorithms have been long investigated for the design of wireless communication systems. Frequently-used optimization algorithms include stochastic algorithms, gradient based algorithms, and direct search algorithms. Stochastic algorithms, such as genetic algorithm [14] and particle swarm optimization [15], use random variables to search for the optimal value of an objective function. These algorithms typically introduce a number of random ‘seeds’ among the whole searching space and determine the direction and step size for each seed by taking account of current local and/or global best solution. Hence, these algorithms are global optimization algorithms. That said, since they introduce random process during optimization, the results obtained by such algorithms are not deterministic. Moreover, a relative large population of seeds is needed to ensure they can cover the whole searching space and

avoid local optimum, which significantly increase the number of objective function evaluations. Gradient based methods, such as quasi-Newton method [16] and adjoint sensitivity methods [17], require information of the derivatives of objective function to determine the searching direction. They oftentimes are very efficient in terms of the number of objective function evaluations when the objective function is smooth and continuous, but may fail to find the optimum when the derivatives are not available or reliable. Due to the highly unpredictable properties of the objective function (e.g. discontinuity non-differentiability, and noisy) used in the design of wireless systems and the large number of objective function evaluations, the gradient based algorithms and stochastic algorithms are oftentimes not applicable to the proposed framework that uses full wave EM simulators. On the other hand, the direct search algorithms are well suited to finding the optimal placement of wireless devices, since they require only the value of the objective function and are efficient in terms of objective function evaluations. Direct search algorithms determine the searching directions by directly comparing current and past sampling values of objective function. Hence, they are derivative-free and can be applied to objective functions that are discontinuous and non-smooth. Direct search algorithms can be classified as global or local algorithms. Local direct search algorithms, such as Nelder-Mead simplex algorithm [18] and Hooke-Jeeves algorithm [19], are efficient in terms of number of objective function evaluations. However, these local algorithms can be easily trapped by local optima, which exist even in very simple forms of the wireless system optimization problem. In contrast, global direct search algorithms can find the global optimum using a reasonable number of objective function evaluations. DIRECT (DIviding RECTangles) algorithm [20-22] is a well-known global direct search

algorithm. It is a modification of standard Lipschitzian optimization approaches and is widely-used in engineering applications. In this thesis, the DIRECT algorithm is adopted to incorporate with the simulators for the EM framework.

On the other hand, the credibility of EM analyses for communication systems in mine environments is largely affected by uncertain quantities (random variables) in mine's geometry, locations of miners, mining equipment, etc. This dependency must be accurately quantified. The need of UQ is oftentimes met by Monte Carlo (MC) method. However, the MC method requires many deterministic simulations to yield accurate statistical results. Each of these simulations can take minutes to hours, which makes MC method too expensive to incorporate with EM simulators. To reduce the computational cost of MC methods, polynomial chaos (PC) [23] and multi-element probabilistic collocation (ME-PC) method [24] have been developed. These methods first form a polynomial approximation (i.e. surrogate model) of each EM observable as a function of the uncertain parameters by probing the EM simulator. Then, the polynomial surrogate model is used in lieu of the simulator by a MC method for UQ. Evaluating the polynomial requires a relatively small number of computations and hence significant computational savings are observed when compared with MC method. That said, in these methods, a full polynomial to a prescribed order is constructed and the number of simulations required increase exponentially with dimensionality making them of little utility even for moderate dimensional problems. To address this limitation, ME-PC methods have recently been hybridized with high dimensional model representation (HDMR) technique [25]. This technique allows for the generation of a surrogate model in a high dimensional random domain by bootstrapping surrogate models generated in low

dimensional random domains. It iteratively constructs the HDMR surrogate model by only including component functions pertinent to the “most important” random variables, and therefore dramatically reduces the cost of surrogate model construction. The incorporation of this HDMR technique with the proposed EM simulators can allow for more efficient obtaining of the statistics of observables in stochastic EM wave propagation scenarios

1.2 Statement of Purpose

The purpose of this thesis is to present the EM framework that permits fast and efficient stochastic analysis and optimizations of wireless communication networks in large and realistic mine environment. The EM framework contains two novel full wave EM simulators, an efficient UQ method, and a modern optimization algorithm.

First, the FMM-FFT accelerated SIE simulator is introduced. It uses Müller and combined field integral equations (CFIE) to account for scatterings from the mine environments and build well-conditioned system matrix that ensures fast convergence of iterative solutions. It leverages singular value and Tucker decompositions to compress the large data structure required during the FMM-FFT acceleration procedures. Numerical results are presented to show that the compression schemes can boost the FMM-FFT accelerated SIE simulator’s performance and the size of the mine environments it can analyze is extended to more than 1500 wavelengths.

Although the FMM-FFT accelerated SIE simulator is computational and memory efficient, it is restricted to applications requiring small number of excitations. Hence, the

DD based SIE full wave simulator is proposed for efficiently analyzing EM wave propagation in electrically large and realistic mine environments when a large number of excitations exist. It alleviates the computational burden by dividing the physical domain of mine tunnel or gallery into subdomains and characterizes EM wave propagation in each subdomain separately. The final solution is obtained by assembling the solutions of subdomains and solves an inter-domain system using an efficient subdomain combining scheme. The applicability, accuracy, and efficiency of the proposed simulator are demonstrated through its application to the EM wave propagation in an arched tunnel, rectangular tunnels with rough walls and partial cave-in, and a mine gallery and statistical characterization of EM wave propagation in an electrically large rectangular tunnel.

While the DD based SIE simulator is accurate and efficient in many mine environments, it is not ready for certain mine scenarios that contain extended equipment, (e.g. rails and cables), and are overkilling when dealing with small or moderate problems. Hence, the choice of simulator in the EM framework depends on the specific scenario and problem.

The full wave simulators are then incorporated to the DIRECT optimization algorithm to form the optimization part of the EM framework. The objective of the optimization is to find optimal placement of the wireless transmitters that maximizes an objective function that measures key desirable performance such as signal coverage, subject to a given set of fixed receiver locations and certain physical constraints on where the transmitters may be placed. The applicability and efficiency of this framework in optimization problems are demonstrated via wireless network optimizations or reconfigurations in several realistic mine galleries.

Furthermore, these two full wave simulators are incorporated to the ME-PC enhanced HDMR method to form the UQ part of the EM framework. This HDMR method is finely tuned to EM applications by hybridizing the HDMR method with the expansion of partial fractions, coefficients of which are obtained by well-known vector fitting algorithm. The proposed framework is applied to the UQ of several real-world communication systems commonly used in the mine environments, including leaky feeder systems, through-the-earth systems, medium frequency radio systems, and wireless node-based mesh networks.

1.3 Organization of Chapters

The remainder of this thesis is organized as follows. Chapter 2 presents the formulation of the FMM-FFT accelerated SIE simulator for analyzing EM propagation inside electrically large realistic mine tunnels and galleries. The Muller and CFIE formulations, FMM-FFT acceleration scheme, singular value and Tucker decompositions, and parallel schemes are detailed in this chapter. The simulator is validated through characterization of EM wave propagation in electrically large mine tunnels/galleries loaded with conducting cables and mine carts. Chapter 3 describes the proposed DD based SIE simulator. The DD approach and its modification to high-loss mine environments are introduced. The accuracy and its applicability of the DD based SIE simulator is demonstrated via examples in various mine layouts. Its computational cost and memory footprint compared to those of FMM-FFT accelerated SIE simulators. In Chapter 4, the DIRECT algorithm is detailed. This chapter first introduces the standard

Lipschitzian optimization and then modifies it towards the DIRECT algorithm. The algorithm is then incorporated with the EM simulators for optimization or reconfiguration of wireless communication systems in various mine environments. Chapter 5 introduces the HDMR enhanced ME-PC method and applies it to several communication systems employed in mine environments. In chapter 6, the DD based SIE simulator is further improved by the hierarchical off-diagonal butterfly factorization (HODBF) scheme. This chapter presents the detail of HODBF scheme and demonstrates the efficiency of the HODBF compressed DD based SIE simulator via electrically very large examples. Finally, conclusions, ongoing studies, and list of publications related to this thesis are outlined in Chapter 7.

CHAPTER 2
A FMM-FFT Accelerated SIE Simulator for Analyzing EM Wave Propagation in Mine Environments Loaded with Conductors

2.1 Chapter Introduction

Reliable wireless communication, sensing, and tracking systems in underground mine environments are critically important to ensure workers' safety and productivity during routine operations and catastrophic events. As mandated by the MINER Act of 2006 [2], U.S. mine operators are required to install reliable and disaster-proof communication systems that support two-way post-event communication and tracking functions. The development, operation, and reconfiguration of these systems, as well as the mitigation of possible electromagnetic compatibility and interference issues associated with their deployment, all benefit from electromagnetic (EM) simulation tools. These tools should be capable of analyzing EM wave propagation in mine tunnels and galleries that are loaded with conductors (e.g., lighting/power cables, mine carts, mining machinery, rails, ventilation systems), occupied by miners, and possibly obstructed by cave-in debris. Present simulation techniques for analyzing EM wave propagation in

mine environments are either approximate or full-wave in nature. Examples of approximate techniques include, but are not limited to, s single/multi-mode waveguide models [3, 4], ray-tracing techniques [5-7], and cascaded-impedance methods [8]; For other approximate techniques, see [26] and references therein. For other approximate techniques, see [1] and references therein. The above-referenced techniques typically only apply to EM characterization in restricted frequency bands and do not readily account for the presence of conductors and miners, wall roughness (especially when comparable to the wavelength), or unstructured debris. Full-wave techniques for analyzing EM wave propagation in mine environments include finite difference time domain (FDTD) [9-12] and surface integral equation (SIE) methods [13]. In principle, these techniques permit faithful modeling of EM wave propagation in real-world mine environments. However, in practice, due to their high computational requirements, their applicability is limited to the study of EM wave propagation in electrically small or moderately sized tunnels even when they are implemented on graphics processing units (GPUs) [9]. This chapter presents a fast, full-wave, CPU and memory-efficient 3D SIE technique for analyzing EM wave propagation in electrically large and realistically loaded mine environments. The technique leverages Muller and combined field SIEs to model scattering from mine walls and perfect electrically conducting (PEC) objects residing inside mine tunnels and galleries. The naive iterative solution of such SIEs requires $O(N^2)$ CPU and memory resources. Here N is the number of basis functions used to discretize current densities on the mine walls and PEC objects. These requirements are prohibitive even when characterizing moderately sized tunnels and

galleries. Therefore, the proposed simulator leverages a fast multipole method – fast Fourier transform (FMM-FFT) acceleration scheme [27] with $O(N^{4/3}\log^{2/3} N)$ CPU and memory resources [28] when applied to mine environments of arbitrary layout, and $O(N \log N)$ resources when applied to straight long tunnels or mine galleries populated with dense posts [27]. When applied to the analysis of EM propagation in mine environments, FMM-FFT accelerated SIE simulators tend to be memory- as opposed to CPU-limited. The simulators' memory requirements derive from the requirement to store (i) near-field interaction matrices, (ii) matrices that characterize far-field signatures of basis functions, and (iii) tensors that hold FFT'ed translation operators on a structured grid. The proposed simulator compresses the first two and third data structures via singular value decomposition (SVD) and its higher-dimensional counterpart, Tucker decomposition [29], respectively. These compression schemes enable the application of the FMM-FFT accelerated SIE simulator to the analysis of EM wave propagation in much larger and complex mine environments. The chapter's contributions are two-fold. (i) It describes the first-ever application of a fast SIE simulator to the characterization of EM wave propagation in electrically large and realistically loaded mine environments. (ii) It proposes a scheme, which compresses all large data structures of the FMM-FFT accelerated SIE simulator, to reduce its memory requirement and enable its application to larger scale problems on memory-bound computer clusters. The accuracy, efficiency, and applicability of the proposed simulator are demonstrated via the analysis of EM wave propagation in a 600 m-long arched tunnel loaded with conductors, a mine gallery consisting of eight rectangular tunnels, and a rectangular tunnel with rough walls.

2.2 Formulation

This section details the Muller and combined field SIEs and their numerical solution via the method of moments (MoM). It also elucidates the proposed SVD and Tucker-enhanced FMM-FFT acceleration scheme.

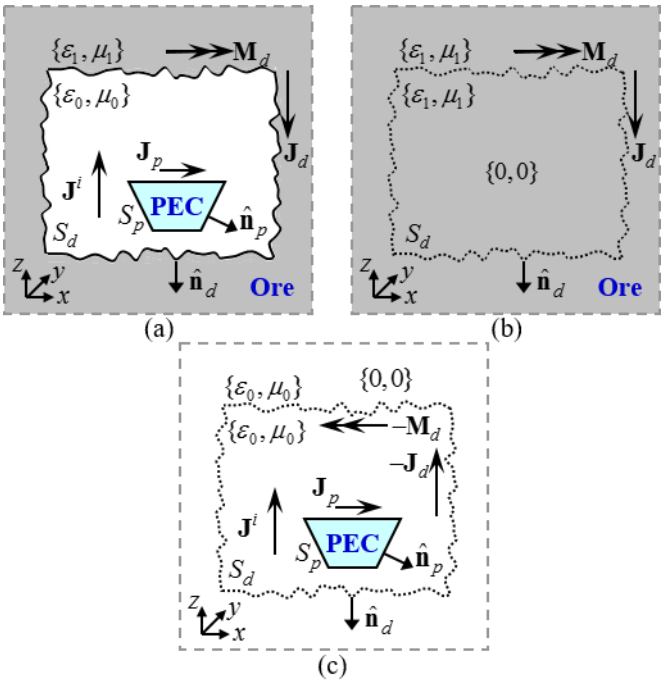

Figure 2.1 (a) Generic tunnel geometry for Muller-combined field SIE formulation. (a) Original problem. (b) Equivalent exterior problem. (c) Equivalent interior problem.

2.2.1 SIEs and Their Discretization

Let S_d denote the walls of a closed mine tunnel or gallery, which is surrounded by unbounded lossy ore with permittivity ε_1 and permeability μ_1 (medium 1). The tunnel or gallery is assumed to be filled by air with permittivity ε_0 and permeability μ_0 (medium 0) [Figure 2.1 (a)]. (Note: the scheme detailed below can be trivially modified for tunnels and galleries filled by dust with permittivity different from ε_0) Let S_p

represent the arbitrarily shaped open or closed surfaces of PEC objects (e.g., mine carts, cables, or other equipment) residing inside S_d. S_d and S_p are excited by the incident EM field $\{\mathbf{E}^i(\mathbf{r}),\mathbf{H}^i(\mathbf{r})\}$ that is generated by a transmitter's electric current density $\mathbf{J}^i(\mathbf{r})$ (e.g., an electric dipole) residing within S_d [Figure 2.1 (a)]. The interaction of $\{\mathbf{E}^i(\mathbf{r}),\mathbf{H}^i(\mathbf{r})\}$ with S_d and S_p gives rise to electric and magnetic current densities, $\mathbf{J}_d(\mathbf{r})$ and $\mathbf{M}_d(\mathbf{r})$ on S_d and electric current densities $\mathbf{J}_p(\mathbf{r})$ on S_p.

To compute $\mathbf{J}_d(\mathbf{r})$, $\mathbf{M}_d(\mathbf{r})$, and $\mathbf{J}_p(\mathbf{r})$, the surface equivalence principle is invoked to construct the exterior and interior problems illustrated in Figure 2.1 (b)-(c). In the exterior problem [Figure 2.1 (b)], $\mathbf{J}_d(\mathbf{r})$ and $\mathbf{M}_d(\mathbf{r})$ radiate in medium 1 and generate total and zero electric and magnetic fields exterior and interior to S_d, respectively. Imposing boundary conditions on the tangential components of electric and magnetic fields on S_d yields the following exterior electric field integral equation (EFIE) and magnetic field integral equation (MFIE):

$$\Re_a\left[\mathbf{X}(\mathbf{r})\right] = \nabla\times\int_S \mathbf{X}(\mathbf{r}')G_a(\mathbf{r},\mathbf{r}')\,d\mathbf{r}', \tag{2.1}$$

$$0 = \hat{\mathbf{n}}_d\times\Im_1\left[\mathbf{M}_d(\mathbf{r})\right]/\eta_1^2 + \left(-0.5\mathbf{J}_d(\mathbf{r}) + \hat{\mathbf{n}}_d\times\Re_1\left[\mathbf{J}_d(\mathbf{r})\right]\right), \tag{2.2}$$

$\mathbf{r}\in S_d$. Here, $\hat{\mathbf{n}}_d$ is the outward normal to S_d, $\eta_a=(\mu_a/\varepsilon_a)^{0.5}$ with $a\in\{0,1\}$ is the wave impedance, and the source-field operators $\Im_a[\cdot]$ and $\Re_a[\cdot]$ are

$$\Im_a\left[\mathbf{X}(\mathbf{r})\right] = -j\omega\mu_a\int_S(\bar{\mathbf{I}}+\frac{\nabla\nabla'}{k_a^2})\cdot\mathbf{X}(\mathbf{r}')G_a(\mathbf{r},\mathbf{r}')\,d\mathbf{r}', \tag{2.3}$$

$$\Re_a\left[\mathbf{X}(\mathbf{r})\right] = \nabla \times \int_S \mathbf{X}(\mathbf{r}') G_a(\mathbf{r},\mathbf{r}')\, d\mathbf{r}' \ , \tag{2.4}$$

where the integral in (2.4) is evaluated in principal value sense. Here $G_a(\mathbf{r},\mathbf{r}') = \exp(-jk_a\,|\mathbf{r}-\mathbf{r}'|)/(4\pi\,|\mathbf{r}-\mathbf{r}'|)$ is the scalar Green's function, $k_a = \omega(\mu_a\varepsilon_a)^{0.5}$, $\omega = 2\pi f$, f is the frequency, and $\mathbf{r}$ and $\mathbf{r}'$ denote observation and source locations on support S, respectively.

In the interior problem [Figure 2.1 (c)], $-\mathbf{J}_d(\mathbf{r})$ and $-\mathbf{M}_d(\mathbf{r})$ radiate alongside $\mathbf{J}^i(\mathbf{r})$ and $\mathbf{J}_p(\mathbf{r})$ in air and generate total and zero electric and magnetic fields interior and exterior to S_d, respectively. Imposing boundary conditions for tangential electric and magnetic fields on S_d and S_p yields the following interior EFIE and MFIE for S_d and interior EFIE and MFIE for S_p :

$$\begin{aligned}\hat{\mathbf{n}}_d \times \mathbf{E}^i(\mathbf{r}) = &-\left(0.5\mathbf{M}_d(\mathbf{r}) + \hat{\mathbf{n}}_d \times \Re_0\left[\mathbf{M}_d(\mathbf{r})\right]\right) \\ &+ \hat{\mathbf{n}}_d \times \Im_0\left[\mathbf{J}_d(\mathbf{r})\right] - \hat{\mathbf{n}}_d \times \Im_0\left[\mathbf{J}_p(\mathbf{r})\right], \quad \mathbf{r} \in S_d\end{aligned} \tag{2.5}$$

$$\begin{aligned}\hat{\mathbf{n}}_d \times \mathbf{H}^i(\mathbf{r}) = \hat{\mathbf{n}}_d \times \Im_0\left[\mathbf{M}_d(\mathbf{r})\right]/\eta_0^2 + \left(0.5\mathbf{J}_d(\mathbf{r}) + \right. \\ \left. \hat{\mathbf{n}}_d \times \Re_0\left[\mathbf{J}_d(\mathbf{r})\right]\right) - \hat{\mathbf{n}}_d \times \Re_0\left[\mathbf{J}_p(\mathbf{r})\right], \quad \mathbf{r} \in S_d\end{aligned} \tag{2.6}$$

$$\hat{\mathbf{t}}_p \cdot \mathbf{E}^i(\mathbf{r}) = \hat{\mathbf{t}}_p \cdot \left(-\Re_0\left[\mathbf{M}_d(\mathbf{r})\right] + \Im_0\left[\mathbf{J}_d(\mathbf{r})\right] - \Im_0\left[\mathbf{J}_p(\mathbf{r})\right]\right), \quad \mathbf{r} \in S_p \tag{2.7}$$

$$\begin{aligned}\hat{\mathbf{n}}_p \times \eta_0 \mathbf{H}^i(\mathbf{r}) = \hat{\mathbf{n}}_p \times \Im_0\left[\mathbf{M}_d(\mathbf{r})\right]/\eta_0 + \hat{\mathbf{n}}_p \times \eta_0 \Re_0\left[\mathbf{J}_d(\mathbf{r})\right] \\ + \eta_0\left(0.5\mathbf{J}_p(\mathbf{r}) - \hat{\mathbf{n}}_p \times \Re_0\left[\mathbf{J}_p(\mathbf{r})\right]\right), \quad \mathbf{r} \in S_p\end{aligned} \tag{2.8}$$

Here $\hat{\mathbf{n}}_p$ and $\hat{\mathbf{t}}_p$ are the outward pointing unit normal and arbitrary unit vector tangential to S_p, respectively. Exterior and interior EFIEs for S_d in (2.1) and (2.5) can be linearly combined after multiplying them by α_1 and α_0, respectively, as

$$\begin{aligned}\hat{\mathbf{n}}_d \times \alpha_0 \mathbf{E}^i(\mathbf{r}) = 0.5(\alpha_1 - \alpha_0)\mathbf{M}_d(\mathbf{r}) - \hat{\mathbf{n}}_d \times \left(\alpha_1 \Re_1\left[\mathbf{M}_d(\mathbf{r})\right] + \alpha_0 \Re_0\left[\mathbf{M}_d(\mathbf{r})\right]\right) \\ + \hat{\mathbf{n}}_d \times \left(\alpha_1 \Im_1\left[\mathbf{J}_d(\mathbf{r})\right] + \alpha_0 \Im_0\left[\mathbf{J}_d(\mathbf{r})\right]\right) - \hat{\mathbf{n}}_d \times \alpha_0 \Im_0\left[\mathbf{J}_p(\mathbf{r})\right].\end{aligned} \tag{2.9}$$

Similarly, exterior and interior MFIEs for S_d can be multiplied by β_1 and β_0, respectively, and combined as

$$\begin{aligned}\hat{\mathbf{n}}_d \times \beta_0 \mathbf{H}^i(\mathbf{r}) = \hat{\mathbf{n}}_d \times \left(\frac{\beta_1}{\eta_1^2} \Im_1\left[\mathbf{M}_d(\mathbf{r})\right] + \frac{\beta_0}{\eta_0^2} \Im_0\left[\mathbf{M}_d(\mathbf{r})\right]\right) + 0.5(\beta_0 - \beta_1)\mathbf{J}_d(\mathbf{r}) \\ + \hat{\mathbf{n}}_d \times \left(\beta_1 \Re_1\left[\mathbf{J}_d(\mathbf{r})\right] + \beta_0 \Re_0\left[\mathbf{J}_d(\mathbf{r})\right]\right) - \hat{\mathbf{n}}_d \times \beta_0 \Re_0\left[\mathbf{J}_p(\mathbf{r})\right].\end{aligned} \tag{2.10}$$

Finally, linearly combining the α_p times interior EFIE and $(1-\alpha_p)$ times interior MFIE for S_p yields

$$\begin{aligned}\hat{\mathbf{t}}_p \cdot \alpha_p \mathbf{E}^i(\mathbf{r}) + \hat{\mathbf{n}}_p \times \eta_0 (1-\alpha_p)\mathbf{H}^i(\mathbf{r}) = \left(-\hat{\mathbf{t}}_p \cdot \alpha_p \Re_0\left[\mathbf{M}_d(\mathbf{r})\right]\right. \\ + \hat{\mathbf{n}}_p \times (1-\alpha_p)/\eta_0 \, \Im_0\left[\mathbf{M}_d(\mathbf{r})\right]\Big) + \left(\hat{\mathbf{t}}_p \cdot \alpha_p \Im_0\left[\mathbf{J}_d(\mathbf{r})\right] + \hat{\mathbf{n}}_p \times \eta_0 (1-\alpha_p)\Re_0\left[\mathbf{J}_d(\mathbf{r})\right]\right) \\ + \left(-\hat{\mathbf{t}}_p \cdot \alpha_p \Im_0\left[\mathbf{J}_p(\mathbf{r})\right] + \eta_0 (1-\alpha_p)\left(0.5\mathbf{J}_p(\mathbf{r}) - \hat{\mathbf{n}}_p \times \Re_0\left[\mathbf{J}_p(\mathbf{r})\right]\right)\right).\end{aligned} \tag{2.11}$$

Equations (2.9)-(2.11) with $\alpha_1 = \varepsilon_1$, $\alpha_0 = -\varepsilon_0$, $\beta_1 = \mu_1$, $\beta_0 = -\mu_0$, and $0 \le \alpha_p \le 1$ are known as Muller-combined field SIE formulation [30] and can be solved simultaneously for $\mathbf{M}_d(\mathbf{r})$, $\mathbf{J}_d(\mathbf{r})$, and $\mathbf{J}_p(\mathbf{r})$ via the MoM. (Note: In this study, α_p is set to 0.2 and 1

for closed and open PEC surfaces, respectively.) To this end, $\mathbf{M}_d(\mathbf{r})$, $\mathbf{J}_d(\mathbf{r})$, and $\mathbf{J}_p(\mathbf{r})$ are approximated in terms of Rao-Wilton-Glisson (RWG) basis functions $\mathbf{f}_n(\mathbf{r})$ [31] as

$$\mathbf{M}_d(\mathbf{r}) = \sum_{n=1}^{N_d} I_n \mathbf{f}_n(\mathbf{r}), \qquad \mathbf{J}_d(\mathbf{r}) = \sum_{n=N_d+1}^{2N_d} I_n \mathbf{f}_n(\mathbf{r}) \tag{2.12}$$

$$\mathbf{J}_p(\mathbf{r}) = \sum_{n=2N_d+1}^{2N_d+N_p} I_n \mathbf{f}_n(\mathbf{r}) \tag{2.13}$$

where I_n, $n=1,\ldots,2N_d+N_p$, are unknown expansion coefficients. Substituting (2.12) and (2.13) into (2.9)-(2.11) and applying Galerkin testing to the resulting equations with $\mathbf{f}_m(\mathbf{r})$, $m=1,\ldots,2N_d+N_p$, yields the linear system of equations of dimension $N=2N_d+N_p$:

$$\bar{\mathbf{Z}}\mathbf{I} = \mathbf{V} \tag{2.14}$$

where $\bar{\mathbf{Z}}$ is the MoM matrix, and $\mathbf{I}$ and $\mathbf{V}$ are vectors of unknown expansion coefficients and tested incident EM fields, respectively. The entries of $\mathbf{I}$, I_n, $n=1,\ldots,N$, as well as those of $\bar{\mathbf{Z}}$ and $\mathbf{V}$ are provided in Section 2.2.2.

When analyzing electrically large mine tunnels and galleries loaded with conductors that require large N, the solution of the matrix system in (2.14) cannot be obtained using classical algebraic solvers. To mitigate the computational and memory requirements of the iterative solution of (2.14), we deploy the SVD and Tucker enhanced FMM-FFT scheme described next.

2.2.2 Entries of Equation 2.14

The entries of the unknown expansion coefficient vector $\mathbf{I}$ are simply I_n, $n=1,\ldots,2N_d+N_p$. The entries of the tested incident field vector $\mathbf{V}$ are

$$\mathbf{V}_m=\begin{cases}\left\langle \mathbf{f}_m(\mathbf{r}),\alpha_0\hat{\mathbf{n}}_d\times\mathbf{E}^i(\mathbf{r})\right\rangle_{S_d} & 1\le m\le N_d \\ \left\langle \mathbf{f}_m(\mathbf{r}),\beta_0\hat{\mathbf{n}}_d\times\mathbf{H}^i(\mathbf{r})\right\rangle_{S_d} & N_d+1\le m\le 2N_d \\ \left\langle \mathbf{f}_m(\mathbf{r}),\alpha_p\hat{\mathbf{t}}_p\cdot\mathbf{E}^i(\mathbf{r})\right\rangle_{S_p} & 2N_d+1\le m\le N \\ +\left\langle \mathbf{f}_m(\mathbf{r}),\eta_0\left(1-\alpha_p\right)\hat{\mathbf{n}}_p\times\mathbf{H}^i(\mathbf{r})\right\rangle_{S_p} & \end{cases} \tag{2.15}$$

where $\left\langle \mathbf{a}(\mathbf{r}),\mathbf{b}(\mathbf{r})\right\rangle_S=\int_S \mathbf{a}(\mathbf{r})\cdot\mathbf{b}(\mathbf{r})d\mathbf{r}$. The entries of the MoM matrix $\bar{\mathbf{Z}}$ are

$$\bar{\mathbf{Z}}_{mn}=0.5(\alpha_1-\alpha_0)\left\langle \mathbf{f}_m(\mathbf{r}),\mathbf{f}_n(\mathbf{r})\right\rangle_{S_d}+\left\langle \hat{\mathbf{n}}_d\times\mathbf{f}_m(\mathbf{r}),(\alpha_1\Re_1+\alpha_0\Re_0)\left[\mathbf{f}_n(\mathbf{r})\right]\right\rangle_{S_d} \tag{2.16}$$
$$1\le m\le N_d,\,1\le n\le N_d$$

$$\bar{\mathbf{Z}}_{mn}=-\left\langle \hat{\mathbf{n}}_d\times\mathbf{f}_m(\mathbf{r}),(\alpha_1\Im_1+\alpha_0\Im_0)\left[\mathbf{f}_n(\mathbf{r})\right]\right\rangle_{S_d} \tag{2.17}$$
$$1\le m\le N_d,\,N_d+1\le n\le 2N_d$$

$$\bar{\mathbf{Z}}_{mn}=\left\langle \hat{\mathbf{n}}_d\times\mathbf{f}_m(\mathbf{r}),\alpha_0\Im_0\left[\mathbf{f}_n(\mathbf{r})\right]\right\rangle_{S_d} \tag{2.18}$$
$$1\le m\le N_d,\,2N_d+1\le n\le N$$

$$\bar{\mathbf{Z}}_{mn}=-\left\langle \hat{\mathbf{n}}_d\times\mathbf{f}_m(\mathbf{r}),(\frac{\beta_1}{\eta_1^2}\Im_1+\frac{\beta_0}{\eta_0^2}\Im_0)\left[\mathbf{f}_n(\mathbf{r})\right]\right\rangle_{S_d} \tag{2.19}$$
$$N_d+1\le m\le 2N_d,\,1\le n\le N_d$$

$$\bar{\mathbf{Z}}_{mn}=0.5(\beta_0-\beta_1)\left\langle \mathbf{f}_m(\mathbf{r}),\mathbf{f}_n(\mathbf{r})\right\rangle_{S_d}-\left\langle \hat{\mathbf{n}}_d\times\mathbf{f}_m(\mathbf{r}),(\beta_1\Re_1+\beta_0\Re_0)\left[\mathbf{f}_n(\mathbf{r})\right]\right\rangle_{S_d} \tag{2.20}$$
$$N_d+1\le m\le 2N_d,\,N_d+1\le n\le 2N_d$$

$$\bar{\mathbf{Z}}_{mn} = \left\langle \hat{\mathbf{n}}_d \times \mathbf{f}_m(\mathbf{r}), \beta_0 \Re_0 \left[\mathbf{f}_n(\mathbf{r}) \right] \right\rangle_{S_d}$$
$$N_d + 1 \le m \le 2N_d,\ 2N_d + 1 \le n \le N \tag{2.21}$$

$$\bar{\mathbf{Z}}_{mn} = \left\langle \mathbf{f}_m(\mathbf{r}), -\hat{\mathbf{t}}_p \cdot \alpha_p \Re_0 \left[\mathbf{f}_n(\mathbf{r}) \right] \right\rangle_{S_p} - \left\langle \hat{\mathbf{n}}_p \times \mathbf{f}_m(\mathbf{r}), \left(1-\alpha_p\right) / \eta_0 \, \Im_0 \left[\mathbf{f}_n(\mathbf{r}) \right] \right\rangle_{S_p}$$
$$2N_d + 1 \le m \le N, 1 \le n \le N_d \tag{2.22}$$

$$\bar{\mathbf{Z}}_{mn} = \left\langle \mathbf{f}_m(\mathbf{r}), \hat{\mathbf{t}}_p \cdot \alpha_p \Im_0 \left[\mathbf{f}_n(\mathbf{r}) \right] \right\rangle_{S_p} - \left\langle \hat{\mathbf{n}}_p \times \mathbf{f}_m(\mathbf{r}), \eta_0 \left(1-\alpha_p\right) \Re_0 \left[\mathbf{f}_n(\mathbf{r}) \right] \right\rangle_{S_p}$$
$$2N_d + 1 \le m \le N,\ N_d + 1 \le n \le 2N_d \tag{2.23}$$

$$\begin{aligned} \bar{\mathbf{Z}}_{mn} &= \left\langle \mathbf{f}_m(\mathbf{r}), -\hat{\mathbf{t}}_p \cdot \alpha_p \Im_0 \left[\mathbf{f}_n(\mathbf{r}) \right] \right\rangle_{S_p} \\ &\quad + \eta_0 \left(1-\alpha_p\right) \left(0.5 \left\langle \mathbf{f}_m(\mathbf{r}), \mathbf{f}_n(\mathbf{r}) \right\rangle_{S_p} + \left\langle \hat{\mathbf{n}}_p \times \mathbf{f}_m(\mathbf{r}), \Re_0 \left[\mathbf{f}_n(\mathbf{r}) \right] \right\rangle_{S_p} \right) \end{aligned}$$
$$2N_d + 1 \le m \le N,\ 2N_d + 1 \le n \le N \tag{2.24}$$

2.2.3 SVD and Tucker Enhanced FMM-FFT Algorithm

2.2.3.1 FMM-FFT Algorithm

FMM-FFT scheme introduces a hypothetical box enclosing the mesh of S_d (and hence S_p). This large box is split into N_x, N_y, and N_z smaller boxes along the x, y, and z directions [Figure 2.2]. The resulting boxes are denoted by $B_{\mathbf{u}}$ with indices $\mathbf{u}=(u_x,u_y,u_z)$, $u_x=1,\ldots,N_x$, $u_y=1,\ldots,N_y$, $u_z=1,\ldots,N_z$, and centered at $\mathbf{r}_{\mathbf{u}}$ that coincide with the points of a uniform 3D grid [Figure 2.2].

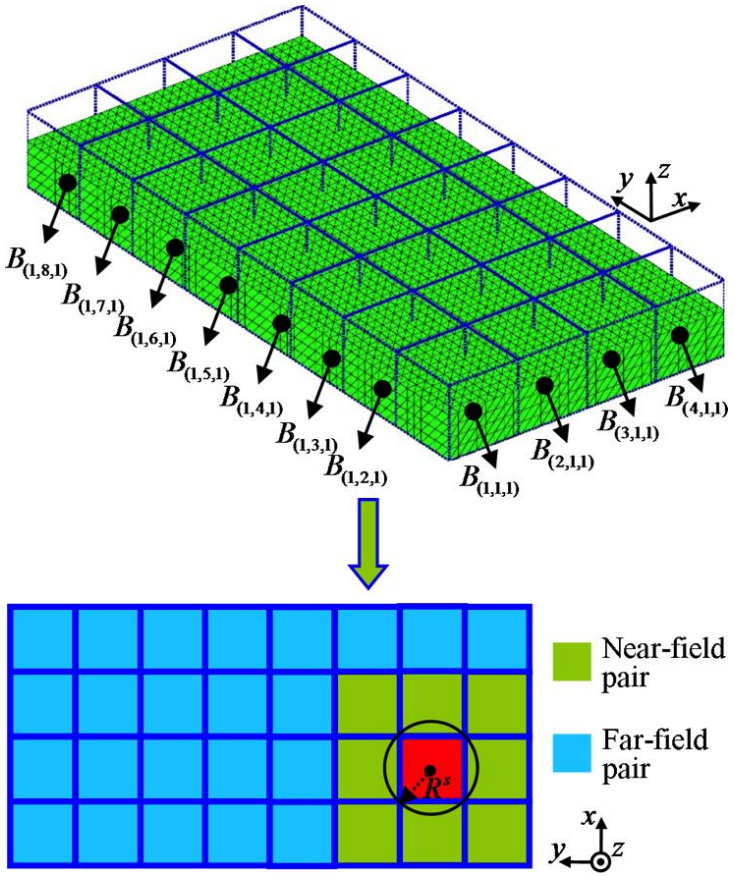

Figure 2.2 Partitioning a fictitious box enclosing the mesh of an example structure into small boxes and tabulating near/far-field pairs of a selected group $B_{(2,2,1)}$ in FMM-FFT scheme.

All boxes that contain triangle pairs of source/testing basis functions, $\mathbf{f}_n(\mathbf{r})/\mathbf{f}_m(\mathbf{r})$, are termed "groups" and enclosed by a sphere of radius R^s. Two groups $B_{\mathbf{u}}$ and $B_{\mathbf{u}'}$ constitute a near-field pair if the distance between their centers $R_{\mathbf{u}'\mathbf{u}}=|\mathbf{R}_{\mathbf{u}'\mathbf{u}}|=|\mathbf{r}_{\mathbf{u}'}-\mathbf{r}_{\mathbf{u}}|$ is smaller than a prescribed threshold, i.e. $R_{\mathbf{u}'\mathbf{u}}<\kappa R^s$ (κ is selected as 4 in this study); otherwise, they form a far-field pair [Figure 2.2]. Interactions between basis functions in the same group and near-field pairs are directly computed and stored, resulting in the first large data structure mentioned in the introduction. A large portion of this data structure is

pertinent to interactions between basis functions in near-field pairs and compressed by SVD, as elucidated in the next subsection. The contributions of self and near-field interactions to the result of each matrix-vector multiplication required by the iterative solution of (2.14) are directly computed. The interactions between basis functions in far-field pairs are computed by the FMM-FFT algorithm. To this end, first, the far-field patterns of source basis functions $\mathbf{P}^{+}(\hat{\mathbf{k}}_a^{pq}, \mathbf{f}_n)$ with

$$\mathbf{P}^{\pm}(\hat{\mathbf{k}}_a^{pq}, \mathbf{c}) = \int_{S_c} \exp(\pm jk_a \hat{\mathbf{k}}_a^{pq} \cdot (\mathbf{r} - \mathbf{r}_\mathbf{u}))(\bar{\mathbf{I}} - \hat{\mathbf{k}}_a^{pq} \hat{\mathbf{k}}_a^{pq}) \cdot \mathbf{c}(\mathbf{r}) d\mathbf{r} \tag{2.25}$$

are computed and stored for all directions $\hat{\mathbf{k}}_a^{pq} = (\sin\theta^p \cos\phi^q, \sin\theta^p \sin\phi^q, \cos\theta^p)$, $p = 1, \ldots, K_a + 1$, $q = 1, \ldots, 2K_a + 1$. Here, θ^p are the inverse cosine of abscissas of $(K_a + 1)^{\text{th}}-$ order Gauss-Legendre quadrature rule, $\phi^q = q2\pi/(2K_a + 1)$, $K_a = 2k_a R^s + 1.8(\log_{10}(1/\gamma_1))^{2/3}(2k_a R^s)^{1/3}$ is the number of multipoles for medium $a = \{0,1\}$, γ_1 is the number of desired accurate digits in the FMM approximation [32], S_c is the support of $\mathbf{c}(\mathbf{r})$, and $\mathbf{u}$ corresponds to the box containing $\mathbf{c}(\mathbf{r})$. Since $\bar{\mathbf{I}}$ is unit dyad and $\bar{\mathbf{I}} - \hat{\mathbf{k}}_a^{pq} \hat{\mathbf{k}}_a^{pq} = \hat{\boldsymbol{\theta}}\hat{\boldsymbol{\theta}} + \hat{\boldsymbol{\varphi}}\hat{\boldsymbol{\varphi}}$, θ and ϕ components of far-field patterns are computed [32]. Note that only the far-field patterns of source basis functions discretizing $\mathbf{J}_d(\mathbf{r})$ and $\mathbf{J}_p(\mathbf{r})$ are computed and stored for both media and only air (medium 0), respectively; the ones pertinent to $\mathbf{M}_d(\mathbf{r})$ can be directly obtained from those related to $\mathbf{J}_d(\mathbf{r})$ by invoking the duality and thereby are not stored. Similarly, the receiving patterns of testing functions used to test electric and magnetic fields on S_d, $\mathbf{P}^{-}(\hat{\mathbf{k}}_a^{pq}, \hat{\mathbf{n}}_d \times \mathbf{f}_m)$, and

electric and magnetic fields on S_p, $\mathbf{P}^-(\hat{\mathbf{k}}_a^{pq}, \mathbf{f}_m)$ and $\mathbf{P}^-(\hat{\mathbf{k}}_a^{pq}, \hat{\mathbf{n}}_p \times \mathbf{f}_m)$, are computed and stored for both media and only air, respectively. These operations give rise to the second large data structure alluded to in the introduction, which is compressed by SVD as explained in the next subsection. During matrix-vector multiplication, the far-fields of basis functions in each group are summed to construct all groups' outgoing far-field patterns for both media as

$$\mathcal{F}_{\mathbf{u}}(\hat{\mathbf{k}}_a^{pq}) = \sum\nolimits_{n \in B_{\mathbf{u}}} \mathbf{P}^+(\hat{\mathbf{k}}_a^{pq}, \mathbf{f}_n) \alpha_a c I_n \,, \tag{2.26}$$

$p = 1, \ldots, K_a + 1$, $q = 1, \ldots, 2K_a + 1$, $a \in \{0,1\}$. Here c is -1 for far-field patterns of basis functions used to discretize $\mathbf{J}_p(\mathbf{r})$ and 1 otherwise. (Note: far-field patterns of basis functions discretizing $\mathbf{J}_p(\mathbf{r})$ are not computed/stored for medium 1 and not included in summation in (2.26) for $a = 1$.) Next, for each $\hat{\mathbf{k}}_a^{pq}$, these far-field patterns $\mathcal{F}_{\mathbf{u}}(\hat{\mathbf{k}}_a^{pq})$ are convolved via FFT with the translation tensor $\mathcal{T}_{\mathbf{u}'-\mathbf{u}}^{\sim}(\hat{\mathbf{k}}_a^{pq})$ to obtain all groups' incoming plane wave spectra $\mathcal{G}_{\mathbf{u}'}(\hat{\mathbf{k}}_a^{pq})$ as

$$\mathcal{G}_{\mathbf{u}'}(\hat{\mathbf{k}}_a^{pq}) = \Psi^{-1}(\mathcal{T}_{\mathbf{u}'-\mathbf{u}}(\hat{\mathbf{k}}_a^{pq}) \Psi(\mathcal{F}_{\mathbf{u}}(\hat{\mathbf{k}}_a^{pq}))) \,. \tag{2.27}$$

Here Ψ is the FFT operator, $\mathcal{T}_{\mathbf{u}'-\mathbf{u}}(\hat{\mathbf{k}}_a^{pq}) = \Psi(\mathcal{T}_{\mathbf{u}'-\mathbf{u}}^{\sim}(\hat{\mathbf{k}}_a^{pq}))$ is the tensor that stores *FFT'ed* translation operator values and

$$\mathcal{T}_{\mathbf{u}'-\mathbf{u}}^{\sim}(\hat{\mathbf{k}}_a^{pq}) = \frac{k_a^2 \eta_a}{16\pi^2} \sum_{l=1}^{K_a} (-j)^l (2l+1) h_l^{(2)}(k_a R_{\mathbf{u}'\mathbf{u}}) \Phi_l(\hat{\mathbf{R}}_{\mathbf{u}'\mathbf{u}} \cdot \hat{\mathbf{k}}_a^{pq}) \tag{2.28}$$

where $\hat{\mathbf{R}}_{\mathbf{u}'\mathbf{u}} = \mathbf{R}_{\mathbf{u}'\mathbf{u}} / R_{\mathbf{u}'\mathbf{u}}$, $\Phi_l(\cdot)$ is the Legendre polynomial of degree l and $h_l^{(2)}$ denotes the spherical Hankel function of the second kind. All $\mathcal{T}_{\mathbf{u}'-\mathbf{u}}(\hat{\mathbf{k}}_a^{pq})$ computed and stored for all directions constitute the third large data structure mentioned in the introduction and can be compressed via Tucker decomposition [29], as explained in the next subsection. In practice, the circular convolution in (2.27) for each $\hat{\mathbf{k}}_a^{pq}$ is performed as follows. First, $\mathcal{T}_{\mathbf{u}'-\mathbf{u}}(\hat{\mathbf{k}}_a^{pq})$ is computed by Fourier transforming $\mathcal{T}^{\sim}_{\mathbf{u}'-\mathbf{u}}(\hat{\mathbf{k}}_a^{pq})$ with indices $u'_x = -N_x+1, \ldots, N_x$, $u'_y = -N_y+1, \ldots, N_y$, $u'_z = -N_z+1, \ldots, N_z$, $(u'_x, u'_y, u'_z \neq 0)$ and $\mathbf{u}=(1,1,1)$. Second, $\mathcal{T}_{\mathbf{u}'-\mathbf{u}}(\hat{\mathbf{k}}_a^{pq})$ is multiplied with the Fourier transform of $\mathcal{F}_{\mathbf{u}}(\hat{\mathbf{k}}_a^{pq})$ with indices $u_x = 1, \ldots, N_x$, $u_y = 1, \ldots, N_y$, $u_z = 1, \ldots, N_z$, after the dimensions of $\mathcal{F}_{\mathbf{u}}(\hat{\mathbf{k}}_a^{pq})$ are increased to $(2N_x-1)\times(2N_y-1)\times(2N_z-1)$ by zero padding. After computing all $\mathcal{G}_{\mathbf{u}'}(\hat{\mathbf{k}}_a^{pq})$, those are projected onto the testing basis functions and far-field contributions to the matrix-vector multiplication in (2.14) are computed by summing over all directions with quadrature weights ω_a^{pq} as

$$\sum_{a=0}^{1} \sum_{p=1}^{K_a+1} \sum_{q=1}^{2K_a+1} w_a^{pq} \mathbf{P}^{-}(\hat{\mathbf{k}}_a^{pq}, \hat{\mathbf{n}}_d \times \mathbf{f}_m) \cdot \mathcal{G}_{\mathbf{u}'}(\hat{\mathbf{k}}_a^{pq}), \quad 1 \le m \le N_d \tag{2.29}$$

$$\sum_{a=0}^{1} \sum_{p=1}^{K_a+1} \sum_{q=1}^{2K_a+1} w_a^{pq} \left(\mathbf{P}^{-}(\hat{\mathbf{k}}_a^{pq}, \hat{\mathbf{n}}_d \times \mathbf{f}_m) \times \hat{\mathbf{k}}_a^{pq} \right) \cdot \mathcal{G}_{\mathbf{u}'}(\hat{\mathbf{k}}_a^{pq}) \, (\beta_a / \alpha_a), \; N_d + 1 \le m \le 2N_d \tag{2.30}$$

$$\begin{aligned} \sum_{p=1}^{K_0+1} \sum_{q=1}^{2K_0+1} w_0^{pq} / \alpha_0 \Big(& \alpha_p \mathbf{P}^{-}(\hat{\mathbf{k}}_0^{pq}, \mathbf{f}_m) - (1-\alpha_p) \\ & \mathbf{P}^{-}(\hat{\mathbf{k}}_0^{pq}, \hat{\mathbf{n}}_p \times \mathbf{f}_m) \times \hat{\mathbf{k}}_0^{pq} \Big) \cdot \mathcal{G}_{\mathbf{u}'}(\hat{\mathbf{k}}_0^{pq}), \; 2N_d + 1 \le m \le N \end{aligned} \tag{2.31}$$

To execute the FMM-FFT algorithm on high-performance parallel computers for characterizing large scale mine tunnels/galleries loaded with conductors, a hybrid spatial/angular parallelization strategy, which utilizes hybrid message passing interface/open multiprocessing (MPI/OpenMP) standards, is deployed. This parallelization strategy, described in next section, uniformly partitions the memory and computational loads along angular dimension (i.e., plane-wave directions) and spatial dimension (i.e., groups) among processors. Such parallelization strategy introduces two additional processor-to-processor communications compared to the spatial partitioning strategy in [33]. These additional communications require negligible time when non-blocking MPI operations are used. On the other hand, the hybrid spatial/angular parallelization strategy permits scalable workload partitioning of compression of far-field patterns, while the spatial parallelization strategy in [33] does not.

2.2.3.2 Parallel Scheme

The proposed hybrid spatial/angular parallelization strategy achieves uniform memory and computational load partitioning (among N_p processors) during the setup stage as follows: Each processor is in charge of computing and storing the matrices that hold near-field interactions and basis functions' far-fields and receiving patterns for N_g / N_p groups (spatial partitioning), where N_g stands for the total number of groups enclosing the basis functions. In addition, each processor is responsible for computing and storing the *FFT'ed* translation operator tensors for $\sum_{a=1}^{2}(K_a+1)(2K_a+1)/N_p$ plane wave directions (angular partitioning). No communication among processors is required

at this stage. During matrix-vector multiplication stage, the uniform computational load partitioning is achieved by the following steps, depicted for an example structure in Figure 2.3:

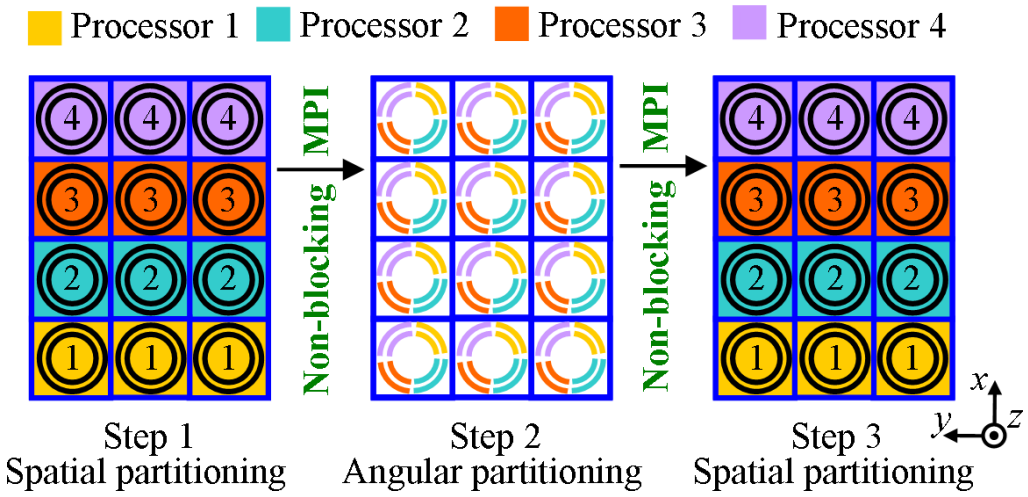

Figure 2.3 Parallelization strategy in FMM-FFT scheme for matrix-vector multiplication stage: partitioning of groups and plane wave directions among $N_p = 4$ processors for the structure composed of 4 and 3 groups along x and y directions

Step 1: Each processor computes the outgoing far-field and receiving patterns of the groups (along all directions) that it's responsible for. Then it sends a set of directions of each group's far-fields to the processor which is in charge of that set of directions. At the same time, it receives all remaining groups' far-fields along a set of directions which it's responsible for. This process can be better explained on the example structure in Figure 2.3: Each pair of concentric circles represents one group's far-field (or receiving) patterns; outer and inner circles represent the far-field (or receiving) patterns computed for the medium 1 and medium 0 (air), respectively. The angular dimension of each circle concerns the angular samples (or directions) of the far-field (or receiving) pattern. The

number printed inside/near (and color of) the concentric circles/arcs indicates the ID of the processor in charge of the data. For the example structure, each processor computes three groups' far-field patterns along all directions [via (2.25)] and keeps a quarter of this data (as $N_p = 4$) that is pertinent to directions the processor is responsible for. It sends the remaining portion of this data to the other processors which are responsible for the remaining directions. At the same time, it receives the data from other processor pertinent to remaining groups' far-fields along a set of directions which it's responsible for. The send and receive operations are performed using non-blocking MPI commands.

Step 2: Each processor has all groups' outgoing far-field patterns and *FFT'ed* translation operator tensors for a set of directions that it's responsible for (shown by arcs in Figure 2.3). Using this data, each processor performs the translation operation (via (2.27)) and obtains incoming plane wave spectra for each direction that it's in charge of. Then it sends each group's incoming wave spectrum along a set of directions to the processor which is in charge of that group. At the same time, it receives the incoming wave spectrum along remaining directions from the other processors for each group that the processor is responsible for. Again, send and receive operations are performed non-blocking MPI commands.

Step 3: Each processor has the incoming plane wave spectra of the groups (along all directions) that it is responsible for. Using each group's incoming plane wave spectrum and receiving pattern of the basis function that sits in that group, it computes the far-field contribution to the matrix-vector multiplication pertinent to m^{th} basis function.

As each processor computes and stores near-field interaction matrices of each group that it's in charge of, it also locally computes near-field contribution to the matrix-vector multiplication pertinent to m^{th} basis function that sits in that group. At the end of each matrix-vector multiplication, each processor sums the near- and far-field contributions pertinent to all basis functions that sit in groups which the processor is responsible for. Then it writes the results to the pertinent entries of a vector with dimension N which is distributed to all processors by all-to-all communication (MPI_Allreduce).

2.2.3.3 SVD and Tucker Decomposition

To reduce the memory requirement of the SIE simulator leveraging FMM-FFT algorithm, large data structures storing the near-field interactions, far-field (and receiving) patterns of basis functions, and *FFT'ed* translation operator tensors are compressed via SVD and its higher-dimensional counterpart Tucker decomposition.

First, the near-field interaction matrices are compressed. Assume that the near-field interactions between N_s source basis functions in a group $B_{\mathbf{u}}$ (e.g., $\mathbf{u}$=(1,1,1) in Figure 2.2) and N_t testing basis functions in a group $B_{\mathbf{u}'}$ (e.g., $\mathbf{u}'$=(2,1,1) in Figure 2.2) are stored in a matrix $\bar{\mathbf{Q}}$ with dimensions $N_t \times N_s$, which is a rank deficient block of MoM matrix with entries $\bar{\mathbf{Z}}_{mn}$, $m \in B_{\mathbf{u}'}$, $n \in B_{\mathbf{u}}$, and can be compressed via truncated SVD (TrSVD(·)) as

$$\bar{\mathbf{Q}} \approx \text{TrSVD}\left(\bar{\mathbf{Q}}\right) = \bar{\mathbf{U}}\bar{\mathbf{\Sigma}}\bar{\mathbf{V}}^{*}, \tag{2.32}$$

where $*$ stands for conjugate transpose, $\bar{\mathbf{U}}$ and $\bar{\mathbf{V}}$ are truncated unitary matrices with dimensions $N_t \times r$ and $N_s \times r$, respectively, and $\bar{\mathbf{\Sigma}}$ is the diagonal matrix with descending r singular values of $\bar{\mathbf{Q}}$, δ_i, $i = 1,\ldots,r$, which are greater than a prescribed tolerance γ_2 times the value of first singular value, i.e. $\delta_i \geq \gamma_2 \delta_1$, $i = 1,\ldots,r$. During setup stage, truncated SVD compression is applied to all MoM matrix blocks that stores the near-field interactions between groups, but not applied to full rank blocks pertinent to self-interactions of groups. During the iterative solution, the reduced representations in (2.32) are directly used without restoring the full block $\bar{\mathbf{Q}}$ to compute the contributions of near-field interactions to the matrix vector multiplication.

Second, the far-field matrices are compressed. Assume that one component (θ or ϕ) of far-field (or receiving) pattern of a basis function for a medium $a \in \{0,1\}$ is stored in a matrix $\bar{\mathbf{W}}$ with dimensions $(K_a + 1) \times (2K_a + 1)$, which tabulates the farfield samples along elevation and azimuthal directions through its rows and columns, respectively. Given the prescribed tolerance γ_3, $\bar{\mathbf{W}}$ can be approximated by its truncated SVD as

$$\bar{\mathbf{W}} \approx \mathrm{TrSVD}\left(\bar{\mathbf{W}}\right) \tag{2.33}$$

This operation is applied to θ and ϕ components of all basis functions' far-field and receiving patterns for both media. The resulting truncated unitary matrices and singular values obtained and stored during setup stage are used to restore the far-field and receiving patterns one-by-one during the iterative solution.

Finally, the *FFT'ed* translation operator tensors are compressed. The tensor storing the *FFT'ed* translation operator samples for each $\hat{\mathbf{k}}_a^{pq}$, $\mathcal{T}_{\mathbf{u}'-\mathbf{u}}$, has dimensions $D_1 \times D_2 \times D_3 = (2N_x - 1) \times (2N_y - 1) \times (2N_z - 1)$ and can be compressed via Tucker decomposition as [34]

$$\mathcal{T}_{\mathbf{u}'-\mathbf{u}} \approx \mathcal{X} \times_1 \bar{\mathbf{U}}_1 \times_2 \bar{\mathbf{U}}_2 \times_3 \bar{\mathbf{U}}_3 \tag{2.34}$$

where $\mathcal{X}$ is the core tensor with dimensions $r_1 \times r_2 \times r_3$, $\bar{\mathbf{U}}_i$, $i = 1, \ldots, 3$, denote the factor matrices with dimensions $D_i \times r_i$, $i = 1, \ldots, 3$, and $\times_i$, $i = 1, \ldots, 3$, stands for the $i-$mode matrix product of a tensor, which can be performed as explained in [35]. The core tensor and factor matrices are obtained via the following procedure: (i) The unfolding matrices of $\mathcal{T}_{\mathbf{u}'-\mathbf{u}}$, $\bar{\mathbf{T}}_i$, $i = 1, \ldots, 3$, are formed. (Note: An example of forming unfolding matrices of a tensor is given in Eqn. 2.1. of [35].) (ii) Given the prescribed tolerance $\gamma_4 / \sqrt{3}$, the truncated SVDs of unfolding matrices, $\mathrm{TrSVD}(\bar{\mathbf{T}}_i) = \bar{\mathbf{U}}_i \bar{\mathbf{\Sigma}}_i \bar{\mathbf{V}}_i^*$, $i = 1, \ldots, 3$, are obtained. The resulting truncated unitary matrices $\bar{\mathbf{U}}_i$, $i = 1, \ldots, 3$, are the factor matrices of (2.34). (iii) The core tensor can be obtained via

$$\mathcal{X} = \mathcal{T}_{\mathbf{u}'-\mathbf{u}} \times_1 \bar{\mathbf{U}}_1^* \times_2 \bar{\mathbf{U}}_2^* \times_3 \bar{\mathbf{U}}_3^*. \tag{2.35}$$

The core tensors and factor matrices of *FFT'ed* translation operator tensors for all $\hat{\mathbf{k}}_a^{pq}$ directions are obtained during the setup stage and used to restore $\mathcal{T}_{\mathbf{u}'-\mathbf{u}}$ one $\hat{\mathbf{k}}_a^{pq}$ at a time during the iterative solution stage.

Numerical Example	Frequency (MHz)	Polarization	Number of processors	Average memory required for each processor (GB)		Time (hours)
				Without Compression	With Compression	
Empty arched tunnel	455	Vertical	32	28.40	14.62	5.28
		Horizontal				5.33
	915	Vertical	45	64.91	36.45	29.93
		Horizontal				28.82
Arched tunnel loaded with carts	455	Vertical	16	20.09	10.58	4.48
Arched tunnel loaded with strips	50	Vertical	32	2.28	-	9.37
Mine gallery	455	Vertical	32	21.05	10.60	4.87
		Horizontal				4.63
	915	Vertical	45	46.27	28.89	23.82
		Horizontal				22.75
Rectangular tunnel with rough walls	455	Vertical	32	30.04	12.73	6.37
Rectangular tunnel with smooth walls	455	Vertical	32	28.45	12.28	6.75

Table 2-1 Specifications of simulation performed by the FMM-FFT accelerated SIE simulator for each numerical example.

2.3 Numerical Results and Discussions

This section presents numerical examples that demonstrate the accuracy, efficiency, and applicability of the proposed FMM-FFT accelerated SIE simulator. In all examples below, the FMM box size is half of the wavelength in ore, FMM accuracy is 3

digits ($\gamma_1 = 3$), the solution of the system of equations is achieved using a transpose-free quasi-minimal residual iterative solver [36] with residual error 10^{-6}, and tolerances γ_2, γ_3, and γ_4 for compressing matrices and tensors are 10^{-3}, 10^{-4}, and 10^{-6}, respectively. Furthermore, tunnels and galleries are surrounded by ore with permittivity $\varepsilon_1 = \varepsilon_0(\varepsilon_{r,1} - j\sigma_1/\omega\varepsilon_0)$ and permeability $\mu_1 = \mu_0$; $\varepsilon_{r,1}$ and σ_1 are the relative permittivity and conductivity of the ore, respectively. All simulations are performed on a cluster of dual hexacore X5650 Intel processors with 64 GB RAM, launching one MPI process on each core and distributing computational tasks on the 16 cores in each processor via OpenMP. The CPU and memory requirements of the proposed solver for all numerical examples are tabulated in Table 2-1.

2.3.1 Arched Tunnel

First, the proposed simulator is used to analyze EM wave propagation in an arched tunnel surrounded by ore with $\varepsilon_{r,1} = 8.9$ and $\sigma_1 = 0.15$ S/m [Figure 2.4 (a)]. A transmitting electrically-small electric dipole with unit moment is positioned at $(0.915, 50, 1.22)$ m and power densities are computed on lines inside the tunnel. Three different scenarios are considered: an empty tunnel, a tunnel loaded with mine carts, and a tunnel loaded with conducting strips that model a transmission line.

2.3.1.1 Empty Tunnel

A 600 m – long tunnel is excited by either a $z-$ (vertically) or $x-$ (horizontally) oriented dipole operated at 455 MHz or 915 MHz (4 cases) [Figure 2.4 (a)]. At the

lower and higher frequencies, the current densities on the tunnel walls are discretized using $N = 15,153,996$ and $N = 58,510,782$ RWG basis functions, respectively. Power densities computed on the line connecting $(0.915, 51, 1.22)$ m and $(0.915, 600, 1.22)$ m are compared with measured data following normalization to account for uncertainties/differences in the excitation mechanism [Figure 2.4 (b)-(e)]. Computed and measured power densities are in good agreement, thereby validating the accuracy of the simulator. The dynamic range of both the simulator and measurements is approximately 100 dB and reflected in Figure 2.4 (b), (c), and (e). The magnitude of the electric current density on the tunnel walls computed for each orientation of the transmitting dipole and frequency is shown in Figure 2.4 (f)-(i). It decays in accordance with the power density along the tunnel. It can be seen from Table 2-1 that the proposed compression schemes reduce the memory requirements of the simulator by factors of 2 for 455 MHz and 1.8 for 915 MHz.

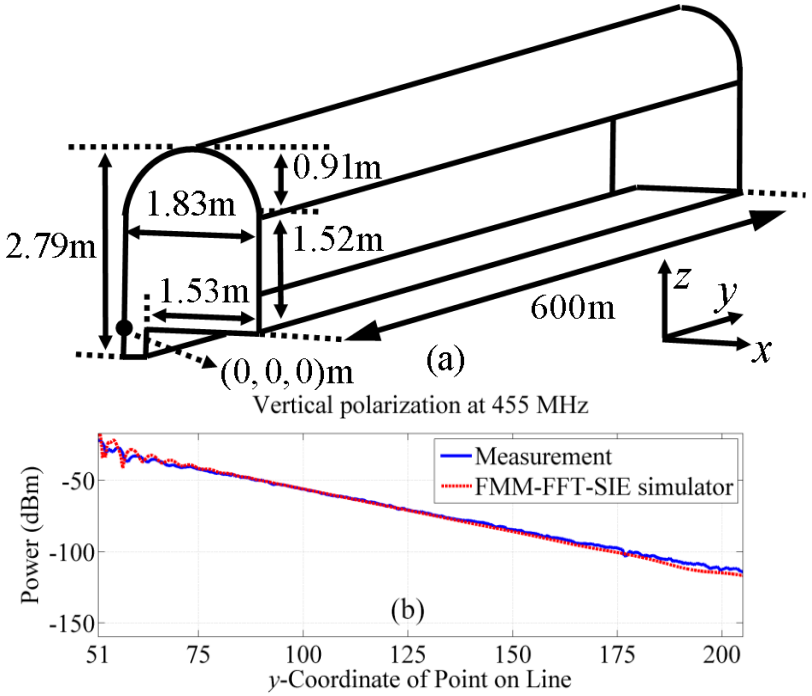

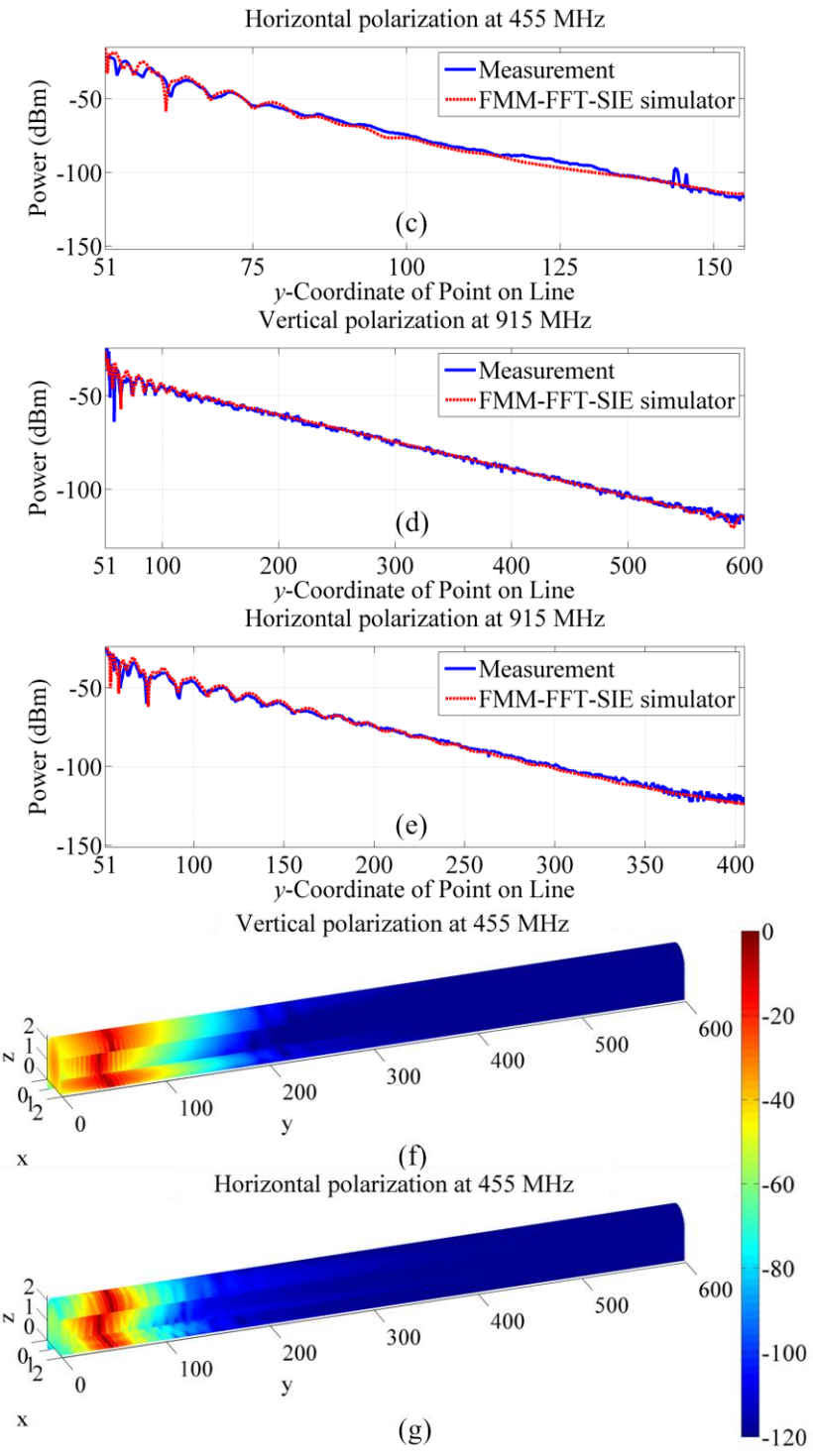
Horizontal polarization at 455 MHz
Measurement
FMM-FFT-SIE simulator
Power (dBm)
-50
-100
-150
51
75
100
125
150
(c)
y-Coordinate of Point on Line
Vertical polarization at 915 MHz
Measurement
FMM-FFT-SIE simulator
Power (dBm)
-50
-100
51
100
200
300
400
500
600
(d)
y-Coordinate of Point on Line
Horizontal polarization at 915 MHz
Measurement
FMM-FFT-SIE simulator
Power (dBm)
-50
-100
-150
51
100
150
200
250
300
350
400
(e)
y-Coordinate of Point on Line
Vertical polarization at 455 MHz
z
x
y
0
100
200
300
400
500
600
(f)
Horizontal polarization at 455 MHz
z
x
y
0
100
200
300
400
500
600
(g)
0
-20
-40
-60
-80
-100
-120

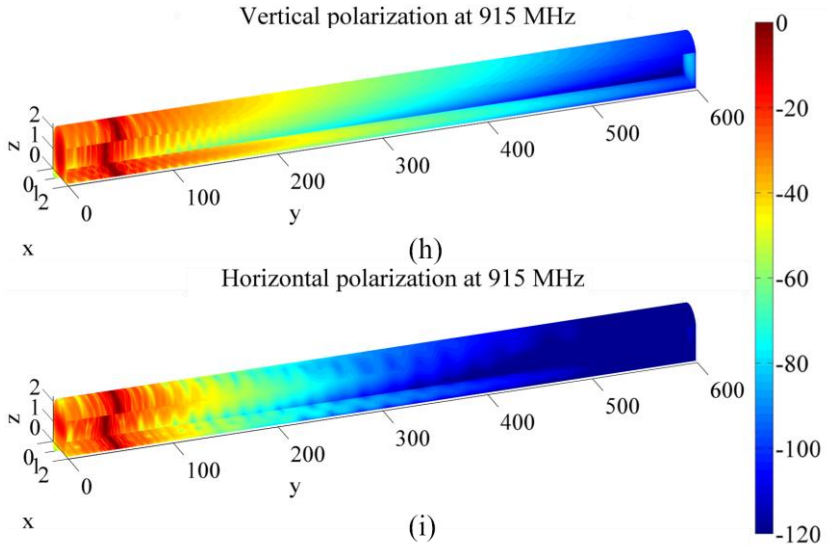

Figure 2.4 (a) The geometry of an empty 600m-long arched tunnel. The power values on receiver points computed by the FMM-FFT-SIE simulator and obtained by measurements at 455 MHz for (b) vertical and (c) horizontal polarizations and at 915 MHz for (d) vertical and (e) horizontal polarizations. Electric current density on tunnel walls computed by the proposed simulator at 455 MHz for (f) vertical and (g) horizontal polarizations and at 915 MHz for (h) vertical and (i) horizontal polarizations (in dB scale)

2.3.1.2 Tunnel Loaded with Mine Carts

A 200m long tunnel loaded with six PEC mine carts is excited by a $z-$directed electric dipole operated at 455 MHz [Figure 2.5 (a)]. The mine carts are centered at $(0.915, 80.25+(j-1)\times 20, 0.55)$ m, $j=1,\ldots,6$; their surfaces and wheels are modeled by truncated inverted pyramids and circular cylinders, respectively [Figure 2.5 (a)].

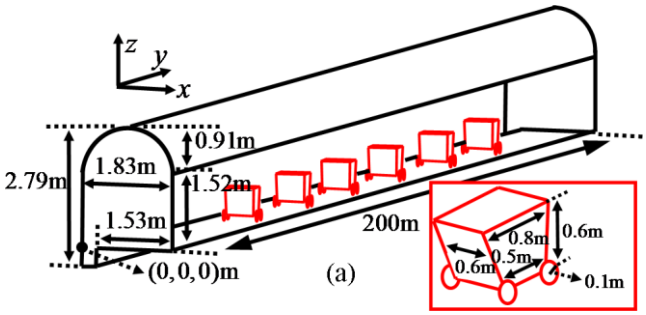

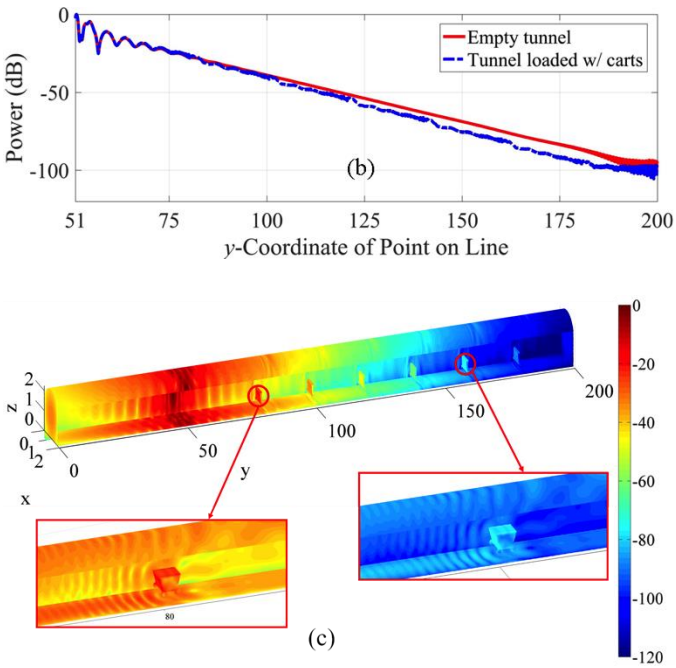

Figure 2.5 (a) The geometry of 200m-long arched tunnel loaded with six PEC mine carts (the lateral wall is removed for illustration). (b) The power values on receiver points in empty and loaded tunnels computed by the proposed FMM-FFT-SIE simulator. (c) Electric current density on tunnel walls and mine carts computed by the proposed simulator (in dB scale).

The current densities on the tunnel walls and mine carts are discretized using N=5,433,360 RWG basis functions. Power densities computed on the line connecting $(0.915, 51, 1.22)$ m and $(0.915, 200, 1.22)$ m are compared with those in the empty tunnel (obtained in scenario *A*) [Figure 2.5 (b)]. The power density at y=184 m (just after the sixth mine cart) is 9 dB below that observed in the empty tunnel. Oscillations in the power density graph in the loaded tunnel beyond y=81 m, that is just after the first mine cart, result from reflections from subsequent carts, as evidenced by plots of the electric current density on tunnel walls displayed in Figure 2.5 (c). Again, the proposed

compression schemes reduce the solver's memory requirement by a factor of two [Table 2-1].

2.3.1.3 Tunnel Loaded with Conducting Strips

A 650 m-long tunnel loaded with two PEC strips is excited by a $z-$directed electric dipole operated at 50 MHz [Figure 2.6 (a)]. The PEC strips, which are 600 m long, infinitesimally thin, 4 cm wide, and separated by 0.3 m, model a transmission line placed near the lateral tunnel wall and are centered at $(0.17, 345, 1.07)$ m and $(0.17, 345, 1.37)$ m. The current densities on the tunnel walls and conducting strips are discretized using $N = 442,044$ RWG basis functions and the simulation is performed without FMM-FFT acceleration as the FMM-FFT algorithm is numerically unstable for low frequencies [32]. Normalized power densities computed along two lines connecting point $(0.915, 51, 1.22)$ m to $(0.915, 645, 1.22)$ m (tunnel center), and point $(0.17, 51, 1.22)$ m to $(0.17, 645, 1.22)$ m (middle of strips) are shown in Figure 2.6 (b). A standing wave phenomenon can be observed at receiver points near to the wall at $y = 650$ m. The magnitude of the electric current densities induced on tunnel walls and conductor strips is shown in Figure 2.6 (c). The current densities induced on the strips conform to a bifilar mode [26], allowing the field to travel deep into the tunnel. The unloaded tunnel does not support any propagating modes.

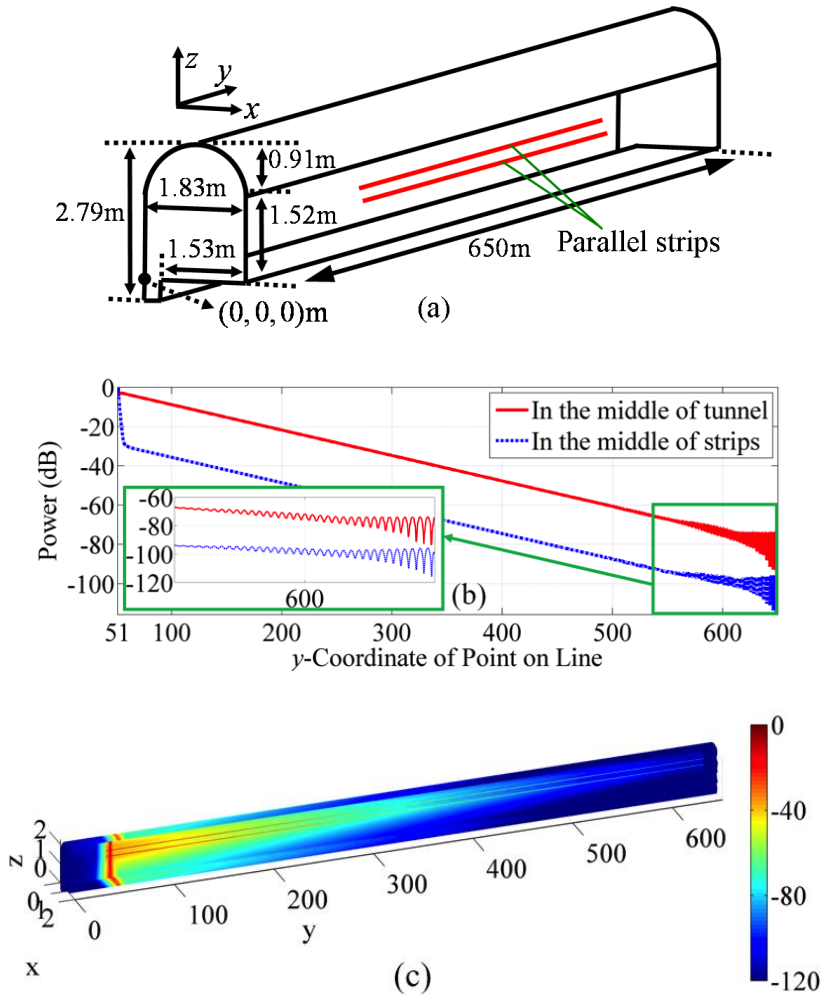

Figure 2.6 (a) The geometry of 650m-long arched tunnel loaded with two parallel PEC strips (the lateral wall is removed for illustration). (b) The power values at receiver points on a line in the middle of strips and on a line in the middle of tunnel computed by the proposed simulator. (c) Electric current density on tunnel walls and mine carts computed by the proposed simulator (in dB scale) (the half of the tunnel is removed to clearly observe the currents around strips).

2.3.2 Mine Gallery

Next, the proposed simulator is used to analyze EM wave propagation in a mine gallery formed by eight rectangular tunnels [Figure 2.7 (a)], four of which extend along the x direction and intersect the remaining four extending along the y direction [Figure

2.7 (a)]. The tunnels are surrounded by ore with $\varepsilon_{r,1}=3$ and $\sigma_1=0.001\,\mathrm{S/m}$. The gallery is excited by an electric dipole with unit moment that is centered at $(7.5,15.91,1.12)\,\mathrm{m}$, either $z-$ (vertically) or $y-$ (horizontally) oriented, and operated at either 455 MHz or 915 MHz (four cases). The current densities on the walls are discretized using $N=15{,}766{,}560$ and $N=58{,}794{,}816$ RWG basis functions at the lower and higher frequencies, respectively. For both polarizations and frequencies, normalized power densities computed at receiver points along four lines in the *x*-directed tunnels connecting $(8.5, y, 1.12)\,\mathrm{m}$ to $(81.5, y, 1.12)\,\mathrm{m}$ with y set to 15.91, 32.73, 49.55, and 66.37 are shown in Figure 2.7 (b)-(e), The observations are followed in order. First, in tunnel 2, power densities at receivers with $x-$coordinates less than 15.91 m are always larger than those at receivers with $x-$coordinates exceeding 15.91 m [Figure 2.7 (b)-(e)]. Slight or no decay is observed for receivers with $x-$coordinates lower than 15.91 m as direct coupling from the transmitter to these receiver points occurs through the low-loss ore. Second, small or large spikes appear in the power density plots near receivers with $x-$coordinates 15.9 m, 32.7 m, 49.5 m, and 66.3 m in tunnels 3 and 4 [Figure 2.7 (b)-(e)]. Note that these receivers reside at the intersections of tunnels 3 and 4 and tunnels 5, 6, 7, and 8; these spikes result from waves guided by tunnels 5, 6, 7, and 8.

The electric current densities on gallery walls computed for each frequency and polarization are shown in Figure 2.7 (f)-(i); these plots indirectly confirm the above power density observations. It can be seen in Table 2-1 that the proposed compression schemes reduce the memory requirements of the simulator by factors of 2 at 455 MHz and 1.6 at 915 MHz.

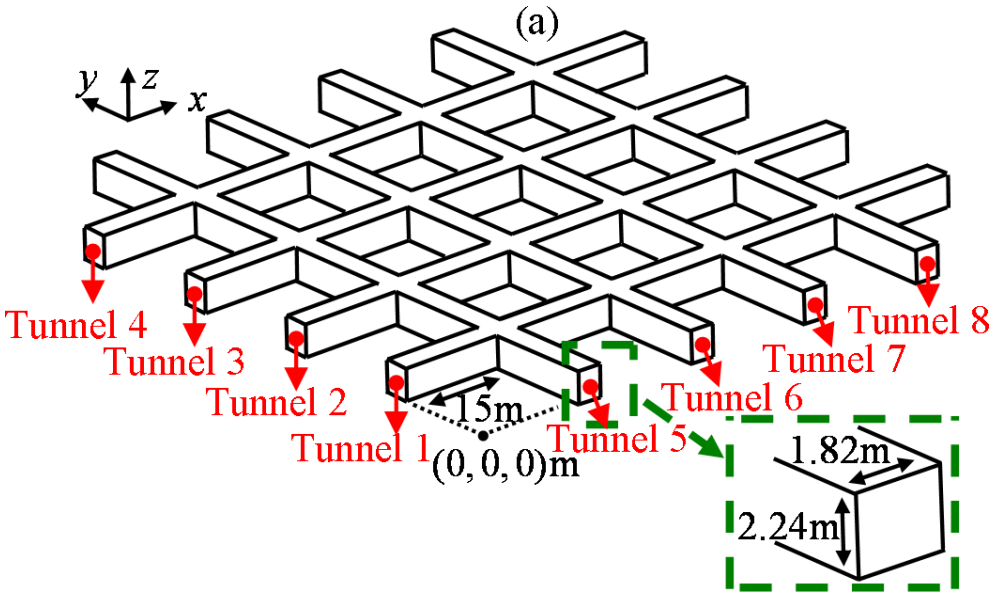
(a)
y
z
x
Tunnel 4
Tunnel 3
Tunnel 2
Tunnel 1
15m
(0, 0, 0)m
Tunnel 5
Tunnel 6
Tunnel 7
Tunnel 8
1.82m
2.24m

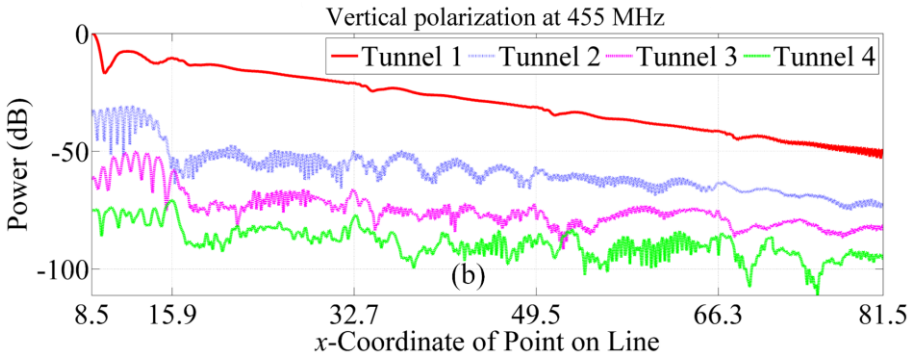
Vertical polarization at 455 MHz
Tunnel 1
Tunnel 2
Tunnel 3
Tunnel 4
Power (dB)
0
-50
-100
(b)
8.5
15.9
32.7
49.5
66.3
81.5
x-Coordinate of Point on Line

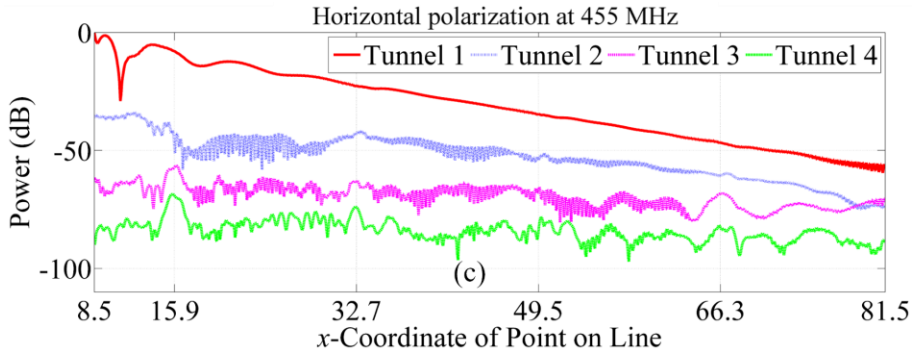
Horizontal polarization at 455 MHz
Tunnel 1
Tunnel 2
Tunnel 3
Tunnel 4
Power (dB)
0
-50
-100
(c)
8.5
15.9
32.7
49.5
66.3
81.5
x-Coordinate of Point on Line

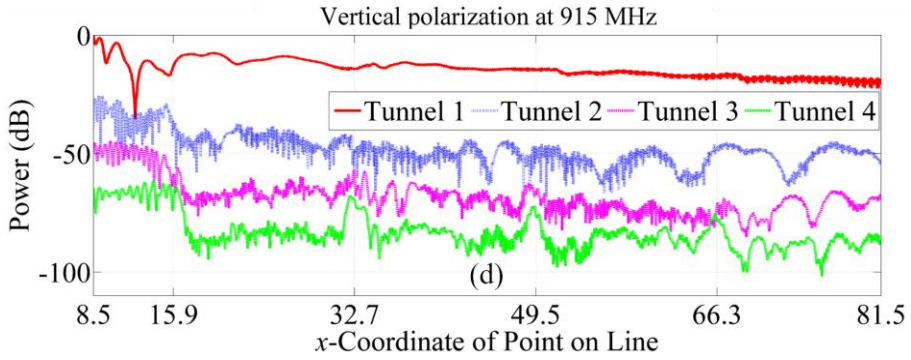
Vertical polarization at 915 MHz
Power (dB)
0
-50
-100
Tunnel 1
Tunnel 2
Tunnel 3
Tunnel 4
(d)
8.5
15.9
32.7
49.5
66.3
81.5
x-Coordinate of Point on Line

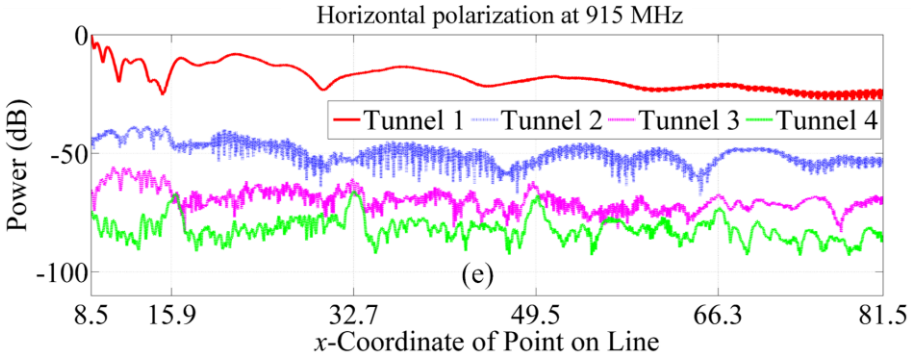
Horizontal polarization at 915 MHz
Power (dB)
0
-50
-100
Tunnel 1
Tunnel 2
Tunnel 3
Tunnel 4
(e)
8.5
15.9
32.7
49.5
66.3
81.5
x-Coordinate of Point on Line

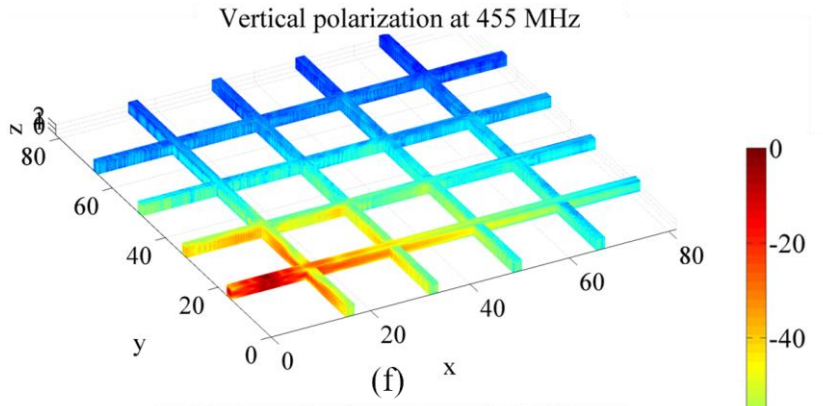
Vertical polarization at 455 MHz
z
80
60
40
20
0
y
0
20
40
60
80
x
(f)
0
-20
-40
-60
-80
-100
-120

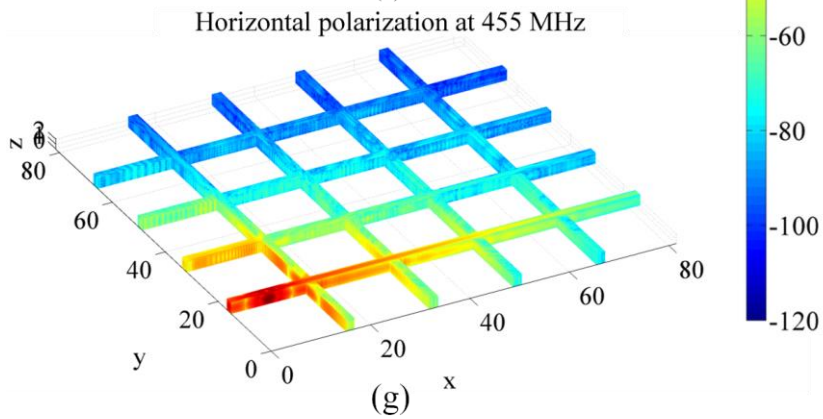
Horizontal polarization at 455 MHz
z
80
60
40
20
0
y
0
20
40
60
80
x
(g)

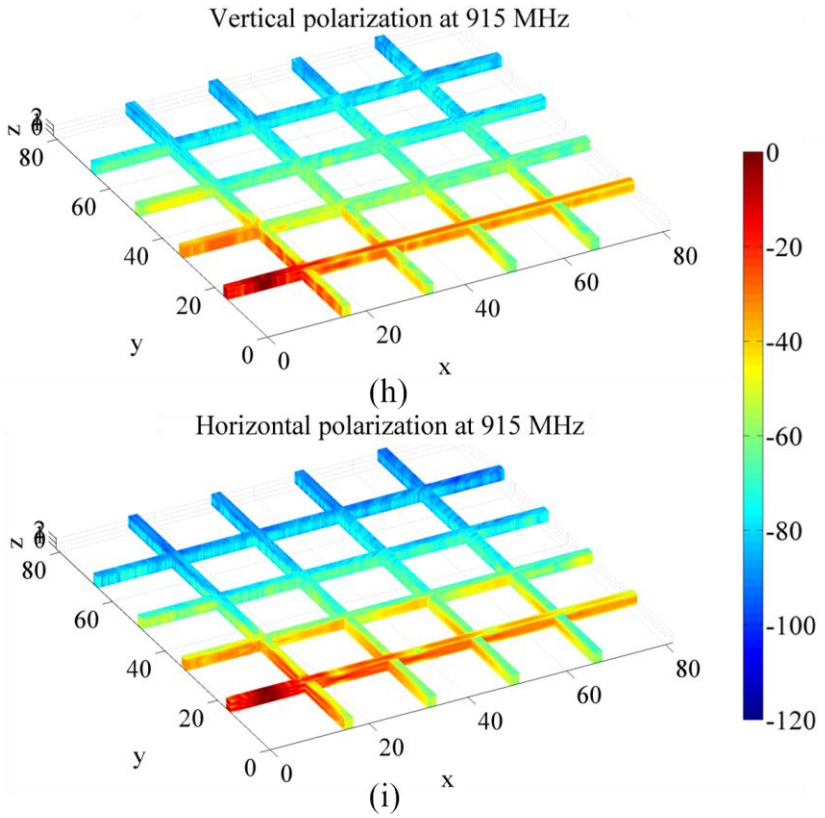

Figure 2.7 (a) The geometry of a mine gallery formed by eight tunnels. (b) The power values at receiver points on lines inside tunnel 1, 2, 3, and 4 computed by the proposed FMM-FFT-SIE simulator at 455 MHz for (b) vertical and (c) horizontal polarizations and at 915 MHz for (d) vertical and (e) horizontal polarizations. Electric current density on tunnel walls computed by the proposed simulator at 455 MHZ for (f) vertical and (g) horizontal polarizations and at 915 MHZ for (h) vertical and (i) horizontal polarizations.

2.3.3 A Rectangular Tunnel with Rough Walls

Finally, the proposed simulator is used to analyze EM wave propagation in a rectangular tunnel with rough walls, excited by a $z-$ (vertically) oriented unit electric dipole positioned at (50.0, 0.925, 1.12) m and operated at 455 MHz [Figure 2.8 (a)]. The tunnel is surrounded by ore with $\varepsilon_{r,1}=3$ and $\sigma_1=0.001\,\mathrm{S/m}$. Tunnel walls have a random profile with 0.1 m root-mean-square (RMS) height and 0.25 m correlation length [37].

The current densities on the tunnel walls are discretized using $N=13,580,916$ RWG basis functions. Results for the tunnel with rough walls are compared to those for the corresponding tunnel with smooth walls, and power densities are computed along a line connecting (51.0, 0.925, 1.12) m and (200, 0.925, 1.12) [Figure 2.8 (b)]. The power density at $y=175$ m for the tunnel with rough walls is 7.34 dB below that for the tunnel with smooth walls. Furthermore, the power densities computed by the proposed simulator for the tunnel with smooth walls are compared to those obtained using the multi-modal decomposition method of [4] in Figure 2.8 (b). Near-perfect agreement between the two results is observed, and validating the accuracy of the proposed simulator. In addition, the electric current densities computed on rough and smooth walls are shown in Figure 2.8 (c) and (d). Clearly, the decay of the current densities on tunnel walls for both cases conforms with the decay of the power densities along the tunnels. The compression schemes reduce the solvers' memory requirements by a factor more than two [Table 2-1].

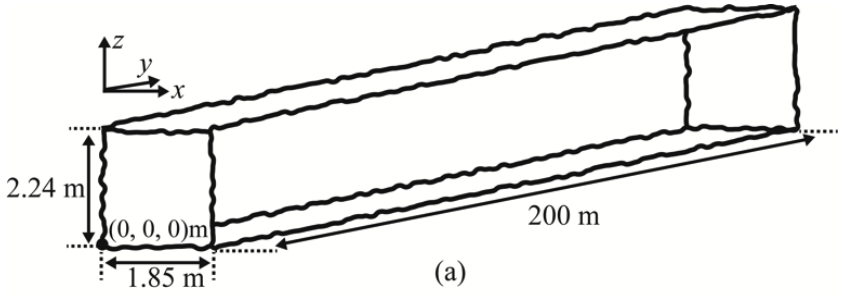

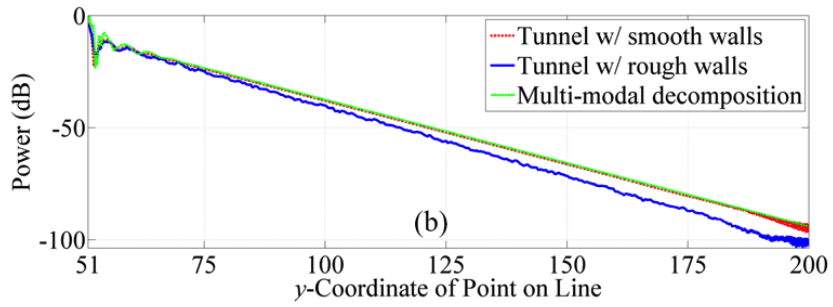

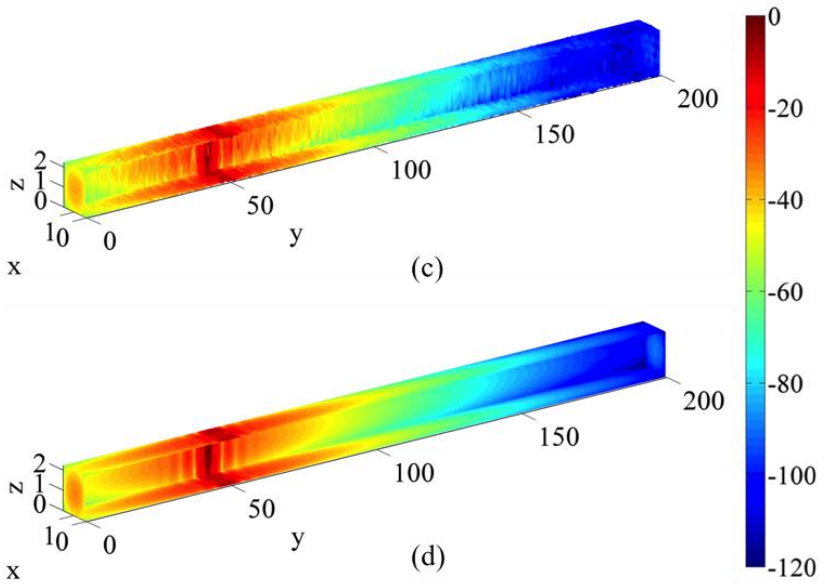

Figure 2.8 (a) The geometry of 200 m-long rectangular tunnel with rough walls. (b) The power values at receiver points on a line in the middle of tunnel computed by the proposed simulator for the tunnel with smooth and rough walls and by the multi-modal decomposition for the tunnel with smooth walls. Electric current density on (c) rough walls and (d) smooth walls of the rectangular tunnel computed by the proposed simulator (in dB scale).

2.4 Chapter Conclusion

An FMM-FFT accelerated SIE full wave simulator is presented for characterizing EM wave propagation in electrically large and loaded mine environments. The full wave simulator rapidly solves the Muller-combined field SIE system using a parallel FMM-FFT acceleration scheme. To reduce the memory requirements, the simulator employs SVDs and Tucker decompositions to compress large data structures. Numerical results demonstrate the accuracy, efficiency, and applicability of the proposed simulator.

CHAPTER 3
A Domain Decomposition Based Surface Integral Equation Simulator for Characterizing Electromagnetic Wave Propagation in Mine Environments

3.1 Chapter Introduction

The wireless communication, sensing, and tracking systems are essential for performing routine mining operations, ensuring miners' safety, and conducting life-saving operations after catastrophic events. The design, characterization, and (re-) configuration of such systems call for efficient and accurate electromagnetic (EM) simulators capable of characterizing EM wave propagation in large-scale and realistic mine environments. Existing EM simulators developed for this purpose are either based on approximate methods or full wave techniques [1]. The simulators based on approximate methods including single/multi-mode waveguide expansion [38, 39], ray-tracing [40-42], and cascaded-impedance [8] methods achieve high computational efficiency, but have limited applicability: These simulators are typically operated at certain frequency bands and not applicable to the analysis of EM wave propagation in complex mine environments with rough walls, debris from a cave-in, mining equipments, and cables. In contrast, the

simulators based on full-wave techniques including finite difference time domain [43-46] and surface integral equation (SIE) [47-50] methods are operated at desired frequency bands and permit high-fidelity modeling of realistic mine environments. Nevertheless, they require excessive computational resources due to large electrical sizes of tunnels/galleries at wireless systems' operating frequencies. To alleviate this computational burden, a fast multipole method - fast Fourier transform (FMM-FFT) accelerated SIE simulator has been proposed recently [49, 50]. This simulator leverages singular value decomposition (SVD) and higher-order SVD based compression schemes to attain low memory requirement while rapidly solving SIEs via FMM-FFT scheme. Albeit efficient for EM analysis with single excitation, the simulator requires excessive computational time when used for EM analyses with many different excitations, which require repetitive execution of EM simulator and arise in uncertainty quantification and optimum wireless node placement studies [51, 52].

In this chapter, a fast, full-wave, and memory-efficient domain decomposition (DD) based 3-D SIE simulator is proposed for efficiently analyzing EM wave propagation in electrically large and realistic mine environments when single or multiple excitations exist. The proposed simulator extends the ideas in our previous work [48] on TMz wave propagation in 2-D mine layouts to EM wave propagation in 3-D realistic mine environments, but with significant algorithmic enhancements. The proposed simulator first divides the physical mine tunnels/galleries into subdomains and defines equivalent surfaces between them using Huygens' principle. Then, it obtains reduced order representations using equivalent surfaces to characterize EM wave propagation in each subdomain separately. The reduced order representations –called scattering

matrices– are computed using a fast and efficient butterfly-based direct solver [53] and an FMM–FFT scheme [27, 28, 54, 55]. Finally, it constructs and solves an inter-domain system accounting for EM interactions between equivalent surfaces. The solution of inter-domain system is accelerated by judiciously combining subdomains into larger ones via an efficient subdomain combining scheme for electrically large mine environments.

As explained in detail in this chapter and shown in numerical results section, the proposed simulator is far more memory and CPU efficient than the conventional fast simulators, such as FMM-FFT accelerated SIE simulators. It significantly outperforms the conventional fast simulators especially for the problems involving EM analyses of electrically large tunnels/galleries with multiple excitations, encountered in uncertainty quantification and optimal wireless node placement studies. This is due to the fact that the proposed simulator obtains and solves a reduced system with significantly less degrees of freedom compared to those of conventional fast simulators. To do that, it performs the analysis in two stages: (i) it computes the scattering matrices (only once) during its offline stage and (ii) it updates the right hand side of inter-domain system and solves the reduced system for each different excitation during its online stage. For such problems involving electrically large tunnels, the subdomain combining scheme is applied and the computational cost of the proposed simulator, which peak at stage (ii), scale logarithmically with the tunnel length while that of the conventional fast simulators scales quasi-linearly. When the subdomain combining scheme is not applied, the computational cost of the proposed simulator scale linearly with the tunnel length and is still lower than that of conventional fast simulators for electrically large tunnels. Furthermore, the memory requirement of the proposed simulator with and without

subdomain combining scheme scales logarithmically and remains constant with tunnel length, respectively. These unprecedented memory requirements are much smaller than that of conventional fast simulators, which scales quasi-linearly.

It is noteworthy to mention that previously proposed DD based full wave methods (see [56] and references therein) leverage the similar ideas proposed here and exploit equivalent surfaces to reduce the dimensionality of linear systems pertinent to the structures involving high permittivity or discretized with fine meshes [57-63]. However, unlike these works relying on closed equivalent surfaces, the proposed simulator leverages truncated open equivalent surfaces to reduce the dimensionality of linear system by exploiting the small skin-depth feature of lossy mine ore at wireless systems' operating frequencies. The applicability, accuracy, and efficiency of the proposed simulator are demonstrated through its application to the EM wave propagation in an arched tunnel, rectangular tunnels with rough walls and partial cave-in, and a mine gallery and statistical characterization of EM wave propagation in an electrically very large rectangular tunnel.

3.2 Formulation

This section first explains the domain decomposition strategy to split the physical domain of mine environment into subdomains and expounds the computation of scattering matrices for characterizing EM wave propagation in each subdomain. Then, it presents the inter-domain system and its expedient solution via subdomain combining

scheme. Finally, it provides the theoretical estimates for the computational cost and memory requirement of the proposed simulator.

3.2.1 Domain Decomposition Strategy

Consider a straight rectangular mine tunnel which is assumed to be filled by air with permittivity ε_0 and permeability μ_0 (medium 0) and surrounded by unbounded ore with permittivity ε_1, permeability μ_1, and conductivity σ (medium 1) [Figure 3.1 (a)]. The tunnel with walls denoted by Ω [Figure 3.1 (a)] is split into four subdomains (for the sake of simplicity and demonstration) denoted by Ω_i, $i = a,b,c,d$ [Figure 3.1 (b)]. By invoking the Huygens' equivalence principle, equivalent surfaces enclosing each subdomain are defined [Figure 3.1 (b)]. The adjacent subdomains and equivalent surfaces touch each other as δ approaches zero and consequently the union of subdomains Ω_i, $i = a,b,c,d$ yields the original domain [Figure 3.1 (c)].

The small skin depth due to the lossy surrounding environment and high operating frequencies of wireless communication systems allows limiting each equivalent surface to a portion of touching surfaces between adjacent subdomains [Figure 3.1 (d)-(e)]. The equivalent electric and magnetic current densities $\mathbf{J}_p(\mathbf{r})$ and $\mathbf{M}_p(\mathbf{r})$, $p = 1,\ldots,3$ are defined on these surfaces in accordance with the outward pointing unit normal of surfaces $\hat{\mathbf{n}}_p$, $p = 1,\ldots,3$. These surfaces and the equivalent current densities are used to characterize EM wave propagation in each subdomain separately, as explained in the following subsection. (Note: the domain decomposition example given in Figure 3.1 and

subdomains and equivalent surfaces defined therein are extensively referred to in this section (without loss of generality) to avoid heavy generic notation.)

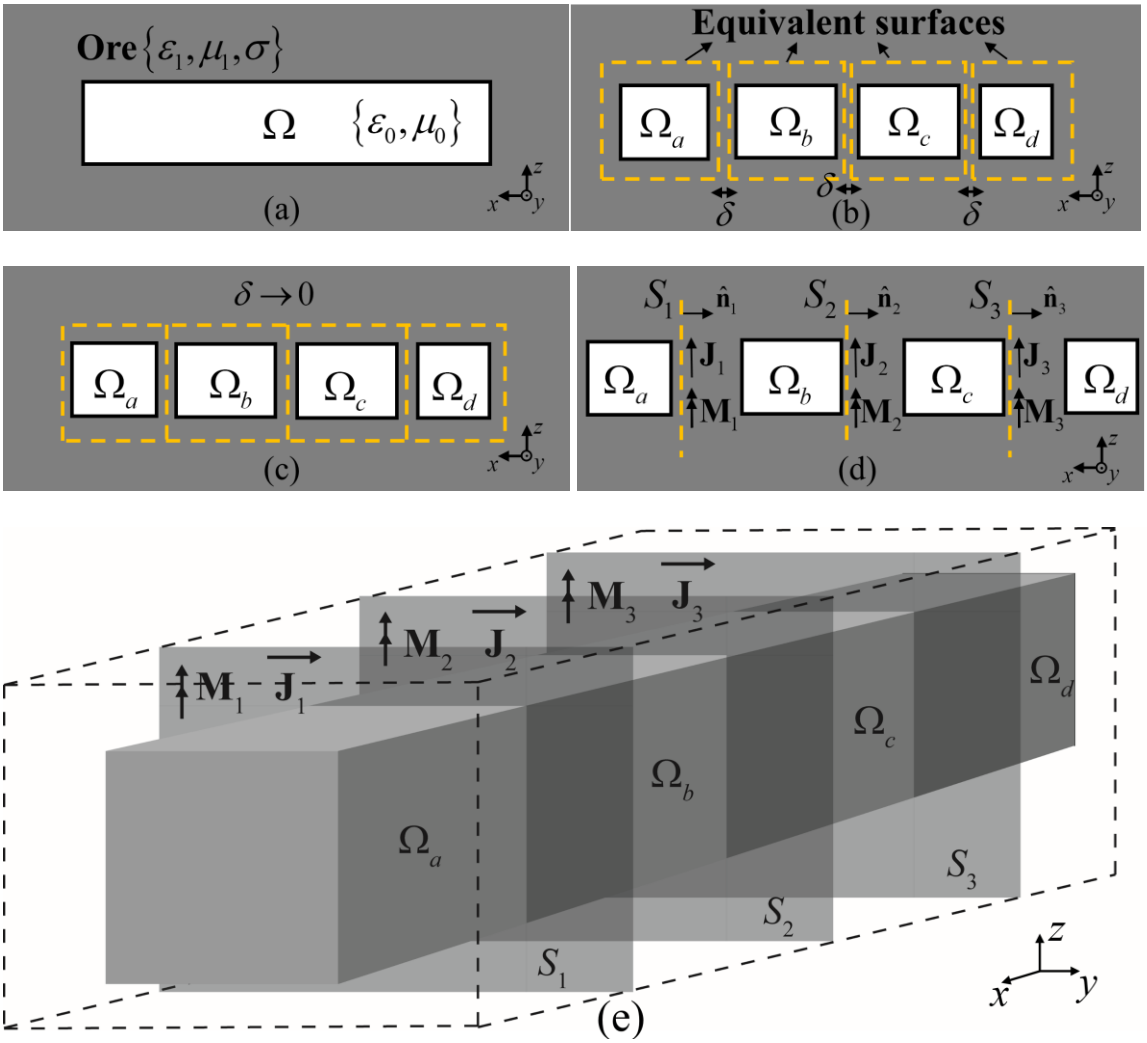

Figure 3.1 Domain decomposition scheme for a mine tunnel: (a) The original physical domain of the tunnel. (b) Decomposition with equivalent surfaces. (c) Overlapping equivalent surfaces between subdomains. (d) Truncated equivalent surfaces and equivalent currents. (e) 3-D view of the decomposed straight tunnel.

3.2.2 Scattering Matrix of Individual Subdomains

EM wave propagation in each subdomain defined in Figure 3.1 (d) is characterized by a scattering matrix $\mathbf{Z}^i$, $i \in \{a,b,c,d\}$. Consider that $\mathbf{J}_p(\mathbf{r})$ and $\mathbf{M}_p(\mathbf{r})$,

$p=1,\ldots,3$, on each equivalent surface (in Figure 3.1 (d)) are discretized by $2N_p$ Rao-Wilton-Glisson (RWG) basis functions $\mathbf{f}_{p,j}(\mathbf{r})$ [64] as

$$\mathbf{J}_p(\mathbf{r})=\sum_{j=1}^{N_p} I_{p,j}\mathbf{f}_{p,j}(\mathbf{r}),\ \mathbf{M}_p(\mathbf{r})=\sum_{j=N_p+1}^{2N_p} I_{p,j}\mathbf{f}_{p,j}(\mathbf{r}), \tag{3.1}$$

where $I_{p,j}$, $j=1,\ldots,2N_p$, are unknown expansion coefficients of the currents on S_p, $p=1,\ldots,3$. The scattering matrix $\mathbf{Z}^i$ relates the discretized currents defined on equivalent surfaces touching to Ω_i to the discretized tested fields (scattered from Ω_i) on them. For an example subdomain Ω_c in Figure 3.1 (d), this relation is expressed via a matrix system as

$$\begin{bmatrix}\mathbf{Z}_{22}^c & \mathbf{Z}_{23}^c\\ \mathbf{Z}_{32}^c & \mathbf{Z}_{33}^c\end{bmatrix}\begin{bmatrix}\mathbf{I}_2\\ \mathbf{I}_3\end{bmatrix}=\begin{bmatrix}\mathbf{V}_2^{sca}\\ \mathbf{V}_3^{sca}\end{bmatrix}, \tag{3.2}$$

where the scattering matrix $\mathbf{Z}^c$ is formed by 2×2 scattering submatrices. $\mathbf{I}_p$ is the vector holding the unknown expansion coefficients of the discretized currents on S_p, $p\in\{2,3\}$. $\mathbf{V}_q^{sca}$ is the vector formed by the vectors of scattered electric fields $\mathbf{E}_q^{sca}$ and scattered magnetic fields $\mathbf{H}_q^{sca}$ tested on S_q, as $\mathbf{V}_q^{sca}=[\mathbf{E}_q^{sca};\mathbf{H}_q^{sca}]$, $q\in\{2,3\}$. The $2N_q\times 2N_p$ scattering submatrix $\mathbf{Z}_{qp}^c$, $q,p\in\{2,3\}$, maps the currents on S_p to the scattered fields on S_q by accounting for the wave propagation characteristics of the subdomain Ω_c. $2N_q$ is the number of RWG basis functions used to discretize the

currents on S_q. It is computed performing the following three steps for all basis functions on S_p:

Step 1: Generate a unit vector $\mathbf{I}_p$ with non-zero entry corresponding to a basis function on S_p and compute the fields generated via $\mathbf{I}_p$ and tested on Ω_c with RWG basis functions.

Step 2: Obtain the electric and magnetic currents on Ω_c induced by the fields computed in step 1.

Step 3: Compute the tested fields on S_q generated by the currents obtained in step 2.

These three steps are illustrated to obtain an example scattering submatrix $\mathbf{Z}_{32}^c$ in Figure 3.2 and described in detail as follows:

Step 1: The current densities $\mathbf{J}_p(\mathbf{r})$ and $\mathbf{M}_p(\mathbf{r})$ on S_p generate the electric and magnetic fields on Ω_c, $\mathbf{E}^c(\mathbf{r})$ and $\mathbf{H}^c(\mathbf{r})$, [Figure 3.2 (a)] via

$$\mathbf{E}^c(\mathbf{r}) = \mathcal{L}_1\left[\pm\mathbf{J}_p(\mathbf{r})\right] + \mathcal{K}_1\left[\pm\mathbf{M}_p(\mathbf{r})\right], \tag{3.3}$$

$$\mathbf{H}^c(\mathbf{r}) = -\mathcal{K}_1\left[\pm\mathbf{J}_p(\mathbf{r})\right] + \left(1/\eta_1^2\right)\mathcal{L}_1\left[\pm\mathbf{M}_p(\mathbf{r})\right]. \tag{3.4}$$

Here $\eta_1 = (\mu_1/\varepsilon_1)^{0.5}$, $\mathbf{r} \in \Omega_c$, and the signs of $\mathbf{J}_p(\mathbf{r})$ and $\mathbf{M}_p(\mathbf{r})$ are positive if they are defined on the side of S_p facing to Ω_c; otherwise, they are negative. The integral operators $\mathcal{L}_\alpha$ and $\mathcal{K}_\alpha$ are defined as

$$\mathcal{L}_\alpha\left[\mathbf{F}(\mathbf{r})\right] = j\omega\mu_\alpha \int_S \left(\bar{\mathbf{I}} + (k_\alpha^{-2}\nabla\nabla')\right) G_\alpha(\mathbf{r},\mathbf{r}')\mathbf{F}(\mathbf{r}')d\mathbf{r}', \tag{3.5}$$

$$\mathcal{K}_\alpha\left[\mathbf{F}(\mathbf{r})\right] = -\nabla\times\int_S G_\alpha(\mathbf{r},\mathbf{r}')\mathbf{F}(\mathbf{r}')d\mathbf{r}', \tag{3.6}$$

where $\omega = 2\pi f$, f is the frequency, $G_\alpha(\mathbf{r},\mathbf{r}') = \exp(-jk_\alpha|\mathbf{r}-\mathbf{r}'|)/(4\pi|\mathbf{r}-\mathbf{r}'|)$ is the Green's function [65] for the medium $\alpha\in\{0,1\}$ and $k_\alpha = \omega(\mu_\alpha\varepsilon_\alpha)^{0.5}$.

Step 2: The electric and magnetic fields on Ω_c, $\mathbf{E}^c(\mathbf{r})$ and $\mathbf{H}^c(\mathbf{r})$, (computed in step 1) induce the current densities $\mathbf{J}^c(\mathbf{r})$ and $\mathbf{M}^c(\mathbf{r})$ on Ω_c [Figure 3.2 (b)], which are obtained solving

$$-\mathbf{E}^c(\mathbf{r}) = \left(\mathcal{L}_0+\mathcal{L}_1\right)\left[\mathbf{J}^c(\mathbf{r})\right]+\left(\mathcal{K}_0+\mathcal{K}_1\right)\left[\mathbf{M}^c(\mathbf{r})\right], \tag{3.7}$$

$$-\mathbf{H}^c(\mathbf{r}) = -\left(\mathcal{K}_0+\mathcal{K}_1\right)\left[\mathbf{J}^c(\mathbf{r})\right]+\left(\frac{\mathcal{L}_0}{\eta_0^2}+\frac{\mathcal{L}_1}{\eta_1^2}\right)\left[\mathbf{M}^c(\mathbf{r})\right], \tag{3.8}$$

where $\mathbf{r}\in\Omega_c$. (3.7) and (3.8) are well-known Poggio-Muller-Chang-Harrington-Wu-Tsai (PMCHWT) equations [65] and are solved for $\mathbf{J}^c(\mathbf{r})$ and $\mathbf{M}^c(\mathbf{r})$, as detailed below.

Step 3: The current densities $\mathbf{J}^c(\mathbf{r})$ and $\mathbf{M}^c(\mathbf{r})$ generate the electric and magnetic fields on S_q, $\mathbf{E}_q(\mathbf{r})$ and $\mathbf{H}_q(\mathbf{r})$, [Figure 3.2 (c)] via

$$\mathbf{E}_q(\mathbf{r}) = \mathcal{L}_1\left[\mathbf{J}^c(\mathbf{r})\right]+\mathcal{K}_1\left[\mathbf{M}^c(\mathbf{r})\right], \tag{3.9}$$

$$\mathbf{H}_q(\mathbf{r}) = -\mathcal{K}_1\left[\mathbf{J}^c(\mathbf{r})\right]+\left(1/\eta_1^2\right)\mathcal{L}_1\left[\mathbf{M}^c(\mathbf{r})\right], \tag{3.10}$$

where $\mathbf{r}\in S_q$. Discretizing the currents in (3.3), (3.4), and (3.7)-(3.10) (as in (3.1)) and Galerkin testing the resulting equations yields $2N_q\times 2N_p$ scattering submatrix $\mathbf{Z}_{qp}^c$ that relates currents on S_p to fields on S_q as

$$\mathbf{Z}_{qp}^{c} = \mathbf{C}_{q}^{c}(\mathbf{B}^{c})^{-1}\mathbf{A}_{p}^{c}. \tag{3.11}$$

Here $\mathbf{A}_{p}^{c}$, $\mathbf{B}^{c}$, and $\mathbf{C}_{q}^{c}$ are the matrices of discretized operators with dimensions $2N_c \times 2N_p$, $2N_c \times 2N_c$, and $2N_q \times 2N_c$ (obtained in steps 1, 2, and 3), respectively, and their entries are provided in Section 3.2.3. $2N_c$ is the number of RWG basis functions used to discretize the currents on Ω_c. Inverting $\mathbf{B}^{c}$ in (3.11) via classical direct methods is computationally expensive when N_c is large (more than tens/hundreds of thousands). To this end, the proposed simulator leverages a butterfly-based direct solver for computing the compressed inverse (LU factors) of $\mathbf{B}^{c}$, realizing significant savings when compared to conventional direct solvers for inverting $\mathbf{B}^{c}$. Specifically, the solver first hierarchically decomposes the discretized PWCHWT impedance matrix $\mathbf{B}^{c}$ and compresses its off-diagonal blocks via butterflies [66]. Next, the solver computes a compressed LU factorization of $\mathbf{B}^{c}$ via recursively computing sums and products of butterfly-compressed partial LU factors as new butterfly representations, which is augmented by a fast matrix-vector multiplication-based low-complexity randomized butterfly scheme. The details of this solver can be found in [53]. Once $(\mathbf{B}^{c})^{-1}$ is obtained, the remaining computationally costly operations to obtain $\mathbf{Z}_{qp}^{c}$ are the multiplications of matrices $\mathbf{A}_{p}^{c}$ and $\mathbf{C}_{q}^{c}$ with a vector while computing $\mathbf{Z}_{qp}^{c}\mathbf{I}_{p}$; such operations are accelerated by an FMM-FFT scheme [27, 28, 54, 55].

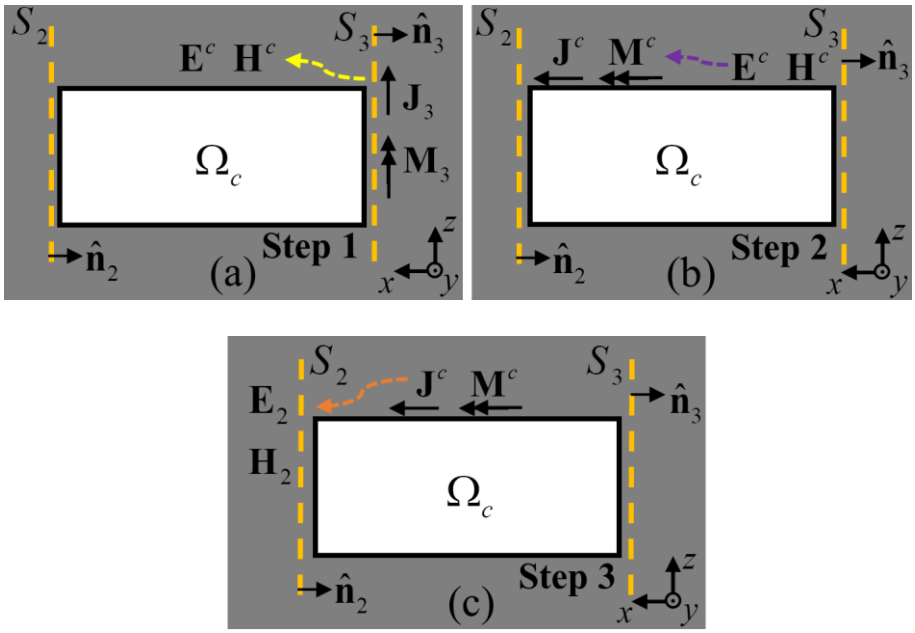

Figure 3.2 Procedure for computing scattering submatrix $\mathbf{Z}_{23}^3$. (a) Step 1: coefficient of a basis function on S_3 is set to unit and the fields produced by this current are tested on Ω_c. (b) Step 2: the currents on Ω_c due to the incident fields obtained in step 1 are solved. (c) Step 3: the fields produced by the currents obtained in step 2 are tested on S_2.

3.2.3 Entries of Equation 3.11

Let $\langle \cdot, \cdot \rangle$ denote standard inner product. Currents $\mathbf{J}^c(\mathbf{r})$ and $\mathbf{M}^c(\mathbf{r})$, defined on subdomain Ω_c, are discretized by $2N_c$ RWG basis functions $\mathbf{f}_n(\mathbf{r})$ as

$$\mathbf{J}^c(\mathbf{r}) = \sum_{n=1}^{N_c} I_n^c \mathbf{f}_n(\mathbf{r}), \quad \mathbf{M}^c(\mathbf{r}) = \sum_{n=1+N_c}^{2N_c} I_n^c \mathbf{f}_n(\mathbf{r}) \tag{3.12}$$

Currents $\mathbf{J}_p(\mathbf{r})$ and $\mathbf{M}_p(\mathbf{r})$ on S_p, $p = \{2,3\}$, are discretized by $2N_p$ RWG basis functions $\mathbf{f}_{p,j}(\mathbf{r})$ as

$$\mathbf{J}_p(\mathbf{r}) = \sum_{j=1}^{N_p} I_{p,j} \mathbf{f}_{p,j}(\mathbf{r}), \quad \mathbf{M}_p(\mathbf{r}) = \sum_{j=N_p+1}^{2N_p} I_{p,j} \mathbf{f}_{p,j}(\mathbf{r}) \tag{3.13}$$

Currents $\mathbf{J}_q(\mathbf{r})$ and $\mathbf{M}_q(\mathbf{r})$ on S_q, $q=\{2,3\}$ are discretized by $2N_q$ RWG basis functions $\mathbf{f}_{q,k}(\mathbf{r})$ as

$$\mathbf{J}_q(\mathbf{r})=\sum_{k=1}^{N_q} I_{q,k}\mathbf{f}_{q,k}(\mathbf{r}),\ \mathbf{M}_q(\mathbf{r})=\sum_{k=N_q+1}^{2N_q} I_{q,k}\mathbf{f}_{q,k}(\mathbf{r}) \tag{3.14}$$

Note that when $p=q$, the basis functions on S_p are identical to the ones on S_q. The entries of $\mathbf{A}_p^c$, $\mathbf{B}^c$ and $\mathbf{C}_q^c$ are

$$\left\{\mathbf{A}_p^c\right\}_{nj}=\left\langle \mathbf{f}_n(\mathbf{r}),\mathcal{L}_1\left[\mathbf{f}_{p,j}(\mathbf{r})\right]\right\rangle_{\Omega_c},\ 1\le n\le N_c,1\le j\le N_p \tag{3.15}$$

$$\left\{\mathbf{A}_p^c\right\}_{nj}=\left\langle \mathbf{f}_n(\mathbf{r}),\mathcal{K}_1\left[\mathbf{f}_{p,j}(\mathbf{r})\right]\right\rangle_{\Omega_c},\ 1\le n\le N_c,1+N_p\le j\le 2N_p \tag{3.16}$$

$$\left\{\mathbf{A}_p^c\right\}_{nj}=\left\langle \mathbf{f}_n(\mathbf{r}),-\mathcal{K}_1\left[\mathbf{f}_{p,j}(\mathbf{r})\right]\right\rangle_{\Omega_c},\ 1+N_c\le n\le 2N_c,1\le j\le N_p \tag{3.17}$$

$$\left\{\mathbf{A}_p^c\right\}_{nj}=\left\langle \mathbf{f}_n(\mathbf{r}),\frac{1}{\eta_1}\mathcal{L}_1\left[\mathbf{f}_{p,j}(\mathbf{r})\right]\right\rangle_{\Omega_c},\ 1+N_c\le n\le 2N_c,1+N_p\le j\le 2N_p \tag{3.18}$$

$$\left\{\mathbf{B}^c\right\}_{mn}=\left\langle \mathbf{f}_m(\mathbf{r}),(\mathcal{L}_0+\mathcal{L}_1)\left[\mathbf{f}_n(\mathbf{r})\right]\right\rangle_{\Omega_c},\ 1\le m\le N_c,1\le n\le N_c \tag{3.19}$$

$$\left\{\mathbf{B}^c\right\}_{mn}=\left\langle \mathbf{f}_m(\mathbf{r}),(\mathcal{K}_0+\mathcal{K}_1)\left[\mathbf{f}_n(\mathbf{r})\right]\right\rangle_{\Omega_c},\ 1\le m\le N_c,1+N_c\le n\le 2N_c \tag{3.20}$$

$$\left\{\mathbf{B}^c\right\}_{mn}=\left\langle \mathbf{f}_m(\mathbf{r}),-(\mathcal{K}_0+\mathcal{K}_1)\left[\mathbf{f}_n(\mathbf{r})\right]\right\rangle_{\Omega_c},\ 1+N_c\le m\le 2N_c,1\le n\le N_c \tag{3.21}$$

$$\left\{\mathbf{B}^c\right\}_{mn}=\left\langle \mathbf{f}_m(\mathbf{r}),(\frac{\mathcal{L}_0}{\eta_0^2}+\frac{\mathcal{L}_1}{\eta_1^2})\left[\mathbf{f}_n(\mathbf{r})\right]\right\rangle_{\Omega_c},\ 1+N_c\le n\le 2N_c,1+N_c\le n\le 2N_c \tag{3.22}$$

$$\left\{\mathbf{C}_q^c\right\}_{kn}=\left\langle \mathbf{f}_{q,k}(\mathbf{r}),\mathcal{L}_1\left[\mathbf{f}_n(\mathbf{r})\right]\right\rangle_{S_q},\ 1\le k\le N_q,1\le n\le N_c \tag{3.23}$$

$$\left\{\mathbf{C}_q^c\right\}_{kn} = \left\langle \mathbf{f}_{q,k}(\mathbf{r}), \mathcal{K}_1\left[\mathbf{f}_n(\mathbf{r})\right]\right\rangle_{S_q},\ 1 \le k \le N_q, 1+N_c \le n \le 2N_c \tag{3.24}$$

$$\left\{\mathbf{C}_q^c\right\}_{kn} = \left\langle \mathbf{f}_{q,k}(\mathbf{r}), -\mathcal{K}_1\left[\mathbf{f}_n(\mathbf{r})\right]\right\rangle_{S_q},\ 1+N_q \le k \le 2N_q, 1 \le n \le N_c \tag{3.25}$$

$$\left\{\mathbf{C}_q^c\right\}_{kn} = \left\langle \mathbf{f}_{q,k}(\mathbf{r}), \frac{\mathcal{L}_1}{\eta_1^2}\left[\mathbf{f}_n(\mathbf{r})\right]\right\rangle_{S_q},\ 1+N_q \le k \le 2N_q, 1+N_c \le n \le 2N_c \tag{3.26}$$

Here, the $\mathbf{B}^c$ matrix is formed by Galerkin testing.

3.2.4 Inter-domain System

The scattering matrices computed to characterize the EM wave propagation in each subdomain are used to form the inter-domain system of equations that accounts for the interactions between equivalent surfaces. The interactions between equivalent surfaces that are not attached to the same subdomain are not included in inter-domain system since those are negligible due to the highly lossy background. The interactions between equivalent surfaces attached to the same subdomain are included in inter-domain system by carefully accounting for the impressed sources in subdomains and induced currents on equivalent surfaces and by imposing the boundary conditions on the equivalent surfaces, as detailed below.

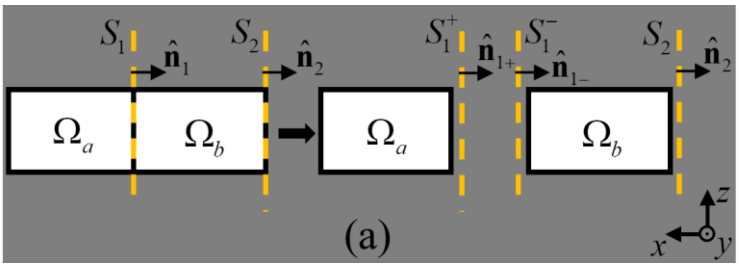

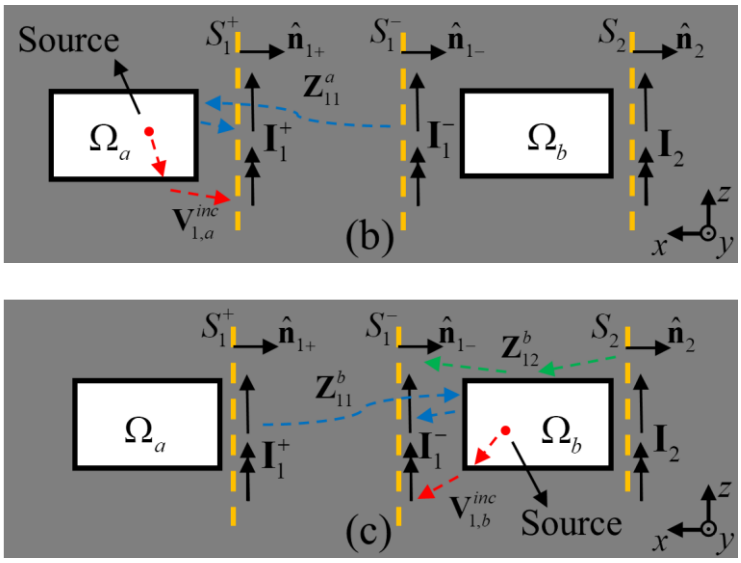

Figure 3.3 (a) Separation of subdomains Ω_a and Ω_b. (b) The incident fields on S_1^+. Red dash line represents the fields due to sources in Ω_a; blue dash line represents the fields radiated by currents on S_1^- and scattered by Ω_a. (c) The incident fields on S_1^-. Red dash line represents the fields due to sources in Ω_b; blue dash line represents the fields radiated by currents on S_1^+ and scattered by Ω_b; green dash line represents the fields radiated by currents on S_2 and scattered by Ω_b.

Consider the equivalent surface S_1 (in Figure 3.1 (d)) attached to Ω_a and Ω_b [Figure 3.3]. This equivalent surface interacts with itself and S_2. To illustrate its self-interaction, S_1 is duplicated as S_1^+ and S_1^- [Figure 3.3 (a)]. While the self-interaction of S_1 is represented as the interaction between S_1^+ and S_1^-, the interaction between S_1 and S_2 is replaced by the interaction between S_1^- and S_2 [Figure 3.3 (a)]. Note that S_1^+ does not interact with S_2 since they are not attached to the same subdomain. Furthermore, the vectors holding the unknown expansion coefficients of the currents on S_1^+ and S_1^- are denoted by $\mathbf{I}_1^+$ and $\mathbf{I}_1^-$, respectively. To obtain $\mathbf{I}_1^+$, the fields impinging to the S_1^+ should

be determined. In fact, these are (i) the incident fields generated by possible impressed sources in Ω_a and (ii) the fields generated by the currents on S_1^-, which travel throughout Ω_a, impinge to the S_1^+, and thereby are characterized by scattering submatrix $\mathbf{Z}_{11}^a$. By taking into account these incident fields, the currents on S_1^+ are obtained by solving the PMCHWT equations for S_1^+, which reads

$$\mathbf{D}_1\mathbf{I}_1^+ = \mathbf{V}_{1,a}^{inc} - \mathbf{Z}_{11}^a\mathbf{I}_1^- \tag{3.27}$$

where $\mathbf{V}_{1,a}^{inc}$ is the tested incident fields on S_1^+ due to impressed sources in Ω_a and $\mathbf{D}_1$ is the discretized PMCHWT matrix for S_1 (see [65] for details). Similarly, the currents on S_1^- are obtained by accounting for the incident fields due to impressed sources in Ω_b and the fields generated by the currents on S_1^+ and S_2, which travel throughout Ω_b, impinge to the S_1^-, and thereby are characterized by scattering submatrices $\mathbf{Z}_{11}^b$ and $\mathbf{Z}_{12}^b$, respectively [Figure 3.3 (c)]. By considering these incident fields, the currents on S_1^+ are obtained via

$$\mathbf{D}_1\mathbf{I}_1^- = \mathbf{V}_{1,b}^{inc} - \mathbf{Z}_{11}^b\mathbf{I}_1^+ - \mathbf{Z}_{12}^b\mathbf{I}_2 \tag{3.28}$$

where $\mathbf{V}_{1,b}^{inc}$ is the tested incident fields on S_1^- due to impressed sources in Ω_b. Since S_1^+ and S_1^- coincide, currents on both surfaces equal to each other ($\mathbf{I}_1 = \mathbf{I}_1^+ = \mathbf{I}_1^-$). Denoting $\overline{\mathbf{Z}}_{11}^a = \mathbf{Z}_{11}^a + \mathbf{D}_1$, $\overline{\mathbf{Z}}_{11}^b = \mathbf{Z}_{11}^b + \mathbf{D}_1$, and summing (3.27) and (3.28) yield the inter-domain equation for S_1

$$\left(\overline{\mathbf{Z}}_{11}^{a}+\overline{\mathbf{Z}}_{11}^{b}\right)\mathbf{I}_1+\mathbf{Z}_{12}^{b}\mathbf{I}_2=\mathbf{V}_1^{inc} \tag{3.29}$$

where $\mathbf{V}_1^{inc}=\mathbf{V}_{1,a}^{inc}+\mathbf{V}_{1,b}^{inc}$. By extending the above procedure to all other equivalent surfaces, the inter-domain system for the example tunnel in Fig.1 is obtained as

$$\begin{bmatrix} \overline{\mathbf{Z}}_{11}^{a}+\overline{\mathbf{Z}}_{11}^{b} & \mathbf{Z}_{12}^{b} & 0 \\ \mathbf{Z}_{21}^{b} & \overline{\mathbf{Z}}_{22}^{b}+\overline{\mathbf{Z}}_{22}^{c} & \mathbf{Z}_{23}^{c} \\ 0 & \mathbf{Z}_{32}^{c} & \overline{\mathbf{Z}}_{33}^{c}+\overline{\mathbf{Z}}_{33}^{d} \end{bmatrix}\begin{bmatrix} \mathbf{I}_1 \\ \mathbf{I}_2 \\ \mathbf{I}_3 \end{bmatrix}=\begin{bmatrix} \mathbf{V}_1^{inc} \\ \mathbf{V}_2^{inc} \\ \mathbf{V}_3^{inc} \end{bmatrix}, \tag{3.30}$$

where $\mathbf{V}_p^{inc}=[\mathbf{E}_p^{inc};\mathbf{H}_p^{inc}]$, $p=1,\ldots,3$, is the vector of incident electric and magnetic fields on S_p due to impressed sources in the subdomains touching S_p . It is zero if all subdomains touching to S_p are (impressed) source-free. Similar equations can be easily derived for tunnels and galleries with more subdomains attached to more than two equivalent surfaces. Once the inter-domain system (3.30) is solved, the currents on each equivalent surface are used to compute the currents on Ω_i (and hence fields anywhere inside Ω_i) via steps 1 and 2 of the procedures to obtain scattering matrix. For example, the current coefficients $\mathbf{I}^b$ on Ω_b (in Figure 3.1 (d)) are computed as

$$\mathbf{I}^b=(\mathbf{B}^b)^{-1}\mathbf{A}_1^b\mathbf{I}_1+(\mathbf{B}^b)^{-1}\mathbf{A}_2^b\mathbf{I}_2. \tag{3.31}$$

In case one subdomain contains impressed sources, the incident fields generated by impressed sources should be accounted for while computing the currents pertinent to that subdomain.

When the repetitive execution of an EM simulator for many different excitations is required for uncertainty quantification or optimum wireless node placement studies, the

proposed DD based SIE simulator only updates the right hand side of (3.30) and re-solves the inter-domain system for new excitations during the online stage of the simulator. Note that the scattering matrices of individual subdomains are computed only once and stored during the offline stage of the simulator. Furthermore, many mine tunnels or galleries have repeated geometric features and therefore it is reasonable to assume that many subdomains of mine tunnels and galleries are identical. Therefore, the scattering matrices for all subdomains decomposing a large mine environment can be obtained by characterizing only a few different subdomains.

3.2.5 Subdomain Combining Scheme

When the electrically large mine tunnels and galleries are divided into hundreds of subdomains, solving the inter-domain system could be computationally expensive. To this end, an efficient scheme that combines the adjacent identical subdomains and alleviates this computational burden is proposed here.

Consider two adjacent subdomains Ω_b and Ω_c (in Figure 3.1 (d)) with associated equivalent surfaces S_p, $p=1,\ldots,3$. As derived in (3.2), the relations between currents and fields on these equivalent surfaces are expressed via scattering matrices of these subdomains as

$$\begin{bmatrix} \mathbf{Z}_{11}^{b} & \mathbf{Z}_{12}^{b} & 0 \\ \mathbf{Z}_{21}^{b} & \overline{\mathbf{Z}}_{22}^{b}+\overline{\mathbf{Z}}_{22}^{c} & \mathbf{Z}_{23}^{c} \\ 0 & \mathbf{Z}_{32}^{c} & \mathbf{Z}_{33}^{c} \end{bmatrix} \begin{bmatrix} \mathbf{I}_1 \\ \mathbf{I}_2 \\ \mathbf{I}_3 \end{bmatrix} = \begin{bmatrix} \mathbf{V}_1^{sca} \\ \mathbf{V}_2^{sca} \\ \mathbf{V}_3^{sca} \end{bmatrix} \tag{3.32}$$

By comparing (3.30) and (3.32), one can found that $\mathbf{V}_2^{sca} = \mathbf{V}_2^{inc}$. Hence, when there is no source inside these subdomains, i.e. $\mathbf{V}_2^{sca} = 0$, $\mathbf{I}_2$ can be eliminated from (3.32). The resulting equation is

$$\begin{bmatrix} \mathbf{Z}_{11}^{new} & \mathbf{Z}_{13}^{new} \\ \mathbf{Z}_{31}^{new} & \mathbf{Z}_{33}^{new} \end{bmatrix} \begin{bmatrix} \mathbf{I}_1 \\ \mathbf{I}_3 \end{bmatrix} = \begin{bmatrix} \mathbf{V}_1^{sca} \\ \mathbf{V}_3^{sca} \end{bmatrix} \tag{3.33}$$

where

$$\mathbf{Z}_{11}^{new} = \mathbf{Z}_{11}^{b} - \mathbf{Z}_{12}^{b} \left(\overline{\mathbf{Z}}_{22}^{b} + \overline{\mathbf{Z}}_{22}^{c} \right)^{-1} \mathbf{Z}_{21}^{b} \tag{3.34}$$

$$\mathbf{Z}_{13}^{new} = -\mathbf{Z}_{12}^{b} \left(\overline{\mathbf{Z}}_{22}^{b} + \overline{\mathbf{Z}}_{22}^{c} \right)^{-1} \mathbf{Z}_{23}^{c} \tag{3.35}$$

$$\mathbf{Z}_{31}^{new} = -\mathbf{Z}_{32}^{c} \left(\overline{\mathbf{Z}}_{22}^{b} + \overline{\mathbf{Z}}_{22}^{c} \right)^{-1} \mathbf{Z}_{21}^{b} \tag{3.36}$$

$$\mathbf{Z}_{33}^{new} = \mathbf{Z}_{33}^{c} - \mathbf{Z}_{32}^{c} \left(\overline{\mathbf{Z}}_{22}^{b} + \overline{\mathbf{Z}}_{22}^{c} \right)^{-1} \mathbf{Z}_{23}^{c} \tag{3.37}$$

Note that (3.33) characterizes the wave propagation between S_1 and S_3. It implies that the two subdomains are combined and treated as one while $\mathbf{Z}_{11}^{new}$, $\mathbf{Z}_{13}^{new}$, $\mathbf{Z}_{31}^{new}$, and $\mathbf{Z}_{33}^{new}$ are new scattering submatrices of the scattering matrix $\mathbf{Z}^{new}$ for the combined subdomain. A reduced inter-domain system of equations can then be formed using $\mathbf{Z}^{new}$ as

$$\begin{bmatrix} \overline{\mathbf{Z}}_{11}^{a} + \overline{\mathbf{Z}}_{11}^{new} & \mathbf{Z}_{13}^{new} \\ \mathbf{Z}_{31}^{new} & \overline{\mathbf{Z}}_{33}^{new} + \overline{\mathbf{Z}}_{33}^{d} \end{bmatrix} \begin{bmatrix} \mathbf{I}_1 \\ \mathbf{I}_3 \end{bmatrix} = \begin{bmatrix} \mathbf{V}_1^{inc} \\ \mathbf{V}_3^{inc} \end{bmatrix} \tag{3.38}$$

where $\overline{\mathbf{Z}}_{11}^{new} = \mathbf{Z}_{11}^{new} + \mathbf{D}_1$ and $\overline{\mathbf{Z}}_{33}^{new} = \mathbf{Z}_{33}^{new} + \mathbf{D}_3$. The matrix system in (3.38) is apparently smaller than that in (3.30). After $\mathbf{I}_1$ and $\mathbf{I}_3$ are solved, $\mathbf{I}_2$ can be computed via

$$\mathbf{I}_2 = -\left(\overline{\mathbf{Z}}_{22}^{b} + \overline{\mathbf{Z}}_{22}^{c}\right)^{-1}\left(\mathbf{Z}_{21}^{b}\mathbf{I}_1 + \mathbf{Z}_{23}^{c}\mathbf{I}_3\right) \tag{3.39}$$

Repeating this procedure permits merging any number of source-free subdomains into one subdomain and reduce the dimensionality of the inter-domain system of equation. The reduced inter-domain system is oftentimes small enough to be directly inverted via direct methods regardless of the tunnel's length. When most of the subdomains are source-free and identical, the subdomain combination operation can be performed in a recursive manner and consequently the computational cost of subdomain combining scheme scales logarithmically with the number of subdomains. It is noteworthy to mention that, in case the impressed sources reside in the same subdomain while performing the analyses with different excitations, the subdomain combining procedure is executed only once for solving all different excitations.

3.2.6 Cost Analysis

The computational cost and memory requirement of offline and online stages of the proposed DD based SIE simulator are analyzed as follows.

3.2.6.1 Computing Scattering Matrix of a Subdomain (Offline Stage)

The computation of a scattering submatrix $\mathbf{Z}_{qp}^{i}$ for a subdomain Ω_i, ($i \in a,b,c,d$ in Figure 3.1 (d)) requires multiplication of $2N_p$ unit vectors with $\mathbf{C}_q^i(\mathbf{B}^i)^{-1}\mathbf{A}_p^i$. In steps

1 and 3, the matrix-vector multiplications are computed via the FMM-FFT acceleration scheme with maximum $O(N_i \log N_i)$ computational and memory resources for one multiplication [28], given that $2N_i$ is the number of basis functions used to discretize currents on Ω_i. In step 2, inversion of $\mathbf{B}^i$ and its multiplication with vectors from step 1 are performed via the butterfly-based direct solver, which requires $O(N_i^{1.5} \log N_i)$ and $O(N_i \log^2 N_i)$ computational and memory resources for computing the inverse and $O(N_i \log N_i)$ computational resources for multiplying $(\mathbf{B}^i)^{-1}$ with the vectors [53]. By summing these estimates for three steps and considering that $N_p N_i >> N_i^{1.5}$ in general, the total computational cost U_{sub} and memory requirement M_{sub} for computing one scattering matrix scale as

$$U_{sub} = O(N_p N_i \log N_i) \tag{3.40}$$

$$M_{sub} = O(N_i \log N_i) \tag{3.41}$$

3.2.6.2 Solving Inter-Domain System (Online Stage)

When the subdomain combining scheme is used, the inter-domain system is solved in two phases: combining the subdomains and solving the reduced inter-domain system.

In the first phase, combining a pair of subdomains calls for one matrix inversion and four matrix-matrix multiplications, requiring $O(N_p^3)$ and $O(N_p^2)$ computational and memory resources, respectively. Since most of the subdomains are identical, subdomains

are combined in a recursive manner and abovementioned operations are repeated $\log N_{sub}$ times, where N_{sub} is the number of subdomains. Therefore, the computational cost and memory requirement of the first phase scale as $O(N_p^3 \log N_{sub})$ and $O(N_p^2 \log N_{sub})$.

In the second phase, the reduced inter-domain system is formed using a small number of equivalent surfaces regardless of N_{sub} and solved by a classical direct method. In case that a direct method is not applicable due to dimensionality of the reduced inter-domain system, an iterative solver [36] is used for inversion. Hence, the computational cost and memory requirement of the second phase scale as maximum $O(N_p^3)$ and $O(N_p^2)$, respectively. To this end, the total computational cost U_{int} and memory requirement M_{int} of solving inter-domain system with subdomain combining scheme are

$$U_{\text{int}} = O(N_p^3 \log N_{sub}), \tag{3.42}$$

$$M_{\text{int}} = O(N_p^2 \log N_{sub}). \tag{3.43}$$

It is clear in (3.42) and (3.43) that the computational cost and memory requirement scale logarithmically with the tunnel length. When the subdomain combining scheme is not used, the sparse inter-domain system of size $N_p N_{sur} \times N_p N_{sur}$ is solved via an iterative solver [36], where N_{sur} is the number of equivalent surfaces. Note that the interactions between equivalent surfaces touching to the same subdomains are only included in inter-domain system and the number of scattering submatrices pertinent to each equivalent surface is bounded by a small constant. Therefore, the computational cost

and memory requirement of solving inter-domain systems without subdomain combining scheme are

$$U_{\text{int}} = O(N_p^2 N_{sur}) \tag{3.44}$$

$$M_{\text{int}} = O(N_p^2 \bar{N}_{sur}) \tag{3.45}$$

where $\bar{N}_{sur}$ is the number of equivalent surfaces attached to non-identical subdomains. Due to the repeated features of mine layouts, $\bar{N}_{sur}$ is oftentimes a small number and does not depend on N_{sub} or N_{sur}. Therefore, M_{int} scales with $O(N_p^2)$ for many mine layouts and remains constant with increasing tunnel length. Note that solving the inter-domain system with subdomain combining scheme requires more memory resources than solving inter-domain system without it. On the other hand, solution with subdomain combining scheme is much faster than the solution without it, given that N_p is oftentimes a small number (due to the small electrical size of tunnel's cross sections) and iterative solvers generally have a large leading constant. The estimates of computational cost and memory requirements provided in (3.42) - (3.45) are numerically validated in numerical results.

For electrically large mine environments, N_p and N_i (as well as N_{sur} and N_{sub}) are insignificant compared to the number of basis functions needed to discretize the currents on the walls of whole mine tunnels or galleries. Therefore, the proposed simulator (even without subdomain combining scheme) is much faster and more memory efficient compared to conventional fast full-wave EM simulators with quasi-linear complexity, as numerically proven in numerical results. Moreover, when the simulator is executed repetitively for different excitations, only the inter-domain system needs to be

re-solved, leading to even more saving on the computational resources, as shown in the numerical results.

3.3 Numerical results and Discussions

This section first demonstrates the accuracy, efficiency, and applicability of the proposed DD based SIE simulator via its application to the EM wave characterization in various types of mine tunnels and gallery and statistical characterization of EM wave propagation in an electrically large mine tunnel. Then, it compares the computational cost and memory requirement of the proposed simulator with those of an FMM-FFT accelerated SIE (FMM-FFT-SIE) simulator. In all examples below, mine tunnels has air inside and are surrounded by ore with relative permittivity $\varepsilon_r = 8.9$, relative permeability $\mu_r = 1$, and conductivity $\sigma = 0.15$ S/m , where ε_r , μ_r , σ are related to ε_1 and μ_1 via $\mu_1 = \mu_r \mu_0$ and $\varepsilon_1 = \varepsilon_0 \varepsilon_r - j\sigma/\omega$. The mine tunnels are excited by an infinitesimal electric dipole with unit moment. The electric field values obtained by the proposed simulator and other methods are normalized to their maxima and converted to power values which are expressed in logarithmic units. The proposed simulator was implemented using hybrid message passing interface/open multiprocessing (MPI/OpenMP) standards and executed on a cluster of dual hexacore X5650 Intel processors located at the Center for Advanced Computing, University of Michigan, Ann Arbor, MI, USA.

3.3.1 Straight Tunnels

To show both the accuracy and applicability of the proposed simulator, it is applied to characterization of EM wave propagation in three different straight tunnels: a 600 m - long empty arched tunnel, a 200 m - long empty rectangular tunnel with rough walls, and a 400 m - long rectangular tunnel with a partial cave-in. Specifications of the simulations performed for each scenario are listed in Table 3-1. The dipole is positioned at (50.2, 0.915, 1.22) m in the arched tunnel scenario and at (50.2, 0.925, 1.12) m in all rectangular tunnel scenarios.

3.3.1.1 Empty Arched Tunnel

A 600 m - long arched tunnel is excited by a $z-$ (vertically) or $y-$ (horizontally) oriented dipole at 455 MHz or 915 MHz (4 cases) [Figure 3.4 (a)]. In this scenario, the tunnel is decomposed into 200 identical 3 m - long subdomains for analysis at 455 MHz and 240 identical 2.5 - m long subdomains for analysis at 915 MHz; only one scattering matrix is computed for each frequency. At lower and higher frequencies, subdomains are discretized using 50,202 and 172,038 RWG basis functions, while the equivalent surfaces are discretized using 12,958 and 44,910 RWG basis functions, respectively. Power values on a line connecting (51.2, 0.915, 1.22) m and (600, 0.915, 1.22) m computed by the proposed simulator are compared with the measurement data in [67, 68] after applying the normalizations accounting for different excitation mechanism [Figure 3.4 (b)-(e)]. Power values computed by the proposed DD based SIE simulator are in good agreement with the measurement data, demonstrating the accuracy of the simulator. The dynamic

ranges of the simulator and measurements are around 120 dB and 100 dB, respectively, and are reflected in Figure 3.4 (b), (c), and (e).

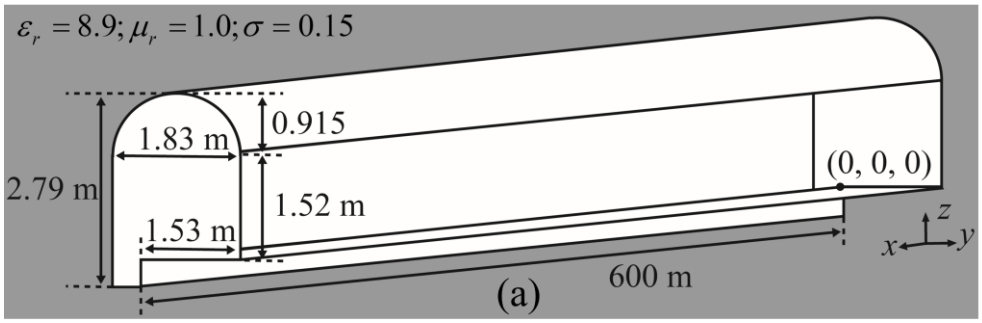

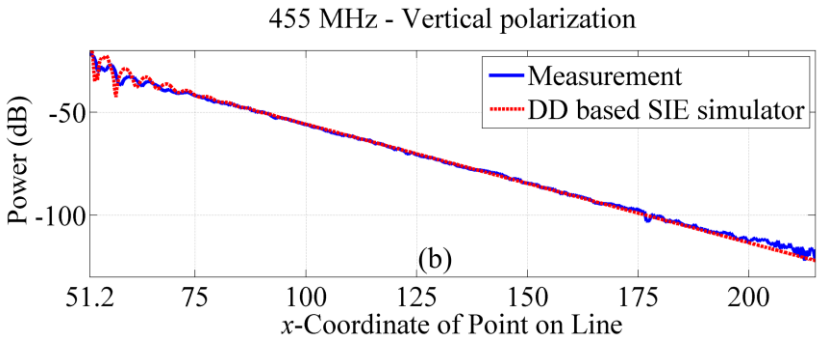

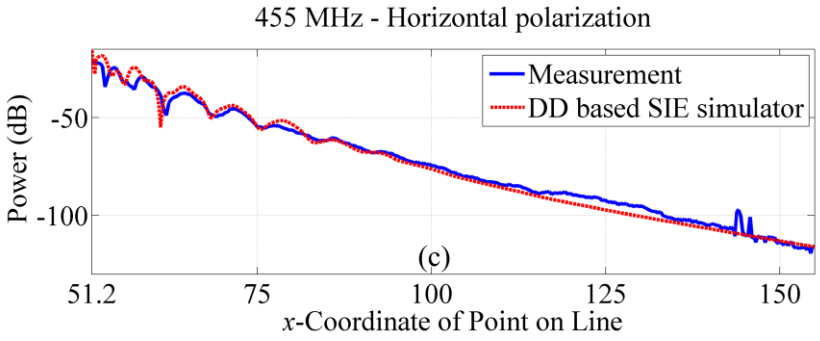

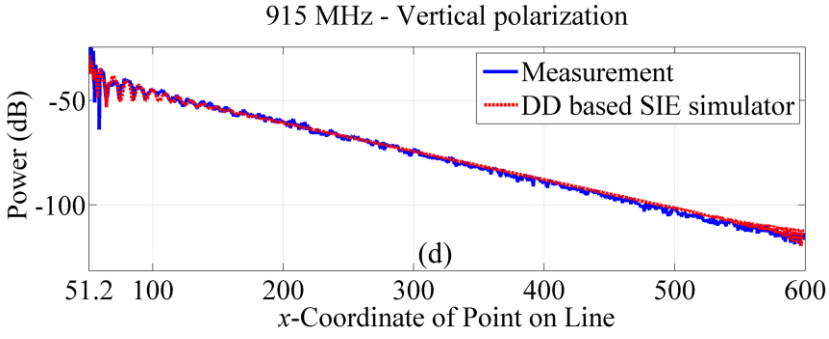

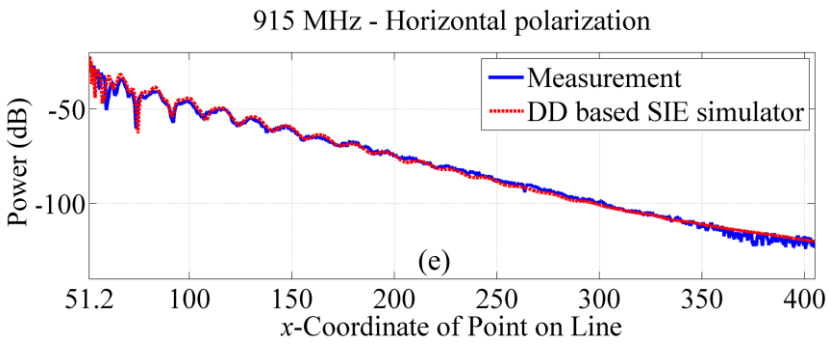

Figure 3.4 (a) The geometry of a 600 m - long arched tunnel. The power values computed by the proposed simulator are compared to measurement data for (b) vertically and (c) horizontally oriented dipole at 455 MHz, and for (d) vertically and (e) horizontally oriented dipole at 915 MHz.

3.3.1.2 Empty Rectangular Tunnel with Rough Walls

A 201 m - long rectangular tunnel with rough walls is excited by a $z-$directed dipole at 455 MHz [Figure 3.5 (a)]. The tunnel is decomposed into 67 subdomains with length of 3 m. The subdomains and equivalent surfaces are discretized using 45,648 and 10,952 RWG basis functions, respectively. Tunnel walls are formed by rough surfaces with root mean square height of 0.1 m and correlation length of 0.5 m [69]. Five subdomains generated by distinct random profiles are randomly cascaded to form the tunnel. Therefore, only five scattering matrices are computed. The power values on a line connecting (51.0, 0.925, 1.12) m to (200, 0.925, 1.12) m (tunnel center) are computed by the proposed simulator [Figure 3.5 (b)]. The computed values are compared to those obtained by the proposed simulator and the multi-modal decomposition [39] for the same tunnel but with the smooth walls [Figure 3.5 (b)]. Apparently, the decay of power values in the tunnel with rough walls is faster than that in the tunnel with smooth walls. The power value at x=175 m in the tunnel with rough walls is 6.03 dB below that in the

tunnel with smooth walls. Furthermore, the results obtained by the proposed simulator and multi-modal decomposition for the tunnel with smooth walls show perfect agreement and further validate the accuracy of the proposed simulator. It's noteworthy to mention the inter-domain systems for the analyses of the tunnels with smooth and rough walls are solved by the subdomain combining scheme and an iterative solver [36], respectively. It's clear in Table 3-1 that the solution with subdomain combining scheme requires less computational time but more memory compared to solution with iterative solver.

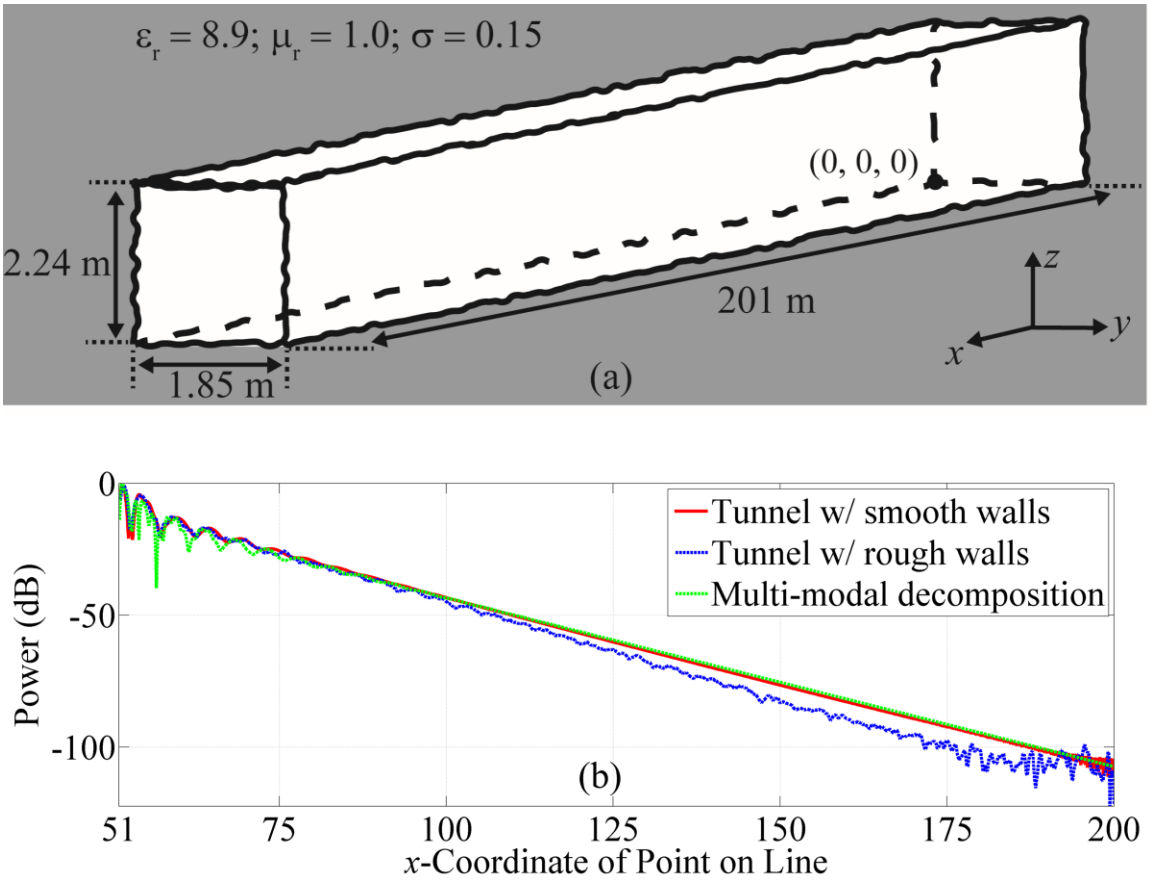

Figure 3.5 (a) The geometry of a 201 m - long rectangular tunnel with rough walls. (b) The power values in the center of tunnel with rough and smooth walls computed by the proposed simulator are compared with those obtained by multi-modal decomposition for tunnel with smooth walls.

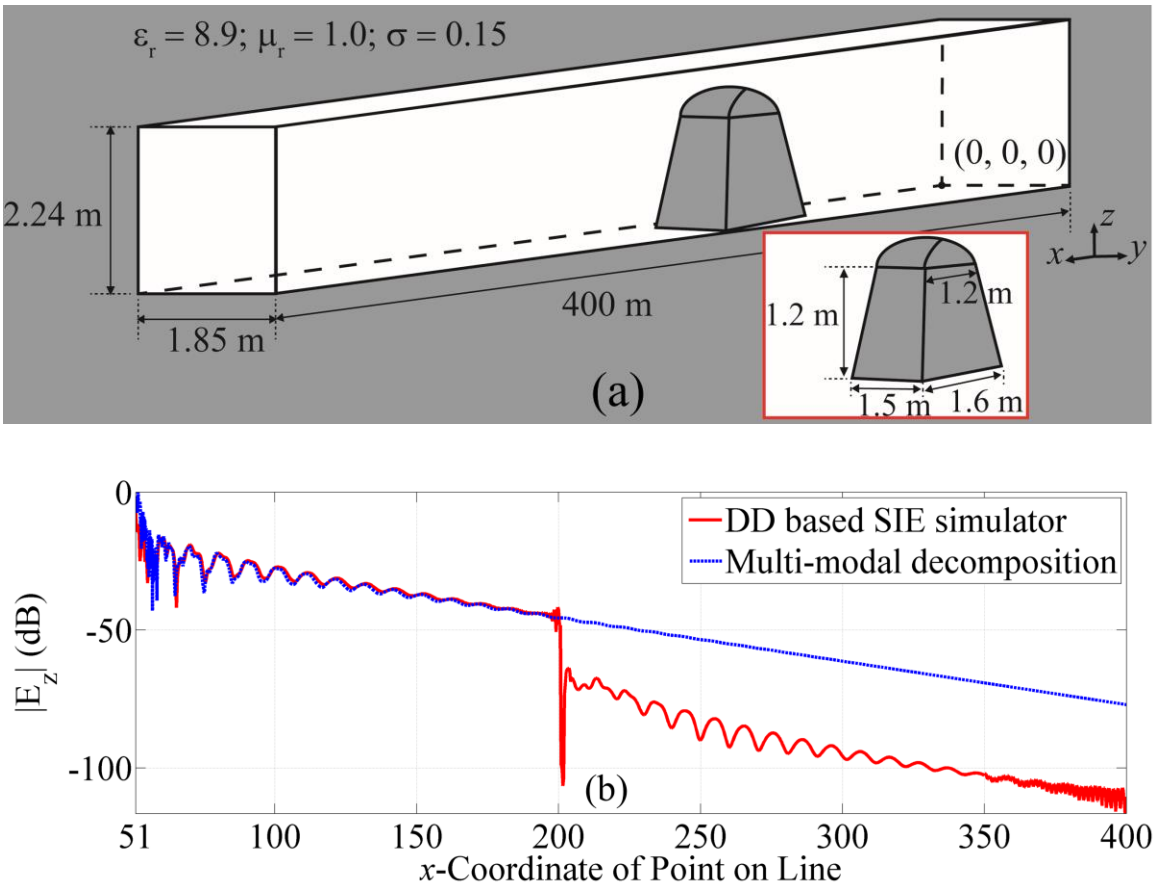

Figure 3.6 (a) The geometry of a 400m-long rectangular tunnel with a partial cave-in. (b) The power values on a line in the middle of the tunnel computed by the proposed simulator for the tunnel with cave-in and by multi-mode decomposition method for the empty tunnel.

3.3.1.3 Rectangular Tunnel with Cave-in

A 400 m - long rectangular tunnel with a partial cave-in is excited by a $z-$directed dipole at 915 MHz [Figure 3.6 (a)]. The tunnel is decomposed into 159 identical 2.5 m - long empty subdomains and one 2.5 m - long subdomain housing the cave-in; two scattering matrices for the empty subdomains and the subdomain with the cave-in are computed. The partial cave-in is modeled by a trapezoidal prism with a 1.1 m - tall half cylinder on top, which is centered at (201.3, 0.925, 0.9) m [Figure 3.6 (a)].

Empty subdomains, the subdomain with cave-in, and the equivalent surfaces are discretized using 141,792; 197,238; and 34,836 RWG basis functions, respectively. The power values on a line connecting (51.0, 0.925, 1.12) m and (400, 0.925, 1.12) m computed by the proposed simulator are compared with those obtained by multi-modal decomposition for the empty tunnel [Figure 3.6 (b)]. The power values before the cave-in computed by both methods are in good agreement, validating the accuracy of the proposed simulator one more time. Due to obstruction of the cave-in, the power value at $x = 203\,\text{m}$ (just after the cave-in) is 30 dB below that observed in the empty tunnel. Standing-wave phenomenon resulting from the reflections from the cave-in and end wall is observed just before $x = 200\,\text{m}$ and $x = 400\,\text{m}$, respectively.

3.3.2 Mine Gallery

The proposed simulator is used to characterize EM wave propagation in a mine gallery formed by twelve 87.1 m - long rectangular tunnels [Figure 3.7 (a)]. Six of these tunnels are extended along x-direction and intersect with the remaining six tunnels extended along y-direction. The gallery is excited by a $z-$directed dipole operated at 915 MHz and positioned at $(11.425, 0.925, 1.12)\,\text{m}$ (in the intersection of tunnel 1 with tunnel 7) [Figure 3.7 (a)]. The gallery is decomposed into 336 identical 2.5 m - long straight subdomains and 36 identical cross-shaped subdomains used to model the intersections of tunnels [Figure 3.7 (a)]. Consequently, two scattering matrices for straight and cross-shaped subdomains are computed. The straight subdomain, cross-shaped subdomain, equivalent surfaces are discretized using 141,792; 199,356; and 34,836 RWG basis functions, respectively. The power values are computed via the

proposed simulator at receiver points on *xy* plane at $z = 1.12$ m [Figure 3.7 (b)] and along six lines residing in *x*-extended tunnels and connecting $(12.425, y, 1.12)$ m to $(87.1, y, 1.12)$ m with $y = 0.925 + (j-1) \times 12.85$, $j = 1, ..., 6$ [Figure 3.7 (c)]. Apparently, the power values on the line-of-sight receiver points (in tunnels 1 and 7) are significantly higher than those on the remaining receiver points [Figure 3.7 (b)]. Small spikes appear at the intersections of tunnels 2-6 with tunnels 8-12 due to constructive interference of guided waves [Figure 3.7 (c)]. Simulation specifications are provided in Table 3-1.

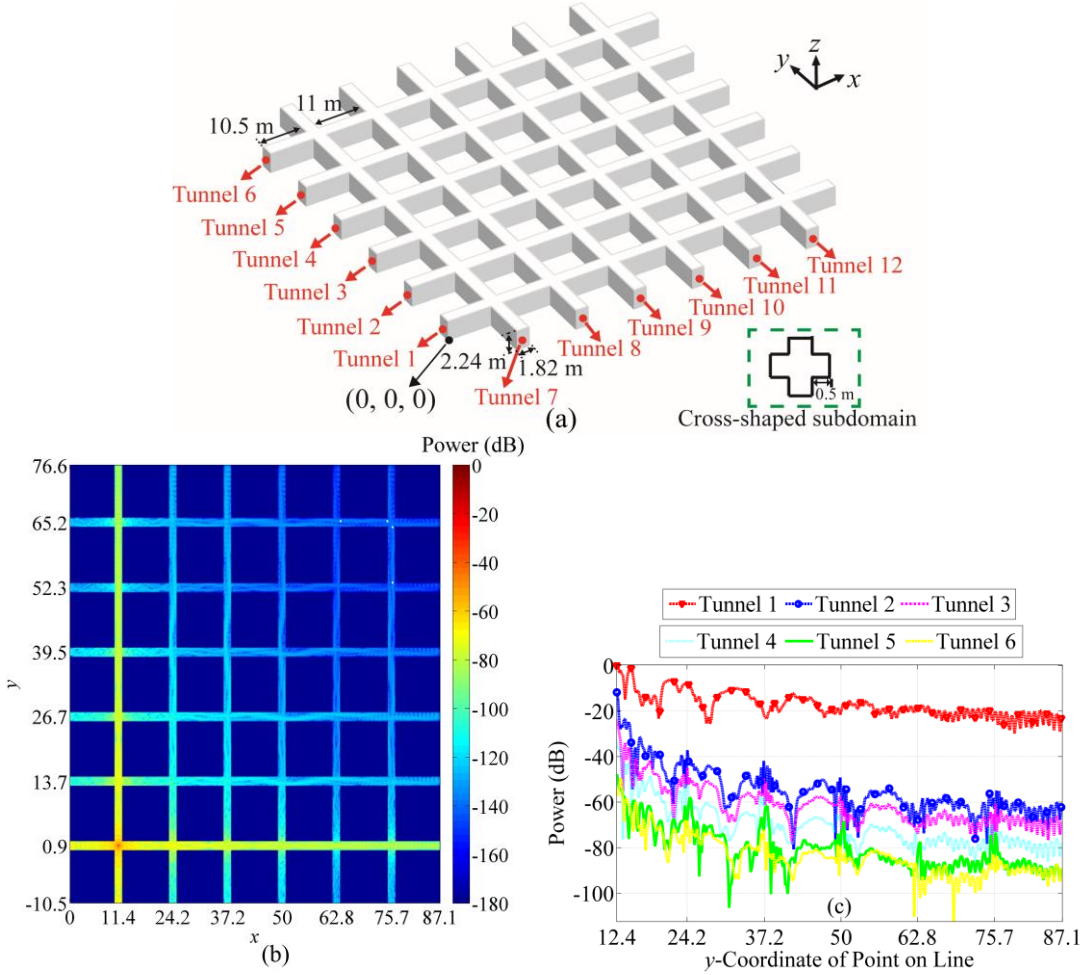

Figure 3.7 (a) The geometry of the mine gallery and the cross-shaped subdomain. Power values computed by the proposed simulator at receiver points located (b) on plane $z = 1.12$ m and (c) on lines aligned in the centers of tunnels 1-6

Numerical Example	Frequency (MHz)	Number of processors	Stage 1: Computing scattering matrices (offline stage)		Stage 2: Solving inter-domain system (online stage)	
			Time (hours)	Average memory per processor (GB)	Time (hours)	Average memory per processor (GB)
Empty arched tunnel	455	16	3.24	2.46	1.18	7.81
	915	32	21.62	4.04	12.45	46.96
Rectangular tunnel with rough walls	455	16	17.21	2.32	1.27	2.79
Rectangular tunnel with smooth walls	455	16	2.88	2.25	0.72	5.02
Rectangular tunnel with cave-in	915	32	38.14	4.64	8.93	25.43
Mine gallery	915	32	62.65	5.05	18.47	13.88

Table 3-1 Specifications of the Simulations Performed by the Proposed Simulator for Numerical Examples in Sections 3.3.1 and 3.3.2

3.3.3 Stochastic Characterization

Next, the proposed simulator is used to statistically characterize EM wave propagation in a 390 m - long rectangular mine tunnel at 455 MHz [Figure 3.8 (a)]. The tunnel is decomposed into 130 identical 3 m - long subdomains. The subdomains and equivalent surfaces are discretized using 45,648 and 10,952 RWG basis functions, respectively. The tunnel is excited by a $z-$directed dipole positioned in the first subdomain at (d_x, d_y, d_z), where d_x, d_y, and d_z are random variables uniformly

distributed in the ranges [1.0, 2.0] m, [0.8, 1.05] m, and [1.0, 1.24] m, respectively. The power values on a line connecting (51, 0.925, 1.12) m and (120, 0.925, 1.12) m are computed by the proposed simulator at 40 random points selected by traditional Monte Carlo method [69]. The power values obtained at random realizations as well as mean and standard deviation of the power along the tunnel are presented in Figure 3.8 (b)-(c). The efficiency of the proposed simulator for stochastic characterization (or uncertainty quantification) studies can be demonstrated by comparing the computational time required by the proposed simulator with that required by an FMM-FFT-SIE simulator, which uses the whole physical domain of tunnel for the analysis [54]. While the FMM-FFT-SIE simulator requires 0.3 hours for computing near-field matrices and far-field patterns (offline stage) and 76 hours for iteratively solving 40 random realizations (online stage), the proposed simulator requires 2.88 hours for obtaining the scattering matrices (offline stage) and 6.3 hours for solving the inter-domain system for 40 random realizations (online stage). (Note: After obtaining scattering matrices, only the RHS of the inter-domain system is changed and solution of inter-domain system is obtained for each random realization.) Therefore, the proposed simulator is more than eight and twelve times faster than the FMM-FFT-SIE simulator overall and at online stages, respectively, demonstrating the efficiency of the proposed simulator in the applications requiring repetitive execution of EM simulator with different excitations. It's important to note that the proposed simulator requires 5.52 GB memory on each processor, which is around 3.6 times less than that required by FMM-FFT-SIE simulator, 20.25 GB; all simulations are executed on 16 processors.

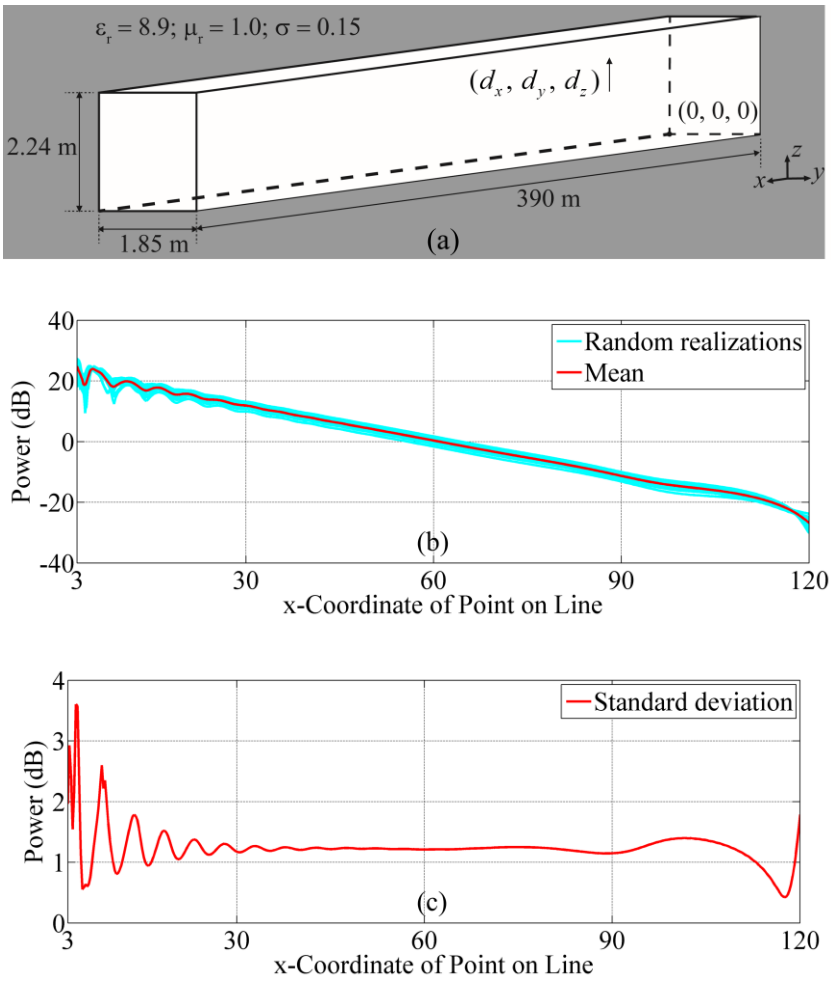

Figure 3.8 (a) The geometry of the rectangular mine tunnel. (b) Mean and (c) standard deviation of the power on receiver points.

3.3.4 Performance Comparison

Here, first, the theoretical estimates of the computational cost and memory requirement of the proposed simulator (provided in Section II.E) are numerically validated. Then, the efficiency of the proposed simulator is demonstrated by comparing its computational cost and memory requirement with those of the FMM-FFT-SIE simulator. To this end, an empty rectangular tunnel with cross section 1.85×2.24 m (width and height) and variable length is considered. The tunnel is excited by a

$z-$directed dipole positioned at (1.5, 0.925, 1.12) m and operated at 455 MHz and 915 MHz. For the analysis at 455 MHz and 915 MHz, the tunnel length is varied from 100 m to 900 m and from 200 m to 660 m, respectively, before the tunnel is decomposed into 3 m - long and 2.5 m - long empty subdomains, as exactly done in Sections 3.3.1.2 and 3.3.1.3, respectively. The simulations for the lower and higher frequencies are performed using 16 and 32 processors, respectively.

3.3.4.1 Complexities of Solving Inter-Domain System

The computational cost and memory requirement of computing scattering matrices scale with those of FMM-FFT and butterfly schemes, which are well-studied in the literature [28, 53] and thereby not analyzed here. On the other hand, the computational cost and memory requirement of solving inter-domain system scale differently with increasing tunnel size when subdomain combining scheme is used and not used, as described in Section II.E and numerically validated in Figure 3.9 (a)-(d). For the analyses at both frequencies, computational costs of solving inter-domain system with and without subdomain combining scheme scale logarithmically and linearly with increasing tunnel length, respectively, [Figure 3.9 (a)-(b)]. The memory requirements of solutions with and without subdomain combining scheme scale logarithmically and remain constant with increasing tunnel size, respectively [Figure 3.9 (c)-(d)]. Needless to say, the proposed subdomain combining scheme allows expedient solution of inter-domain system in exchange of increasing memory requirement.

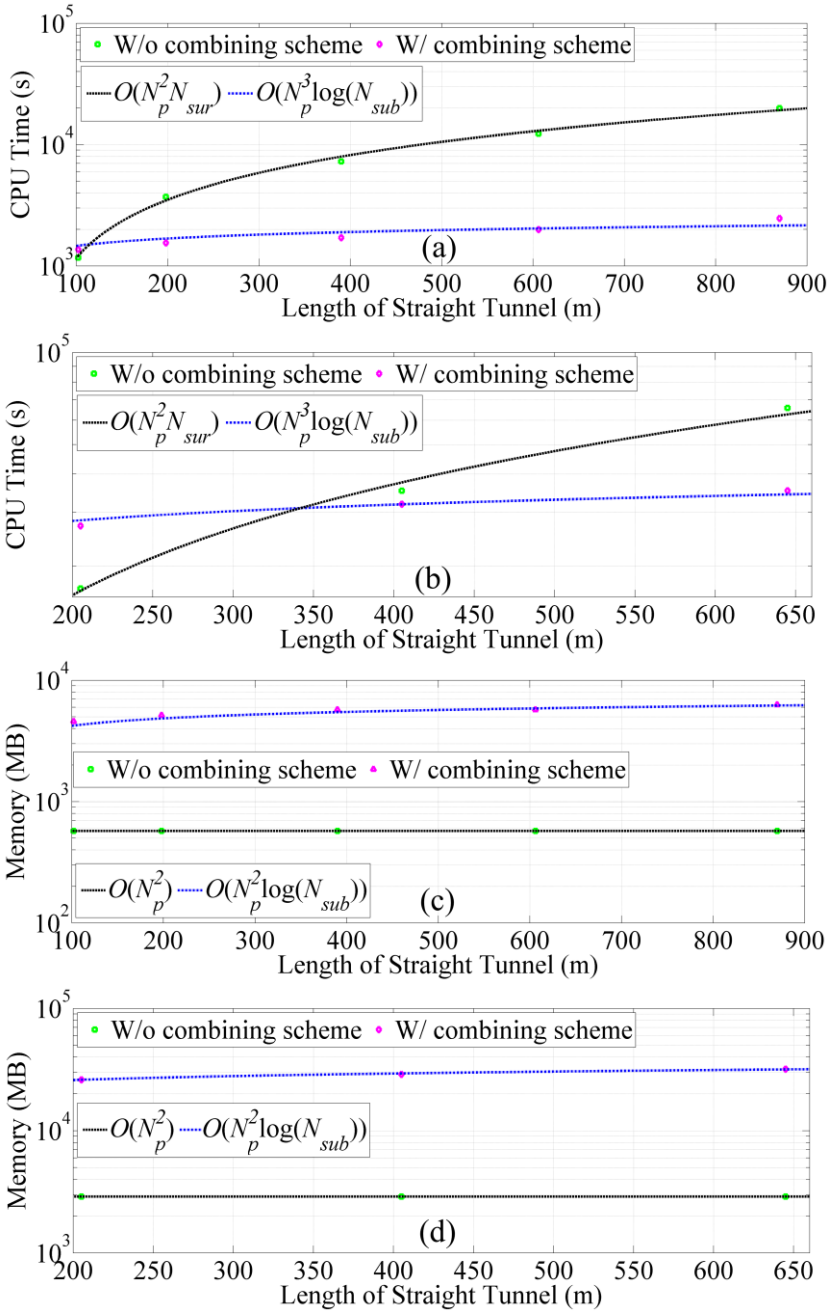

Figure 3.9 Computational time and memory requirement of solving inter-domain system with and without subdomain combining scheme: Computational time for the analysis at (a) 455 MHz and (b) 915 MHz and memory requirement for the analysis at (c) 455 MHz and (d) 915 MHz.

3.3.4.2 Comparison of DD Based SIE Simulator and FMM-FFT Accelerated SIE Simulator

The computational cost and memory requirement of both simulators with increasing tunnel size are investigated for both frequencies [Figure 3.10 (a)-(d)]. In Figure 3.10 (a)-(b), computational cost of the FMM-FFT-SIE simulator and the proposed simulator with and without subdomain combining scheme increase quasi-linearly, linearly, and logarithmically with increasing tunnel size, respectively. The proposed scheme with and without subdomain combining scheme outperforms the FMM-FFT-SIE simulator when the tunnel size is larger than 400 m and 650 m at 455 MHz, respectively, and 500 m and 560 m at 915 MHz, respectively. Note that the computational speed-up achieved by the proposed simulator increases with increasing tunnel size. For all tunnels considered here, the memory requirement of the proposed simulator without subdomain combining scheme, which is constant with increasing tunnel length, is much less than (at least one order of magnitude) that of the FMM-FFT-SIE simulator, which scale quasi-linearly with increasing tunnel length [Figure 3.10 (c)-(d)]. The memory requirement of the proposed simulator with subdomain combining scheme, which scale logarithmically with increasing tunnel length, is less than that of the FMM-FFT-SIE simulator for the analysis of all tunnels at 455 MHz and for the analysis of tunnels larger than 300 m at 915 MHz. Note that the memory saving achieved by the proposed simulator compared to memory requirement of FMM-FFT-SIE simulator increases with increasing tunnel length.

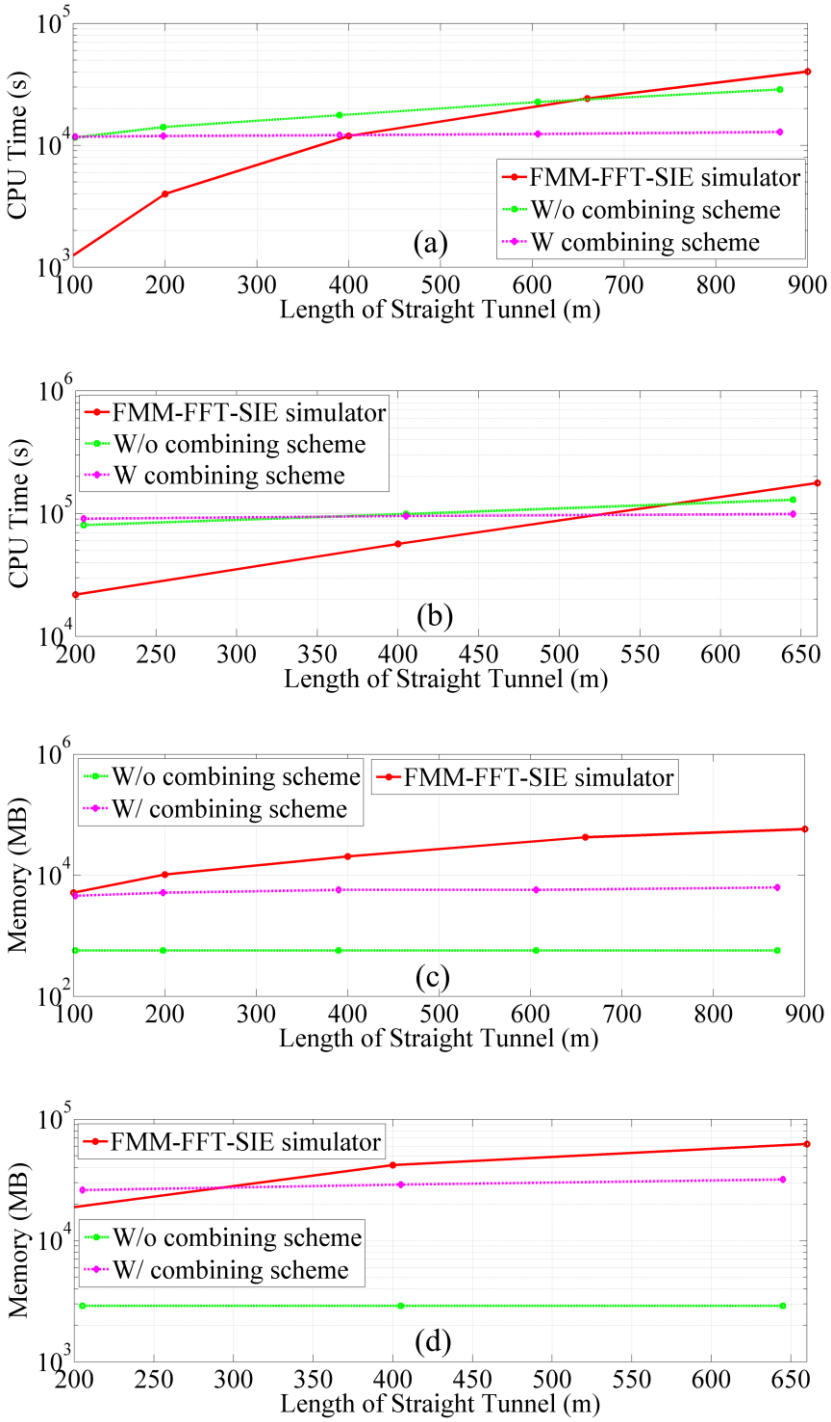

Figure 3.10 Comparison of FMM-FFT-SIE simulator and the proposed simulator with and without subdomain combining scheme: CPU time at (a) 455 MHz and (b) 915 MHz. Memory requirements at (c) 455 MHz and (d) 915 MHz.

3.4 Chapter Conclusion

A DD based SIE full wave simulator was presented for characterizing EM wave propagation in electrically large mine environments. The proposed simulator alleviates the computational burden of full-wave EM analysis for such environments by first dividing the physical domain of mine tunnel/gallery into subdomains. Then, it characterizes EM wave propagation in each subdomain separately using scattering matrices, which are obtained by butterfly-based direct solver and an FMM-FFT scheme. Finally, it obtains an inter-domain system by assembling scattering matrices and solves the system using a fast subdomain combining scheme. The proposed simulator is faster and memory efficient compared to conventional fast SIE simulators; while its computational and memory costs scale logarithmically with tunnel length, those of conventional fast SIE simulators scale quasi-linearly. The numerical results clearly showed the applicability, accuracy, and efficiency of the proposed DD based SIE simulator. Currently, the proposed simulator is extensively being used as a research tool to characterize wireless channels and predict radio coverage in mine tunnels/galleries. Wireless system designers and operators can greatly benefit from the proposed simulator while optimally deploying or re-configuring the nodes of wireless sensing, communication, or tracking systems in mine environments during routine operations or an emergency when the mine is partially obstructed by debris from a cave-in.

CHAPTER 4
Optimization and Reconfiguration of Wireless Communication Systems in Mine Environments

4.1 Chapter Introduction

The design of wireless communication systems in mine environments greatly benefits from tools capable of synthesizing wireless network configurations, and rapidly reconfiguring networks in response to changing operating conditions and catastrophic events. These synthesizing problems in mine environments have been studied in decades and many tools hybridizing electromagnetic (EM) simulator and optimization algorithm have been proposed (see [1] and references therein). Most of the tools leverage approximate techniques, such as multi-mode waveguide models [39], ray-tracing technique [40, 41], and cascaded impedance [8] methods, for EM characterization inside mine environments. However, approximate techniques have drawbacks that limits their utility for accurately analyzing wireless communication systems inside complex mine environments [1, 70]. For example, these methods are usually restricted to certain frequency bands and cannot readily account for the presence of wall roughness, unstructured debris, or mine equipment and workers. In contrast, full wave simulators are

capable of accurately accounting for the presence of miners, mining equipment, as well as roughness on the tunnel walls, but can be hardly used for network optimization problems because full wave simulators oftentimes become prohibitively expensive when repetitive characterizations of electrically large environments are required. On the other hand, the choice of optimization algorithm is important for ensuring the efficiency and robustness of the optimization. Therefore, the design of a wireless network synthesis tool for mine environments requires the careful matching of a complementary EM simulator and optimization algorithm, and endowing the latter with an objective function that provides good performance measure of network configurations.

In this chapter, an efficient optimization framework that addresses the above-mentioned challenges is proposed. The framework combines a DIRECT (Dividing RECTangles) global optimization algorithm [20-22] and the DD based SIE simulator that provides path loss estimates in realistically modeled mine environments. As detailed in previous chapter, the DD based SIE simulator divides the mine tunnels or galleries into subdomains and computes wave input-output relationships for each of them. It next characterizes the global system comprising wave propagation information of all subdomains by enforcing field continuity across subdomain boundaries. When repetitive execution with different excitations is required by the optimization engine, the simulator only re-solves the inter-domain system during each execution and hence is very efficient for optimization purposes. The DIRECT algorithm was purposed by Jones et al. in 1993 [22] as an effective approach to solve global optimization problems with simple constraints. DIRECT algorithm is a kind of Lipschitzian optimization method but does not require the knowledge of the Lipschitz constant. It is comprised of a series of moves

that explore the behavior of the objective function at a set of points in the carefully picked sub-regions of the whole searching space. The high computational complexity underlying in the Lipschitzian optimization methods for high dimensional problems is reduced by this center-point sampling strategy. The objective functions endowed to the optimization framework are adopted from the work by Sherali et al. [71], which proposed a minisum and a minimax objective function, comprising the average and maximum of the weighted path loss measured at receivers, respectively. A penalty term applies to the objective function if the maximum tolerated path loss is violated at certain receivers. A convex combination of the two objective functions is used if an overall measure of performance is needed. The proposed framework is applied to the optimum placement of nodes in partial mesh wireless networks operated at 455 MHz and 915 MHZ inside electrically large mine tunnels and galleries. The signal coverage throughout the mine gallery before and after the optimization are demonstrated in the numerical results.

4.2 Problem Formulation

The optimization framework is designed to improve (ideally, optimize) the desired properties of a wireless network in mine environments via adjusting a set of parameters that influence the performance of the network. Signal coverage might be the most important property of a wireless network in mine environments, but other properties, such as the cost of equipment and maintenance, are also considered in practice and literature [72, 73]. On the other hand, parameters that one can adjust in a network optimization problem typically include the positions of transmitters and receivers, the

topology of the wireless network, and so on [74, 75]. To demonstrate the efficiency and applicability of the proposed optimization framework, the problem considered in this chapter is to optimize the positions of transmitters, given a set of fixed receivers, to obtain the desired qualities of network coverage. The proposed framework may also be applicable to other considerations of wireless network optimization problems.

In general, it is not necessary to pursue the exact global optimal positions of transmitters for this wireless network optimization problem [72]. One reason is that there is no point to distinguish very small difference of the desired coverage property, since the EM simulator is eventually an approximate tool (although it is an accurate approximate). Meanwhile, there are oftentimes multiple sets of transmitter positions that produce almost the same optimal coverage inside a mine environment, especially when they are close to the optimum. For example, if a transmitter reaches an optimal position that achieves line-of-sight connections with some receivers, there will be no significant difference in the coverage quality when the transmitter moves 10 cm away from the optimal position, as long as the line-of-sight connections are maintained. Hence, the aim of the optimization is to find a good approximation that lies within a certain range of the optimal positions.

4.3 Optimization Algorithm

The DIRECT optimization algorithm is a modification of standard Lipschitzian optimization approaches and is widely-used in engineering applications. Examples of its application include optimization of indoor antenna placement [75], design of energy system [76], design of civil transportation system [77]. Other applications of the DIRECT

algorithm are referred to [21] and references therein. Lipschitzian optimization approaches are designed to find the globally minimum (or maximum) of a real-valued objective function with bound constraints, which is considered

$$f^* = f(\mathbf{x}^*) = \min_{\mathbf{x} \in D} f(\mathbf{x}), \tag{4.1}$$

$$\left| f(\mathbf{x}_1) - f(\mathbf{x}_2) \right| \le L \left\| \mathbf{x}_1 - \mathbf{x}_2 \right\|, \ \forall \mathbf{x}_1, \mathbf{x}_2 \in D, \tag{4.2}$$

where $D = [\mathbf{l}, \mathbf{u}] = \left\{ x \in \mathbb{R}^n : l_k \le x_k \le u_k, k = 1, ..., n \right\}$ and L is the Lipschitz constant. The DIRECT algorithm is designed to overcome several shortcomings of standard Lipschitzian optimization approaches, such as the Shubert's algorithm [78]. Hence, this section begins with a review of one dimensional Shubert's algorithm and a discussion on its shortcomings. It next modifies the Shubert's algorithm to the DIRECT algorithm and extends it to higher dimensions.

4.3.1 Shubert's Algorithm

Shubert's algorithm assumes the Lipschitzian is known, which introduces a lower bound on the function in any closed interval whose boundary points are evaluated. Let x be in the region $[a, b]$, $f(x)$ must satisfy

$$f(x) \ge f(a) - L(x - a), \tag{4.3}$$

$$f(x) \ge f(b) + L(x - b). \tag{4.4}$$

The right-hand sides (RHS) of (4.3) and (4.4) correspond to the two lines with slopes $-L$ and $+L$, which lie below $f(x)$ [Figure 4.1 (a)]. The lower bound of $f(x)$ is then

computed at the point of intersection for the two lines. The point of intersection and the lower bound of region $[a,b]$ are defined by $I(a,b)$ and $B(a,b)$ as

$$I(a,b) = (a+b)/2 + \left[f(a) + f(b) \right] / (2L), \tag{4.5}$$

$$B(a,b) = \left[f(a) + f(b) \right] / 2 - L(b-a). \tag{4.6}$$

The function evaluated at $x_1 = I(a,b)$ is the first estimate of the minimum of $f(x)$. The algorithm next divides the region to two sub-regions, $\left[a, x_1\right]$ and $\left[x_1, b\right]$, obtains new intersection points $x_2 = I(a, x_1)$ and $x_3 = I(x_1, b)$, and computes $B(a, x_1)$ and $B(x_1, b)$ [Figure 4.1 (b)]. It then continues by dividing the sub-region with lower *B*-value and repeat the above process until a prescribed condition is satisfied (e.g. lower bound of a region is within a prescribed tolerance of current minimum). The final estimate of minimum is the function value computed at intersection point of the region that has lowest *B*-value.

There are several drawbacks with Shubert's algorithm. First, this algorithm is computationally expensive in higher dimensions since it needs to evaluate function values at all vertices of the searching space during an iteration, leading to 2^n function evaluations for a *n*-dimension problem [20]. Second, the Lipschitz constant oftentimes is not available or cannot be reasonably estimated. Furthermore, the objective functions adopted in many engineering applications may not be Lipschitz continuous. Even if one is able to estimate the Lipschitz constant, it is generally quite high (to ensure it can upper-bound the rate of change of the objective function) and leads to slow convergence [22].

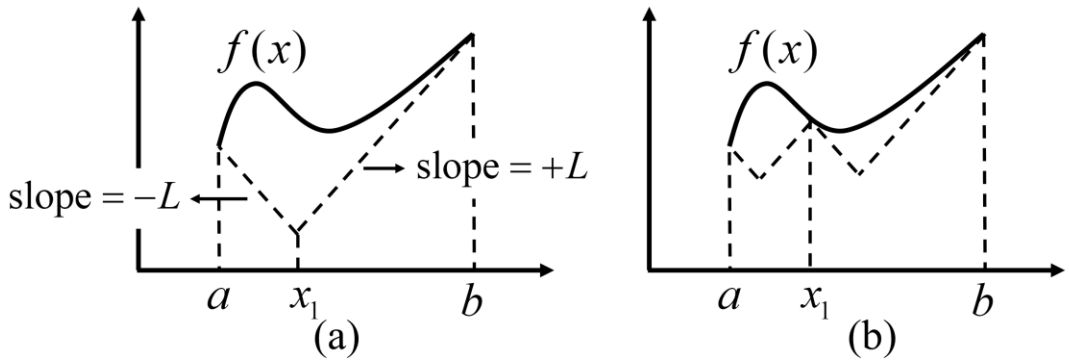

Figure 4.1 (a) Initialize a lower bound for $f(x)$. (b) Dividing regions.

4.3.2 DIRECT Algorithm

To alleviate above problems, DIRECT algorithm was proposed by Jones, et. al in 1993 [22]. It has two major modifications to the standard Lipschitzian optimization. First, instead of sampling the vertices of a searching space, it samples at the midpoints, thereby permitting the algorithm to apply for high dimensions. Second, it does not require the knowledge of Lipschitz constant and the objective function to be Lipschitz continuous. It uses the function value at the center of a region in the searching space and the region's size to determine if it should be divided into sub-regions during an iteration.

4.3.2.1 Initialization

Without losing generality, let the domain of the problem be a unit hyper-cube, i.e.

$$D = \left\{ x \in \mathbb{R}^n : 0 \le x_k \le 1, k = 1, ..., n \right\}. \tag{4.7}$$

The domain of any problem can be easily transformed into a unit hyper-cube. During the initialization phase of the algorithm, it first evaluates the objective function at center of the hyper-cube and points $\mathbf{c}_1 \pm (1/3)\mathbf{e}_k$, $k = 1, ..., n$, and computes

$$v_k = \min\left(f(\mathbf{c}_1 + (1/3)\mathbf{e}_k),\ f(\mathbf{c}_1 - (1/3)\mathbf{e}_k)\right),\ \ k = 1,...,n \tag{4.8}$$

where $\mathbf{c}_1$ is the center of the space and $\mathbf{e}_k$ is the unit vector in the kth dimension. Next, the algorithm divides the hyper-cube. The division begins by dividing the whole region into thirds along the dimension with smallest v_k, and continues by dividing the central sub-region (the one resulted from previous division and containing $\mathbf{c}_1$), along the dimension with the next smallest v_k, until all dimensions are divided. Figure 4.2 illustrates this procedure for an example two-dimension objective function (Note: this objective function is also used as example in later part). To this end, the initialization phase is finished and the algorithm begins its iteration to find and divide the "potentially optimal" regions, which potentially contain the minimum of the objective function.

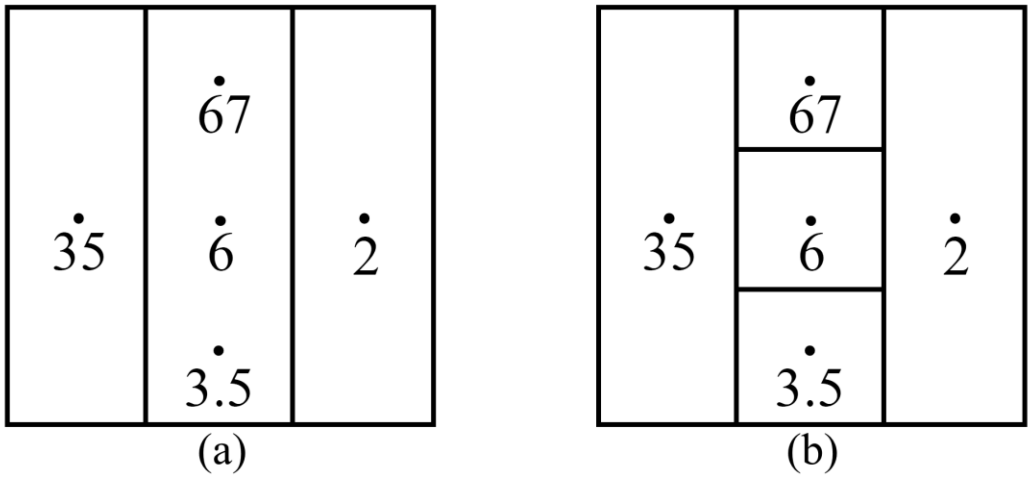

Figure 4.2 (a) Divide the searching domain into three sub-regions along the dimension with smallest v_k. (b) Divide the central sub-region along the dimension with second smallest v_k and finish initialization. Sampling points are represented by black dots and the value of objective function at sampling points are shown below the dots.

4.3.2.2 Iteration

Let $\varepsilon > 0$ be a positive constant and $f_{\min}$ be the current minimum. Denote I be the set of indices of all current regions. A region j is defined to be potentially optimal if there exists some $\tilde{L} > 0$ such that [22]

$$f(\mathbf{c}_j) - \tilde{L}d_j \le f(\mathbf{c}_i) - \tilde{L}d_i, \ \forall i \in I, \ \textit{and} \tag{4.9}$$

$$f(\mathbf{c}_j) - \tilde{L}d_j \le f_{\min} - \varepsilon \left| f_{\min} \right|, \tag{4.10}$$

where $\mathbf{c}_i$ and d_i are the center and a measure of size of region i, respectively. Various definitions of d_i are used in the literature [20, 79]. Here, d_i is defined as the distance from c_i to the vertices of region i. Note that the same definition applies to those with subscript j.The graphical interpretation of the first condition is shown in Figure 4.3 (a). When (4.9) is satisfied, a line with slope $\tilde{L}$ passing $f(\mathbf{c}_j)$ must intercept the vertical axis at $f(\mathbf{c}_j) - \tilde{L}d_j$, which is lower than all the other vertical intercepts of the line with the same slope but passing other points. Hence, the first condition requires the potentially optimal regions to be on the bottom of the convex hull of the points [Figure 4.3 (b)]. The second condition requires that $f(\mathbf{c}_j) - \tilde{L}d_j$ exceeds the current best solution by a nontrivial value, which prevents the algorithm from pursuing extremely small improvements. As demonstrated in [22], the choice of ε between 1×10^{-2} and 1×10^{-7} has only a negligible effect on the performance.

The definition of potentially optimal regions does not provide a practical way to identify if a region j is potentially optimal. Hence, an interpretation of the definition is

given to help the identification [21]. Let $I_1 = \{i \in I : d_i < d_j\}$, $I_2 = \{i \in I : d_i > d_j\}$, and $I_3 = \{i \in I : d_i = d_j\}$. Region j is potentially optimal if

$$f(\mathbf{c}_j) \le f(\mathbf{c}_i),\ \forall i \in I_3, \tag{4.11}$$

$$\max_{i \in I_1} \frac{f(\mathbf{c}_j) - f(\mathbf{c}_i)}{d_j - d_i} \le \min_{i \in I_2} \frac{f(\mathbf{c}_i) - f(\mathbf{c}_j)}{d_i - d_j}, \tag{4.12}$$

and

$$\varepsilon \le \frac{f_{\min} - f(\mathbf{c}_j)}{|f_{\min}|} + \frac{d_j}{|f_{\min}|} \min_{i \in I_2} \frac{f(\mathbf{c}_i) - f(\mathbf{c}_j)}{d_i - d_j},\ \ f_{\min} \neq 0, \tag{4.13}$$

or

$$f(\mathbf{c}_j) \le d_j \min_{i \in I_2} \frac{f(\mathbf{c}_i) - f(\mathbf{c}_j)}{d_i - d_j},\ \ f_{\min} = 0. \tag{4.14}$$

The proof of this interpretation is provided in [21]. Eqs (4.11) - (4.14) can be easily implemented into computer codes.

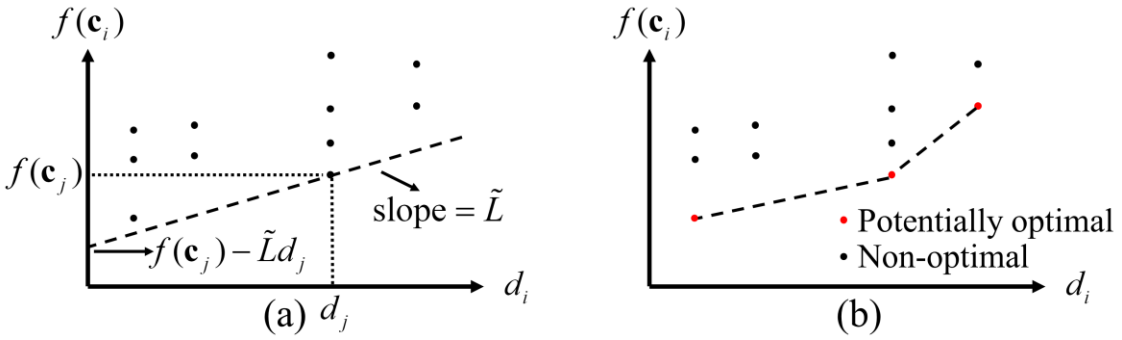

Figure 4.3 (a) First condition of potentially optimal regions. (b) Set of potentially optimal regions. Dot represents the value of objective function evaluated at the center of each region.

After potentially optimal regions are identified, the algorithm proceeds to divide these regions along their longest dimension(s). If a region is a hyper-cube (i.e. all dimensions have the same length), the division is done along all dimensions via the procedures in the initialization phase. The dividing strategy contains the following three steps:

Step 1: Identify the set U_i that contains all dimensions of the maximum side length for the potentially optimal region i.

Step 2: Evaluate the objective function at points $\mathbf{c}_i \pm \delta_i \mathbf{e}_k$ and compute $v_k = \min\{ f(\mathbf{c}_i + \delta_i \mathbf{e}_k), f(\mathbf{c}_i - \delta_i \mathbf{e}_k)\}$ for all $k \in U_i$. Here, $\mathbf{c}_i$ and δ_i are the center and one-third of the maximum side length of the region i, respectively. $\mathbf{e}_k$ is the unit vector in the *k*th dimension.

Step 3: Divide region i into thirds along the dimension with smallest value of v_k, and continue the division for the central sub-region (the one resulted from the previous division and containing $\mathbf{c}_i$) in the dimension with next smallest v_k until it is repeated for all the dimensions in U_i.

As demonstrated in [22], this strategy ensures that the regions to be divided will shrink on all dimensions. Once the division of all potentially optimal regions are done, an iteration of the algorithm is completed. Figure 4.4 illustrates first two iterations for the example two-dimension objective function. Note that the initialization is done in the example given in Figure 4.2.

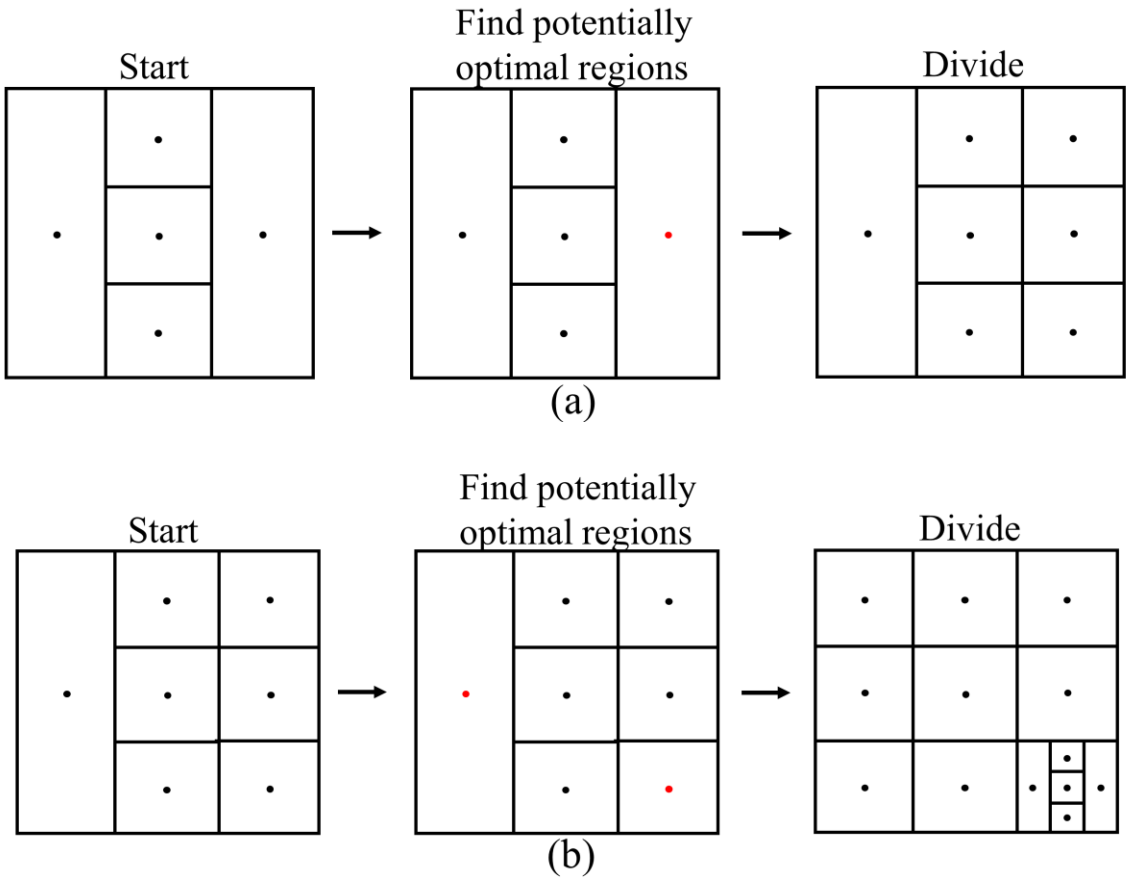

Figure 4.4 First two iterations of the DIRECT algorithm for the example objective function: (a) iteration 1 and (b) iteration 2. Red dots represent the center of potentially optimal regions

4.3.2.3 Termination Criterion, Algorithm, and Discussion

When the global minimum of the objective function is unknown, frequent choices of the termination criterion include the number of iteration or objective function evaluation, size of the smallest regions, and the convergence rate of objective function [80]. Since the aim of the optimization is to find an approximation that lies within a certain range of the optimal positions, the size of smallest regions is chosen as the

termination criterion, i.e., the algorithm stops when the size of smallest region reaches a prescribed threshold. To this end, the DIRECT algorithm is given below.

DIRECT Algorithm

1: Normalize the problem domain to a unit hyper-cube.

2: Set $i = 0$, compute $f(\mathbf{c}_1)$, set $f_{\min} = f(\mathbf{c}_1)$, and divide the hyper-cube

3: **while** size of smallest regions > threshold, **do**

4: Identify all potentially optimal regions

5: Evaluates objective function at points required to divide the potentially optimal regions

6: Divide all potentially optimal regions, update $f_{\min}$, $i = i + 1$.

7: **end while**

Table 4-1 DIRECT Algorithm

The DIRECT algorithm is a direct search method. It does not require any knowledge of objective function gradient. Instead, it evaluates function at sampling points over the searching domain and uses the information obtained from the sampling to decide the searching direction. Hence, it is well-used in engineering applications, where the value of objective function is obtained from numerical simulation and the gradient is unavailable or unreliable. On the other hand, the DIRECT algorithm will converge to global optimum, while many other direct search methods, such as Nelder-Mead algorithm [18] and Hooke-Jeeves pattern search method [19], are only guaranteed to converge to

local optimum. Hence, it can avoid local traps and provide better performance when there are many local optimums in the problem.

The main weakness of the DIRECT algorithm is the slow convergence rate [77]. It can quickly find region(s) containing the optima but will slowly converge to it. That said, this burden is alleviated in the application of wireless network optimizations. As discussed in Section 4.2, the exact optimal positions of transmitters are not necessarily needed, but good approximations close to the optimal positions are enough. Since the DIRECT algorithm can quickly locate regions containing the optimum, the points it samples will likely to be close to the optimum and a good set of approximations can be quickly obtained.

4.4 Objective Function

The quality of an optimization depends on the measure of the desired properties, which is represented by the objective function. The idea of objective functions considered here is to locate the transmitters such that the allocation provides the optimal average coverage or the optimal worst coverage, or a convex combination of them. Based on this idea, the objective functions are mathematically defined as [71]

$$f_1 = \frac{1}{m}\sum_{i=1}^{m} w_i \left[p_i + u_i \max\{0, p_i - s_i\} \right], \tag{4.15}$$

$$f_2 = \max_{i=1,\ldots,m} \left\{ w_i \left[p_i + u_i \max\{0, p_i - s_i\} \right] \right\}, \tag{4.16}$$

where f_1 is a minisum function and f_2 is a minimax function. *m* and *n* are the total number of receivers/access points and transmitters, respectively. The path loss function is $p_i = \min_{j=1,\ldots,n} \{g_{i,j}\}$, where $g_{i,j}$ is the path loss at the *i*th receiver due to the *j*th node. w_i, u_i and s_i are the weight, penalty factor, and maximum tolerated path loss prescribed for the *i*th receiver, respectively. The minisum function is the weighted average of all path losses at the different receiver positions, and a penalty term is added if a maximum path loss threshold is violated. The minimax function is the weighted path loss experienced by the worst served receiver. The choice of f_1 or f_2 depends on the specific optimization scenario and requirements. When an overall measure of coverage quality is required, a convex combination of f_1 and f_2 is used, which is defined as

$$f_c = \varphi f_1 + (1-\varphi) f_2 \tag{4.17}$$

where φ is the combination parameter. The convex combination parameter can be adjusted based on the path loss profiles obtained during optimization.

4.5 Numerical Results

This section demonstrates the efficiency and applicability of the proposed optimization framework via its application to transmitter placement problems in electrically large mine galleries. In all examples below, mine tunnels has air inside and are surrounded by ore with relative permittivity $\varepsilon_r = 8.9$, relative permeability $\mu_r = 1$, and conductivity $\sigma = 0.15$ S/m, where ε_r, μ_r, σ are related to ε_1 and μ_1 via $\mu_1 = \mu_r \mu_0$ and

$\varepsilon_1 = \varepsilon_0 \varepsilon_r - j\sigma/\omega$. The smallest region size threshold for terminating the optimization algorithm is set as 0.05 m. The combination parameter φ for f_c is 0.5 for all examples. The transmitters are modeled by infinitesimal electric dipole with unit moment. The power values obtained by the proposed simulator and other methods are normalized to their maxima and converted to power values which are expressed in logarithmic units. The optimization algorithm was serially implemented in MATLAB [81] and incorporated with the DD based SIE simulator that was parallelly executed on a cluster of dual hexacore X5650 Intel processors located at the Center for Advanced Computing, University of Michigan, Ann Arbor, MI, USA.

4.5.1 Two Connected Tunnels

The proposed framework is used to optimize 915 MHz wireless networks inside a mine gallery formed by two 71.05 m - long tunnels, which extend along x and connect each other via three 11 m - long branches extending along y [Figure 4.5 (a)]. It is first used to optimize a two-transmitter network with respect to average and worst coverage, measured by f_1 and f_2, respectively. Next, the proposed framework is used to optimize a three-transmitter network and reconfigure the optimized network after a catastrophic event, both respect to the overall coverage measured by f_c. Six access points are placed inside the mine gallery [Figure 4.5 (b)]. Three of which are placed 2 meters before the end of tunnel. The remaining three access points are placed at the center of each branch that connects two tunnels. Average CPU time of one distinct simulation for this mine gallery is approximately 3 hours.

4.5.1.1 Two-Transmitter Network

The positions of transmitter 1 and 2 are $(x_1, 0.925, 1.12)$ m and $(x_2, 13.775, 1.12)$ m, respectively, where $x_1 \in [20, 70]$ and $x_2 \in [30, 80]$ are variables to be determined [Figure 4.5 (b)]. Since the two-transmitter network cannot achieve LOS connections with all access points, the optimization results are different for two objective functions. When the framework is used to optimize the average coverage, it converged to $x_1 = 41.32$ and $x_2 = 55.00$ after 83 objective function evaluations and reduced the value of objective function from 50.43 to 26.10. On the other hand, when the framework is used to optimize the worst coverage, it took 115 objective function evaluations to converge to $x_1 = 41.44$ and $x_2 = 60.65$ and reduced the value of objective function from 60.43 to 49.12. The power values are computed on the $xy-$plane at $z = 1.12$ m [Figure 4.5 (c)(d)]. While the framework sought to reasonably achieve LOS connections with as many access points as possible for an optimal average coverage, it had to lose a LOS connection to improve the worst coverage.

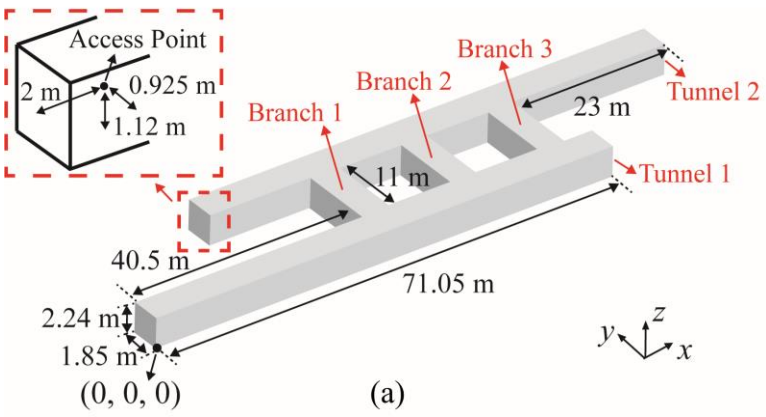

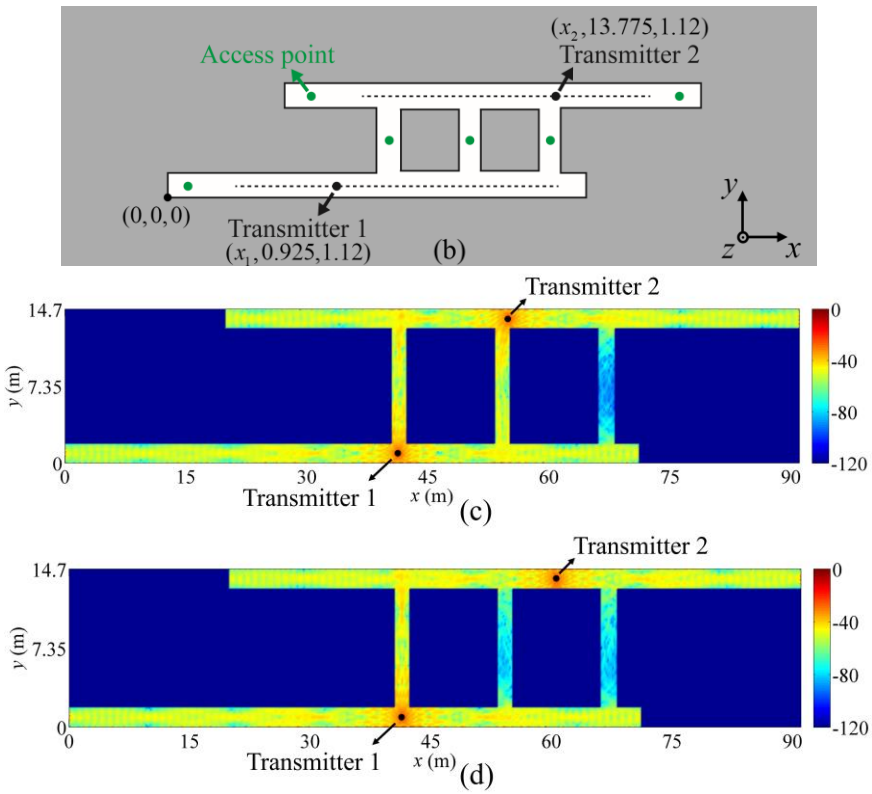

Figure 4.5 (a) Geometry of the two connected tunnels. (b) Two-transmitter network and access points on plane $z = 1.12$ m. Power values computed on plane $z = 1.12$ m for optimization of (c) average coverage and (d) worst coverage (scale: dB).

4.5.1.2 Three-Transmitter Network

The positions of transmitter 1, 2, and 3 are $(x_1, 0.925, 1.12)$, $(x_2, 13.775, 1.12)$, and $(x_3, 0.925, 1.12)$, respectively, where $x_1 \in [20, 50]$, $x_2 \in [30, 80]$, and $x_3 \in [51, 71]$ are to be determined with respect to the overall coverage measured by f_c [Figure 4.6 (a)]. The results are $x_1 = 41.33$, $x_2 = 54.20$, and $x_3 = 67.83$. The optimization is terminated after 157 objective function evaluations and reduces the value of objective function by from 54.08 to 21.15. The power values are computed on the $xy-$plane at $z = 1.12$ m [Figure 4.6 (b)]. It can be observed that all access points have LOS connection with transmitters.

Next, the proposed framework is used to reconfigure the optimized three-transmitter network after a catastrophic event. A cave-in appeared in branch 2 and blocked the signal from transmitting [Figure 4.6 (c)]. Hence, the access point in branch 2 lost LOS connection with transmitters and the value of objective function is increased to 39.07. To perform the reconfiguration, the positions of transmitter 1, 2, and 3 are reset as $(x_1, 0.925, 1.12)$, $(x_2, 13.775, 1.12)$, and $(x_3, 0.925, 1.12)$, respectively, where $x_1 \in [20, 50]$, $x_2 \in [30, 80]$, and $x_3 \in [51, 71]$ are variables to be reconfigured [Figure 4.6 (c)]. The reconfiguration process took 151 objective function evaluations to converge and reduce the value of objective function from 39.07 to 22.13. The reconfigured positions of transmitter 1, 2, and 3 are (41.42, 0.925, 1.12), (66.91, 13.775, 1.12), and (54.64, 0.925, 1.12), respectively. The power values of the reconfigured network are computed on the $xy-$ plane at $z = 1.12$ m [Figure 4.6 (d)]. Apparently, the LOS connection between access point in branch 2 and transmitters is resumed.

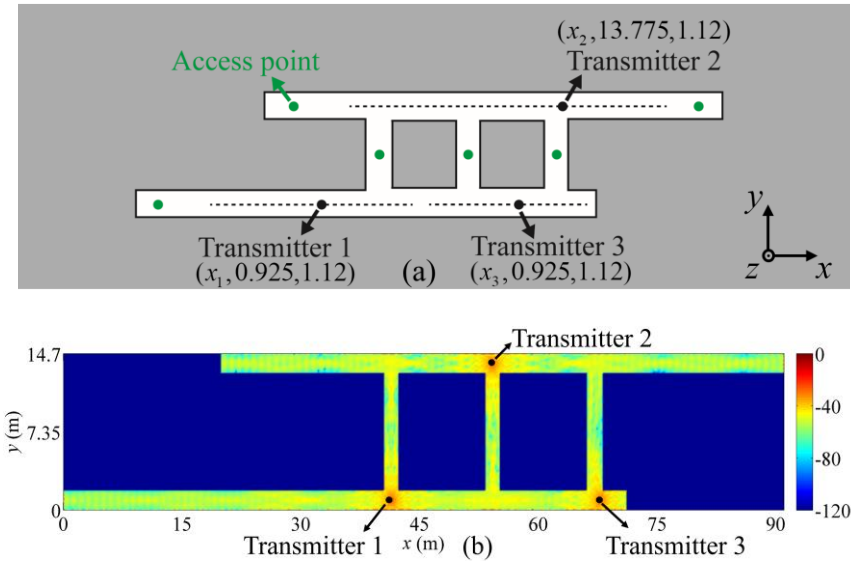

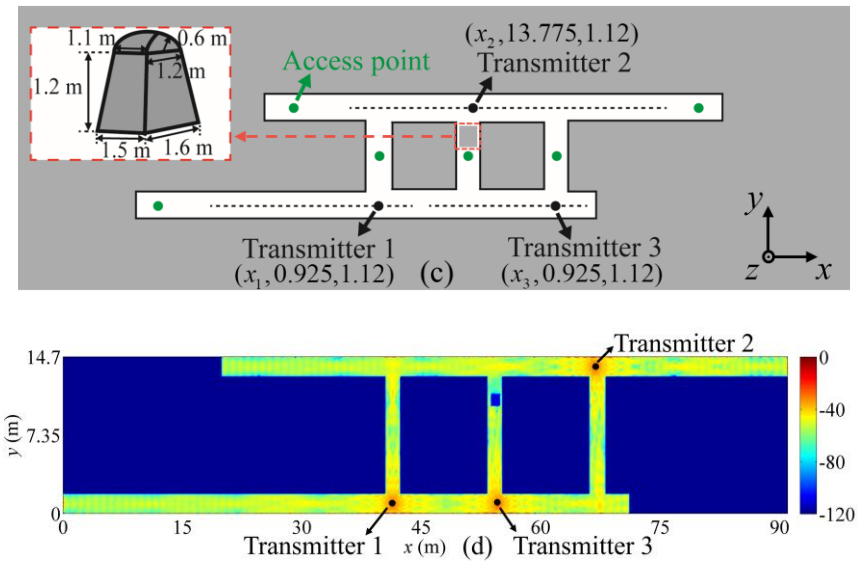

Figure 4.6 (a) Three-transmitter network and access points on plane $z = 1.12$ m. (b) Power values computed on plane $z = 1.12$ m for optimization of overall coverage (scale: dB). (c) Optimized network and the cave-in. (d) Power values computed on plane $z = 1.12$ m after reconfiguration (scale: dB)

4.5.2 4 by 4 Mine Gallery

The proposed EM framework is used to optimize a four-transmitter network inside a mine gallery formed by eight tunnels. Four of which are extended along x-direction and intersect with the remaining four tunnels extended along y-direction. The specifications of this mine gallery are shown in Figure 4.7 (a). The wireless network includes four transmitters that are operated at 455 MHz and placed inside the tunnels extended along x-direction. The positions of transmitter 1, 2, 3 and 4 are $(x_1, 0.925, 1.12)$ m, $(x_2, 13.775, 1.12)$ m, $(x_3, 26.625, 1.12)$ m, and $(x_4, 39.475, 1.12)$ m, respectively [Figure 4.7 (b)]. The variables x_1, x_2, x_3, and x_4 are to be determined in the ranges [20, 60] m, [30, 60] m, [30, 80] m, and [42, 80] m, respectively, with respect to the overall coverage measured by f_c. Eight access points are placed in the mine gallery [Figure 4.7

(b)]. Seven of which are placed 2 m before the ends of the tunnels and the remaining one is placed at the center of tunnel 7. The optimization is terminated after 221 objective function evaluations and reduces the value of objective function from 53.12 to 27.20. The optimized results are $x_1 = 31.11$, $x_2 = 45.10$, $x_3 = 56.85$, and $x_4 = 70.44$. The power values are computed on the $xy-$plane at $z = 1.12$ m [Figure 4.7 (c)]. Apparently, all access points obtain LOS connection with transmitters. It should be noted that the optimization results avoided many local optima. For example, one can move transmitter 2 to the intersection of tunnel 2 and 7 and transmitter 3 to the intersection of tunnel 3 and 6, while the LOS connections between access points and transmitters are maintained. However, it is not the global best solution as the value of objective function is 29.23 for this placement. Average CPU time of one distinct simulation is approximately 1.2 hours.

Next, the proposed framework is used to reconfigure the optimized the network after a catastrophic event. Two cave-ins appeared in tunnel 6 and 7 and blocked the LOS connection between access points in those tunnels with transmitters. During reconfiguration, the variables x_1, x_2, x_3, and x_4 are reset as and to be determined in the ranges [20, 60] m, [30, 60] m, [30, 80] m, and [42, 80] m, respectively [Figure 4.7 (d)]. The reconfiguration process took 255 objective function evaluations to converge and reduce the value of objective function from 42.87 to 32.21. After reconfiguration, the positions of transmitter 1, 2, 3 and 4 are (43.95, 0.925, 1.12), (32.11, 13.775, 1.12), (57.20, 26.625, 1.12), and (70.38, 39.475, 1.12) respectively. The power values of the reconfigured network are computed on the $xy-$plane at $z = 1.12$ m [Figure 4.7 (e)]. Note that the access point in tunnel 7 did not have a LOS connection with any transmitter.

Hence, the reconfigured network is compared to a manually configured network that provides LOS connection with all access points. The positions of transmitters and power values on $xy-$plane of the manually configured network are shown in Figure 4.7 (f). While all access points have LOS connections, it is observed that the points in tunnel 5 and tunnel 3 are not served very well as they are too far from the transmitters. The value of objective function under this configuration is 40.25, which is a lot higher than the one provided with the reconfigured network (32.21), demonstrating the effectiveness of the optimization framework.

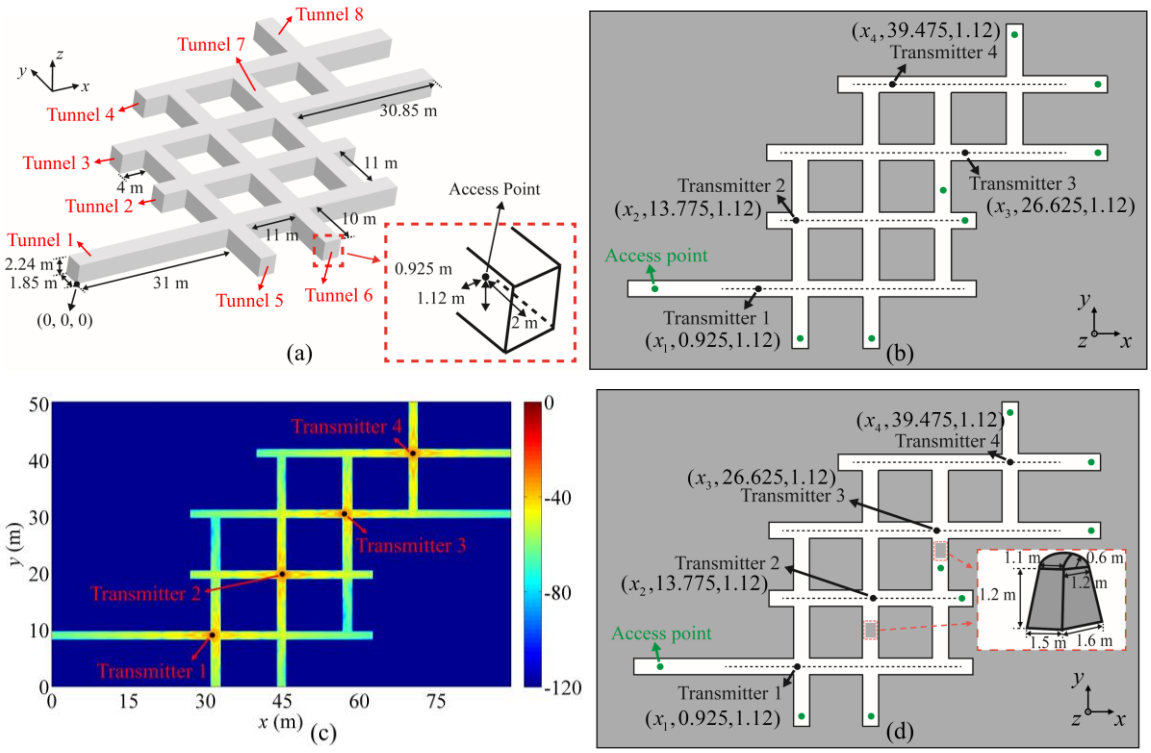

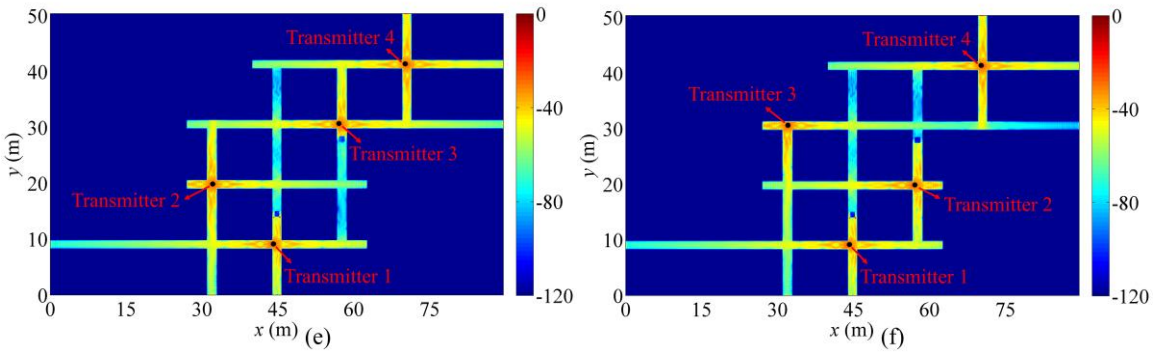

Figure 4.7 (a) Geometry of the 4 by 4 mine gallery. (b) Transmitters and access points on plane $z = 1.12$ m. (c) Power values of the optimized network computed on plane $z = 1.12$ m (scale: dB). (d) Optimized network and the cave-in. (e) Power values computed on plane $z = 1.12$ m after reconfiguration (scale: dB) (f) Power values of the manually configured network computed on plane $z = 1.12$ m (scale: dB)

4.5.3 Mine Gallery with Serrated Tunnel

The proposed EM framework is used to optimize a four-transmitter network inside a mine gallery formed by three tunnels. Two of which are extended along x-direction and intersect with the remaining serrated tunnel. The specifications of this mine gallery are shown in Figure 4.8 (a). The wireless network in the gallery includes four transmitters that are operated at 455 MHz. The positions of transmitter 1, 2, 3 and 4 are $(x_1, 0.925, 1.12)$ m, $(x_2, 0.925, 1.12)$ m, $(x_3, 32.22, 1.12)$ m, and $(x(y_4), y_4, 1.12)$ m, respectively [Figure 4.8 (b)]. The variables x_1, x_2, x_3, and y_4 are to be determined in the ranges [10, 45] m, [75, 100] m, [80, 101] m, and [-13, 30] m, respectively, with respect to the overall coverage. Note that $x(y_4)$ is a function that keeps the position of transmitter 4 in the middle of the cross-section of serrated tunnel 3. Seven access points are placed in the mine galley and positioned at (5, 0.925, 1.12) m, (50, 0.925, 1.12) m, (70, 32.22, 1.12) m, (108.45, -12.78, 1.12) m, (110.0, 16.57, 1.12) m, (76, 32.22, 1.12) m, and (108.45,

45.93, 1.12) m [Figure 4.8 (b)]. The EM framework converged after 231 objective function evaluations. The optimized position of transmitter 1-4 are (24.95, 0.925, 1.12) m, (75.16, 0.925, 1.12) m, (100.16, 32.22, 1.12) m, and (107.6, -11.31, 1.12) m, respectively. The power values computed at z=1.12 plane is shown in Figure 4.8 (c). Average CPU time of one distinct simulation is approximately 0.8 hours. Apparently, all access points are well-served by the network.

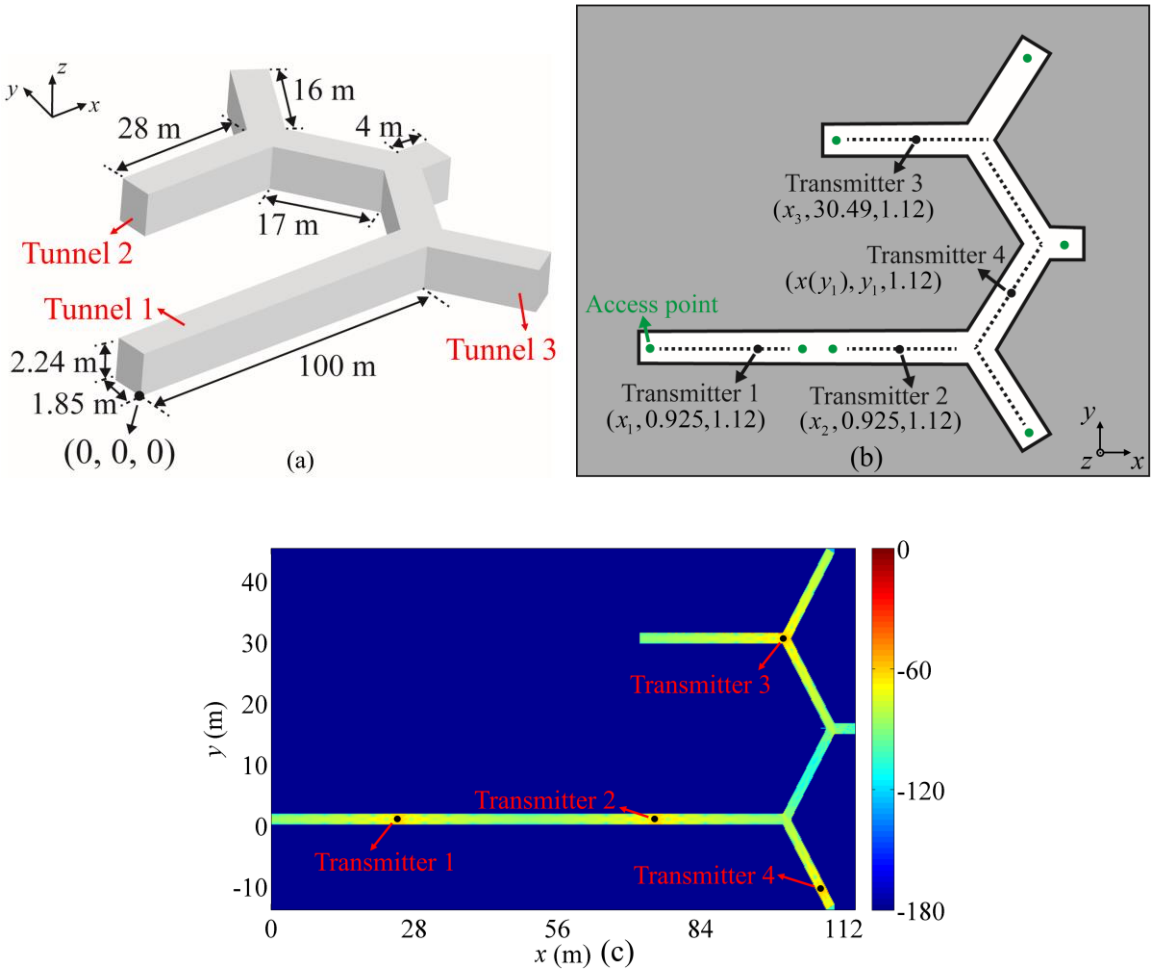

Figure 4.8 (a) Geometry of the mine gallery with serrated tunnel. (b) Transmitters and access points on plane $z = 1.12$ m. (c) Power values of the optimized network computed on plane $z = 1.12$ m (scale: dB).

4.6 Chapter Conclusion

In this chapter, we developed an optimization framework for network (re)configuration in mine environments. It leverages the DIRECT optimization algorithm and the DD based SIE full-wave EM simulator to obtain optimal allocation of the wireless transmitters in mine environments. Simulation results show that the proposed framework is efficient and able to obtain reasonable allocations.

CHAPTER 5
Uncertainty Quantification of Communication Systems in Mine Environments

5.1 Chapter Introduction

In the mine environments, the EM wave propagations are largely affected by the uncertainties in the mine's geometry, loaded equipment, and electronic devices. Examples of these uncertainties (i.e. random variables) include the polarization and position of transmitters and receivers, the moving of miners and mining carts, the roughness of tunnel walls, etc. In practice, these uncertainties can strongly affect the critical information obtained by the computational tools used for analyzing communication systems and even plague the reliability of such tools. Therefore, during an analysis of communication systems in mine environments, the uncertainties should be accurately and efficiently quantified to enhance the credibility of the analysis conducted by computational tools. To do that, a numerically rigorous EM simulator and an efficient uncertainty quantification (UQ) method must be incorporated together. In general, UQ methods can generate the desired statistics for observables (e.g. currents or voltages received by communication devices) using surrogate models constructed via a finite

number of deterministic executions of the EM simulator. Hence, the EM simulator leveraged in a satisfied EM-UQ framework should be able to obtain accurate wave propagation information accounting for all geometrical details and mining equipment inside a mine tunnel or gallery, while the UQ scheme should be able to obtain the statistics efficiently to minimize the cost of execution of the computationally expensive EM simulator.

Quantification of uncertainties in EM analysis is most frequently performed via Monte Carlo (MC) methods. Classical MC methods require the evaluation of observables using EM simulators for many deterministic realizations of the system and its excitation, which are sampled as random variables with known/assumed probability density function (PDF). Although classic MC methods can be simply implemented with EM simulators to provide the statistical moments and PDFs of the observables, they often converge quite slowly and require a large number of deterministic EM simulations to yield reliable statistical data. This slow convergence limits the applicability of classic MC methods to the uncertainty quantifications of EM phenomena in complex and large-scale mine environments, for which each deterministic simulation requires significant CPU resources. To reduce the cost of classic MC methods, the methods use generalized polynomial chaos (gPC) expansions to generate surrogate models of observables have been applied within the EM society. Among these gPC methods, the multi-element probabilistic collocation (ME-PC) method [24] is highly efficient and accurate for surrogate model generation of EM observables that vary rapidly and/or are discontinuous functions of random variables, since it effectively tailors the collocation/integration points used for polynomial approximations to the behavior of observables. That said, its applicability is limited to the

moderate-dimensional random domains as the number of subdomains resulting from adaptive refinement and the number of collocation points in each subdomain become excessively large as the dimension increases. To remedy this issue, an HDMR extension [25] to the ME-PC method is leveraged to permit the accurate and efficient construction of surrogate models for EM observables in high dimensions.

In the chapter, we propose a computational framework that leverages the novel fast full wave EM simulators (described in previous chapters) in concert with modern high dimensional model representation (HDMR) method [25, 82] to produce qualitative insights and actionable quantitative data pertinent to the design, deployment, and post-event reconfiguration of mine communication and tracking systems. The HDMR method reduces the cost of the surrogate model construction by iteratively including only the component functions pertinent to the "most important" random variables. The component functions, which are approximated by the multi-element probabilistic collocation (ME-PC) method [25], can represent either individual or combined contributions of random variables to the observables. The observable values at collocation/integration points chosen by the ME-PC method are computed using the FMM-FFT accelerated EM simulator. The new framework can apply to large mine environments comprised of tunnels, tunnel junctions, and galleries.

This chapter is organized as follows: it first describes the HDMR method that is used as the UQ tools in the framework. Next, four major communication systems installed in mine environments are introduced (leaky feeder system, through-the-earth system, medium frequency radio system, and wireless node-based mesh network). UQ examples for each system are analyzed with our EM-UQ framework.

5.2 HDMR Method

HDMR-generated surrogate models enable the efficient and accurate stochastic characterization of electronic systems subject to uncertainties in mine environments. Once the HDMR method successfully converges and constructs the surrogate model, the MC simulations will be performed on the surrogate model (instead of the EM simulator) and the statistics of desired observables can be efficiently obtained.

5.2.1 Formulation of HDMR

Let $\mathbf{x} = [x^1, x^2, ..., x^{N_{dof}}]$ denote a random vector defined over a domain D. Each element in $\mathbf{x}$ is a random variable that has a known PDF and parameterizes an uncertain quantity in the mine environments. The HDMR expansion approximates an unknown function $V(\mathbf{x})$, which represents an observable in mine communication systems, in terms of component functions as

$$V(\mathbf{x}) = \sum_{\mathbf{u} \subseteq \Omega} V_{\mathbf{u}}(\mathbf{x}^{\mathbf{u}}) \tag{5.1}$$

where $\Omega = \{1, ..., N_{dof}\}$ is the general set of random variable indices, $\mathbf{u}$ is a subset of Ω, i.e. $\mathbf{u} \subseteq \Omega$, and $|\mathbf{u}|$ denotes the cardinality of subset $\mathbf{u}$. $\mathbf{x}^{\mathbf{u}}$ is a $|\mathbf{u}|$-dimensional random vector and $V_{\mathbf{u}}(\mathbf{x}^{\mathbf{u}})$ represents the component functions defined over D. For example, for $\mathbf{u} = \varnothing$, $V_{\mathbf{u}}(\mathbf{x}^{\mathbf{u}}) = V_{\varnothing}(\mathbf{x}^{\varnothing}) = V_0$ is the zeroth-order component function which is constant over D; for $\mathbf{u} = \{1\}$, $V_{\mathbf{u}}(\mathbf{x}^{\mathbf{u}}) = V_1(\mathbf{x}^1)$ is the first-order component function that represents the individual contribution of x^1 to $V(\mathbf{x})$. The HDMR construction can be better

described by an example. Assume that $N_{dof} = 3$ and $\Omega = \{1,2,3\}$, all possible subsets of Ω, $\mathbf{u}$ and all component functions $V_{\mathbf{u}}\left(\mathbf{x}^{\mathbf{u}}\right)$ corresponding to these possible subsets are given in Table 5-1.

Subset, $\mathbf{u}$	$V_{\mathbf{u}}\left(\mathbf{x}^{\mathbf{u}}\right)$	$\lvert\mathbf{u}\rvert$
$\varnothing$	V_0	1
{1}	$V_1\left(x^1\right)$	1
{2}	$V_2\left(x^2\right)$	1
{3}	$V_3\left(x^3\right)$	1
{1,2}	$V_{12}\left(x^1, x^2\right)$	2
{1,3}	$V_{13}\left(x^1, x^3\right)$	2
{2,3}	$V_{23}\left(x^2, x^3\right)$	2
{1,2,3}	$V_{123}\left(x^1, x^2, x^3\right)$	3

Table 5-1 The correspondence between subsets of $\Omega = \{1,2,3\}$ and the component functions used to build HDMR expansion and the cardinalities of subsets.

For this example, one can construct the HDMR expansion in (5.1) using the component functions given in Table 5-1 as

$$\begin{aligned} V\left(\mathbf{x}\right) = V_0 + V_1\left(x^1\right) + V_2\left(x^2\right) + V_3\left(x^3\right) + V_{12}\left(x^1, x^2\right) \\ + V_{13}\left(x^1, x^3\right) + V_{23}\left(x^2, x^3\right) + V_{123}\left(x^1, x^2, x^3\right). \end{aligned} \tag{5.2}$$

The advantage of such construction can be illustrated by selecting an observable that consists of a constant term and monomials such as $V\left(\mathbf{x}\right) = 1 + \left(x^1\right)^2 + \left(x^2\right)^2 + \left(x^3\right)^2$, (Note: the indices (or superscripts) of random variables are written inside parentheses while their powers are intentionally left outside to avoid confusion). The component functions V_0, $V_1\left(x^1\right)$, $V_2\left(x^2\right)$, and $V_3\left(x^3\right)$ are needed to approximate $V\left(\mathbf{x}\right)$ while the remaining

component functions in (5.2) are redundant. In many practical communication systems, like in this example, the behavior of observables can be efficiently approximated by including only the low-order component functions. This fact renders the HDMR expansions highly suitable for surrogate model generation of $V(\mathbf{x})$ that is in high-dimensional random domains but can be approximated by surrogate models constructed in low dimensional domains.

5.2.2 Definition and Selection of Component Functions in HDMR

The component functions are expressed in terms of observable values on cuts passing through a reference point $\bar{\mathbf{x}}$, i.e.

$$V_{\mathbf{u}}\left(\mathbf{x}^{\mathbf{u}}\right) = V\left(\mathbf{x}^{\mathbf{u}}\right)\Big|_{\mathbf{x}=\bar{\mathbf{x}}\setminus\mathbf{x}^{\mathbf{u}}} - \sum_{\mathbf{v}\subset\mathbf{u}} V_{\mathbf{v}}\left(\mathbf{x}^{\mathbf{v}}\right) \tag{5.3}$$

where $\mathbf{x} = \bar{\mathbf{x}} \setminus \mathbf{x}^{\mathbf{u}}$ indicates that the random variables with indices that do not belong to subset $\mathbf{u}$ are set to the corresponding values at reference point $\bar{\mathbf{x}}$. The reference point in this study is select as the mass center of *D*, i.e.,

$$\bar{\mathbf{x}} = \left[\bar{x}^1, ..., \bar{x}^{N_{dof}}\right] = \left[(a^1 + b^1)/2, ..., (a^{N_{dof}} + b^{N_{dof}})/2\right]. \tag{5.4}$$

The choice of reference point is not unique, it may also be selected as the centroid of SG integration rule [83], as a random point at which the observable value is closest to the global mean [84], or as a random point determined due to the prescribed weights of dimensions [85]. For the example given above, the component functions obtained are given as follows:

$$
\begin{aligned}
&V_0 = V\left(\bar{\mathbf{x}}\right)\\
&V_1\left(x^1\right) = V\left(x^1, \bar{x}^2, \bar{x}^3\right) - V_0;\\
&V_2\left(x^2\right) = V\left(\bar{x}^1, x^2, \bar{x}^3\right) - V_0;\\
&V_3\left(x^3\right) = V\left(\bar{x}^1, \bar{x}^2, x^3\right) - V_0;\\
&V_{12}\left(x^1, x^2\right) = V\left(x^1, x^2, \bar{x}^3\right) - V_0 - V_1\left(x^1\right) - V_2\left(x^2\right);\\
&V_{13}\left(x^1, x^3\right) = V\left(x^1, \bar{x}^2, x^3\right) - V_0 - V_1\left(x^1\right) - V_3\left(x^3\right);\\
&V_{23}\left(x^2, x^3\right) = V\left(\bar{x}^1, x^2, x^3\right) - V_0 - V_2\left(x^2\right) - V_3\left(x^3\right);\\
&V_{123}\left(x^1, x^2, x^3\right) = V\left(x^1, x^2, x^3\right) - V_0 - V_1\left(x^1\right) - V_2\left(x^2\right) - V_3\left(x^3\right)\\
&\qquad\qquad - V_{12}\left(x^1, x^2\right) - V_{13}\left(x^1, x^3\right) - V_{23}\left(x^2, x^3\right);
\end{aligned}
\tag{5.5}
$$

To iteratively select the component functions that significantly contribute to observable, the weight associated with the first-order functions are defined as

$$
\varsigma_{\mathbf{u}} = \left| E\left[V_{\mathbf{u}}(\mathbf{x}^{\mathbf{u}})\right] / V_0 \right|;\ |\mathbf{u}| = 1. \tag{5.6}
$$

Here, $E\left[V_{\mathbf{u}}(\mathbf{x}^{\mathbf{u}})\right]$ is the means of first-order component functions. In case V_0 is zero, the weight is set to $E\left[V_{\mathbf{u}}(\mathbf{x}^{\mathbf{u}})\right]$. A component function is assumed to be significant when its associated weight is larger than a prescribed value δ_1. During the iterations with the second-order component functions, only those involving the significant first-order component functions are computed and are added to the second-level HDMR expansion only if their associated weights are larger than the prescribed value. This scheme is then repeated for all levels. Note that the weights of component functions at higher levels are defined as

$$
\varsigma_{\mathbf{u}} = \left| E\left[V_{\mathbf{u}}(\mathbf{x}^{\mathbf{u}})\right] \Big/ \sum\nolimits_{|\mathbf{v}|<|\mathbf{u}|-1} E\left[V_{\mathbf{v}}(\mathbf{x}^{\mathbf{v}})\right] \right|;\ |\mathbf{u}| > 1 \tag{5.7}
$$

An additional stopping criterion is the decay rate of relative difference κ between observable means computed at two consecutive levels, which is defined as

$$\kappa = \left| \sum_{|\mathbf{v}|=|\mathbf{u}|} E\left[V_{\mathbf{v}}(\mathbf{x}^{\mathbf{v}})\right] - \sum_{|\mathbf{v}|<|\mathbf{u}|-1} E\left[V_{\mathbf{v}}(\mathbf{x}^{\mathbf{v}})\right] \right| \Big/ \left| \sum_{|\mathbf{v}|<|\mathbf{u}|-1} E\left[V_{\mathbf{v}}(\mathbf{x}^{\mathbf{v}})\right] \right|. \tag{5.8}$$

If this relative difference is smaller than a prescribed tolerance δ_2, the HDMR is assumed to have converged. To provide additional accuracy for the surrogate model, the component functions identified as insignificant are also included in the final HDMR expansion that construct the surrogate model of $V(\mathbf{x})$.

5.2.3 Integrating HDMR with ME-PC Method

To recursively obtain the component functions, the observable value on reference point $\bar{\mathbf{x}}$ (for $|\mathbf{u}|=0$) is computed and the observable values on lines (for $|\mathbf{u}|=1$), planes (for $|\mathbf{u}|=2$), and hyperplanes (for $|\mathbf{u}|\geq 3$) passing through $\bar{\mathbf{x}}$ are interpolated using the ME-PC method. To do that, the component function $V\left(\mathbf{x}^{\mathbf{v}}\right)$ are approximated using *p*th-order local gPC expansion as

$$V\left(\mathbf{x}^{\mathbf{v}}\right)\Big|_{\mathbf{x}=\bar{\mathbf{x}}\setminus\mathbf{x}^{\mathbf{v}}} = \sum_{m=0}^{N_p} v_m^{v}\, \mathbf{P}_m(\mathbf{x}^{v})\Big|_{\mathbf{x}=\bar{\mathbf{x}}\setminus\mathbf{x}^{\mathbf{v}}} \tag{5.9}$$

where v_m^{v} and $\mathbf{P}_m(\mathbf{x}^{v})$ denotes the local gPC coefficients and |v|-variate local orthogonal Legendre polynomial basis functions (defined over the domain of $V\left(\mathbf{x}^{\mathbf{v}}\right)\Big|_{\mathbf{x}=\bar{\mathbf{x}}\setminus\mathbf{x}^{\mathbf{v}}}$). The local gPC coefficients v_m^{v} are obtained by evaluating a |v|-variate integral. During the ME-PC's construction of expansion coefficients, an adaptive refinement process is performed and

the refinement parameters are also computed separately for all component functions. The final approximation of $V(\mathbf{x})$ is to sum up the ME-PC approximations of all component functions. To this end, the ME-PC enhanced HDMR method is introduced. Further information about this method can be referred to [25, 82].

5.3 Uncertainty Quantification of Communication Systems

The EM-UQ framework leverages the above-described ME-PC enhanced HDMR method to approximate observables (and thereby, their statistics) over the "random domain" of variables that parameterize the uncertainties existing inside mine tunnels or galleries. The deterministic full-wave EM simulators are used by the UQ method to compute observables for various mine configurations represented by selected collocation points in the random domain. Subsequently, the framework constructs compact multivariate polynomial surrogate models that accurately approximate the observables and are computationally cheap to evaluate. Finally, the surrogate models are used in lieu of the computationally expensive EM simulator to extract pertinent statistics via MC simulations performed on the surrogate model.

The following four sections present the application of proposed EM-UQ framework to four commonly-used communication systems in mine environments: leaky feeder systems, TTE systems, medium frequency (MF) systems, and wireless node-based mesh networks. For each system, an UQ examples are presented. In all examples, the threshold δ_1 for determining significant component functions and δ_2 for determining the

convergence of HDMR are set as 10^{-2} and 10^{-16}, respectively. The tolerance of ME-PC refining tolerance (see its definition in [24]) is set as 10^{-1}.

5.3.1 Leaky Feeder System

Reliable communication is essential for underground mines and tunnels for safety and productivity reasons. This communication system is needed to distribute video and audio information within the complex tunnel networks. To achieve this, the leaky feeder system is often used as transmission medium in underground mines and tunnels [Figure 5.1]. The leaky feeder is dual functional; it not only transmits radio signal as a cable but also radiates the signal along its length via carefully designed slots. The leaky feeder system is almost noise free and has enough bandwidth to support multiple radio signals carrying voice and text simultaneously. The leaky feeder system is also able to transfer electricity to power up amplifiers and active wireless nodes.

There are many previous works on the leaky feeder system. Fan et al. [86] studied the radiation characteristics of leaky co-axial cable field and compared it with the characteristics of the helical antenna. Feng et al. [87] theoretically analyze the radiating modes of leaky coaxial cable fields. However, these techniques rely on simplified assumptions and/or approximations that limit their applications. In contrast, full-wave methods does not suffer from these limitations. In [88], Wang et al. used the finite-difference time-domain (FDTD) method to calculate the electric field distribution in the slot cut in the outer conductor of the coaxial cable. They then obtained the radiation fields from the slots via the equivalent magnetic current and the dyadic Green's function. That

said, FDTD is computationally expensive for long tunnels with cables and its focus is to compute the coupling loss of a cable rather than the fields distribution inside the tunnel.

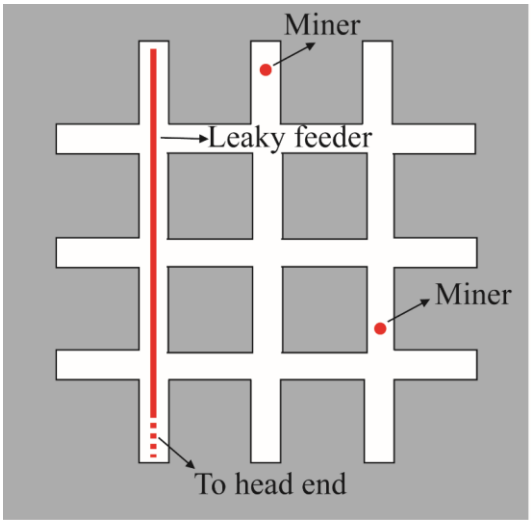

Figure 5.1 An examples of leaky feeder system. The two miners can communicate with each other if they are within the range of the leaky feeder cable.

In this section, our proposed EM-UQ framework is used to analyze leaky feeder systems inside mine tunnels or galleries. In all examples considered here, the cable is operated at radiating mode and the signal strength decay inside the cable is modeled by the diffuse model given in [89]. In the diffuse model, a cable element of length h is represented as a point source radiating the power Ph in appropriate polarization. The radiating power per unit length is

$$P = (\pi D/8)(4\pi/\lambda)^2 10^{-L/10} \exp(-2\alpha x)\, P_{feed}\,. \tag{5.10}$$

Here, D is the reference distance between the axis of a long diffuse radiator and a half-wave dipole that is parallel to the axis. α is the attenuation constant in Np/m. L is the standard coupling loss of a leaky coax. D is usually 20 ft.; α and L can be easily found

in commercial leaky cable manuals. In all examples, α and L are chosen as 0.0152 and 65.0, respectively. x is the distance between the radiating point and the feeding point.

In the real environment, there are many uncertainties affecting the performance of a leaky feeder system. For example, the cable installed on the wall of a tunnel may be affected by mine geometry and may not keep unmoved all along the tunnel. Hence, the actual location of the cable and the amplifier on it may be different than planned. In this example, the uncertainty of the cable's position and an amplifier's position is quantified via the proposed EM-UQ framework. As shown in Figure 5.2, a leaky feeder system installed in a 650-meter long tunnel is analyzed. The width and height of the tunnel is 1.85 meters and 2.24 meters, respectively. The relative permittivity ε_r, permeability μ_r and conductivity σ of the surrounding ore are 8.9, 1.0, and 0.15, respectively. The leaky cable is 640 meters long and extends from $(5, y_l, z_l)$ m to $(645, y_l, z_l)$ m, where y_l and z_l are the random variables uniformly distributed in [0.6, 1.25] m and [1.90, 2.10] m. The amplifier is installed near the center of the leaky cable and positioned at (x_a, y_l, z_l) m, where x_a is a random variable uniformly distributed in [290, 310] m.

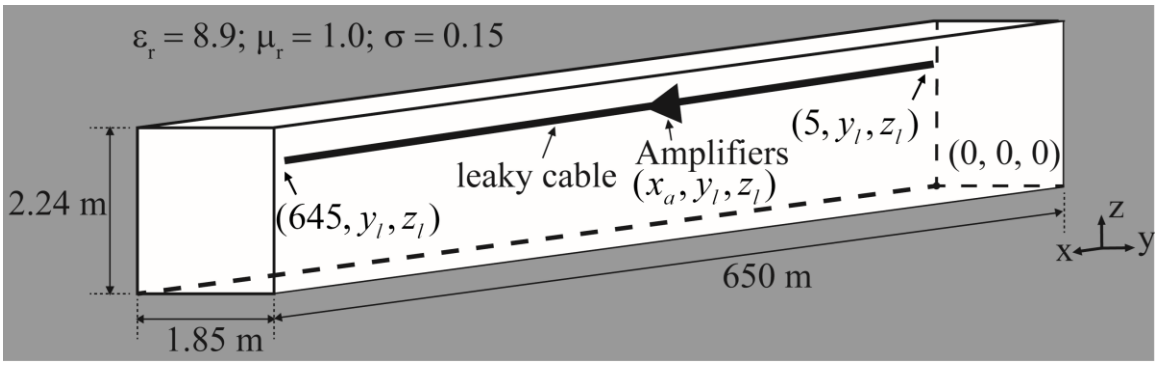

Figure 5.2 Geometry of a straight tunnel and a leaky cable installed with an amplifier

Two receivers are positioned inside the tunnel. Receiver 1 is chosen at (300, 0.925, 1.12) and receiver 2 is at (640, 0.925, 1.12), i.e., one is near the center of the tunnel and the other is near the end. The observables are the received power strength at the two receivers. Table 5-2 presents these observables' averages and standard deviations computed by the proposed EM-UQ framework. It can be observed that the power strength at receiver 1 has much larger standard deviation than that at receiver 2. This is expected as the amplifier is placed around receiver 1. In addition, the PDF of power values received at the two receivers are obtained by performing 5000-point MC simulations on the HDMR constructed surrogate model [Figure 5.3 (a)-(b)].

Statistics	Observables	Proposed Framework
Mean (dB)	Power Strength at Receiver 1	-6.97
	Power Strength at Receiver 2	-30.39
Standard Deviation (dB)	Power Strength at Receiver 1	3.83
	Power Strength at Receiver 2	1.96
Number of Simulations		61

Table 5-2 Statistics and number of deterministic simulations obtained by the proposed EM-UQ framework.

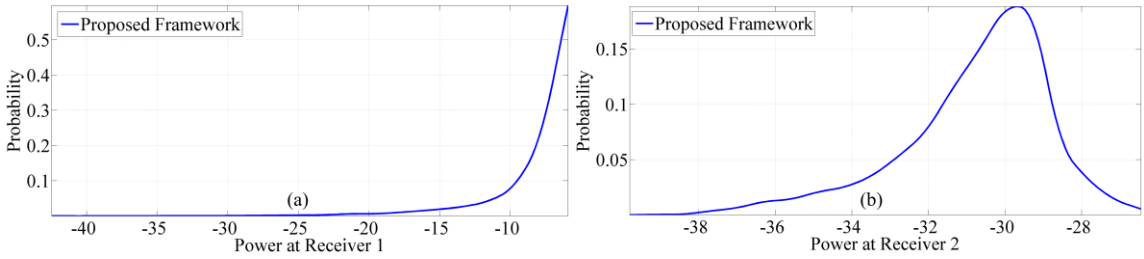

Figure 5.3 PDF of power values received at (a) receiver 1 and (b) receiver 2.

5.3.2 Through-the-Earth System

The Mine Improvement and New Emergency Response Act of 2006 (MINER Act) requires that every underground mine in the U.S. should be equipped with an emergency response plan. The plan must include a two-way wireless post-accident communication system between underground and surface, which is used to electronically track and communicate with underground workers. In an emergency, conventional communication systems may be interrupted or disabled if communication infrastructures are damaged and the backup communication between rescuers at the surface and miners underground becomes particularly important in such situation. One way to establish the post-accident communication is to directly communicate from surface to the underground mines [Figure 5.4 (a)]. Although previous researches showed that the TTE transmission between surface and underground is difficult to establish, recent advances in this technology have led to better communication capability and offer new possibilities for TTE communication. Typically, signals at frequencies below 10 kHz can penetrate the earth and offer promising capabilities to establish through-the-earth (TTE) connections. Hence, current TTE communications tested in mine environments use large loop antennas operating at ultra-low frequency to send/receive signal through the earth. A major advantage of the TTE communications is that it requires much less underground and surface infrastructure than higher frequency mine communication systems in post-accident situation.

In an emergency, the configuration of a TTE communication system may be affected or damaged by the accident. For example, an earthquake or an explosion inside mine tunnels would change the position and orientation of communication devices, which

lead to uncertainties in the system. Oftentimes these uncertainties would have influences on the signal transmission path and the connection quality. To enhance the reliability and functionality of a TTE communication system, these uncertainties must be accurately quantified. In this example, the uncertainties in the transmitter's location and polarization are quantified via the proposed EM-UQ framework.

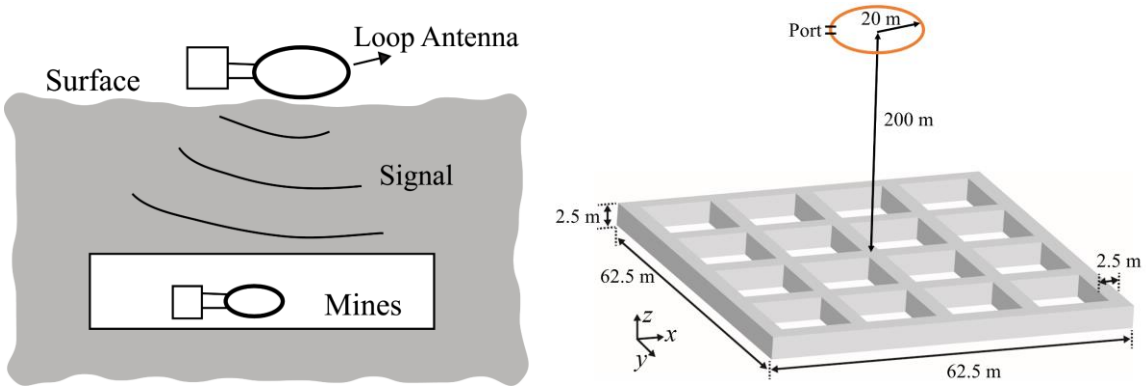

(a) (b)

Figure 5.4 (a) TTE communication system. (b) UQ example of the TTE system.

The UQ example characterizes a TTE system in a mine gallery located 200 m underground is analyzed [Figure 5.4 (b)]. The gallery is filled with air and surrounded by homogeneous lossy dielectric whose relative permittivity is 3.0, relative permeability is 1.0 and conductivity is 0.01. The gallery occupies horizontally a 62.5 m by 62.5 m area and the cross section of each tunnel is 2.5 m by 2.5 m. A magnetic dipole, which is used to model the transmitting loop antenna at 5000 Hz, locates at (x, y, z) and is oriented towards (θ, φ). Variables x, y, z, θ, and φ are uniformly distributed in the region [-0.5, 0.5] m, [-0.5, 0.5] m, [-200.5, -199.5] m, [0, 10] degree and [0, 360] degree, respectively. The observables are the real and imaginary part the current flowing on the port of

receiving loop antenna, which is modeled by a PEC loop strip with 20 cm width. The load is conjugate matching. Table 5-3 presents these observables' averages and standard deviations computed by both direct Monte Carlo (MC) methods and the proposed EM+UQ framework. Additionally, probability density functions of these observables are estimated via 5000-point MC simulation performed on the HDMR constructed surrogate model and compared with those directly obtained via MC simulations [Figure 5.5 (a)-(b)].

Apparently, the proposed EM-UQ framework can provide accurate averages and standard deviations for the real and imaginary part of port current. Subsequently, the surrogate models for characterizing the real and imaginary part of port current are used to characterize the magnitude and phase of port current, which are what really interested in practice. The means and standard deviations are compared with direct MC simulations [Table 5-4]. The PDFs of the magnitude and phase are present [Figure 5.5 (c)-(d)]. Again, the statistics of both methods match very well to each other.

Statistics	Observables	Direct MC	Proposed framework
Mean	Real part of currents	4.0919e-07	4.2060e-07
	Imaginary part of currents	-7.3388e-7	-7.3966e-07
Standard deviation	Real part of currents	5.1608e-06	5.1542e-06
	Imaginary part of currents	2.5636e-06	2.6385e-06
Number of simulations	Real part of currents	5000	329
	Imaginary part of currents	5000	679

Table 5-3 Comparison of statistics and number of deterministic simulations obtained via direct MC method and the proposed framework for real and imaginary part of port current.

Statistics	Observables	Direct MC	Proposed framework
Mean	Magnitude of currents	4.14 uA	4.12 uA
	Phase of currents	8.26 degrees	7.76 degrees
Standard deviation	Magnitude of currents	4.10 uA	4.16 uA
	Phase of currents	110.2 degrees	111.35 degrees

Table 5-4 Comparison of statistics and number of deterministic simulations obtained via direct MC method and the proposed framework for magnitude and phase of port current.

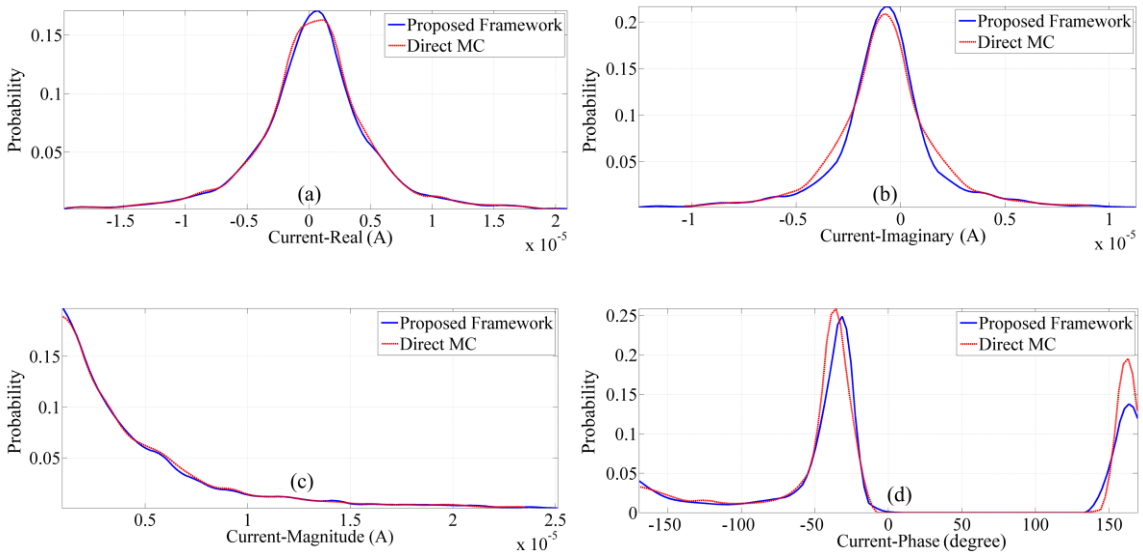

Figure 5.5 PDF of (a) the real part and (b) the imaginary part of port current. PDF of (c) magnitude and (d) phase of port current.

5.3.3 Medium Frequency Radio System

Medium frequency (MF) communications systems operate in the 300 kHz to 3 MHz band. It was developed as radio signals in the VHF (30 MHz to 300 MHz) and UHF band (300 MHz to 3 GHz) are restricted to line-of-sight coverage, and coverage cannot be provided around sharp corners and through rock falls. MF radio waves, in contrast,

can propagate through complex geometries as they are parasitically coupled to nearby existing metallic conductors within the mine environments [Figure 5.6]. These conductors, for example, can be existing mine telephone wire, rails, water pipes, or leaky feeder cables. Among them, solid copper twisted-pair phone wire and leaky feeder cable can serve as excellent conductors for propagation of MF signals because they are distributed continuously throughout the whole mine tunnels or galleries. In other words, the conductors inside mine tunnels act as part of a transmission line to transport the MF signal. They also act as distributed antennas and can receive and transmit MF signals. The MF systems are generally considered to be a secondary communications system because the hand-held device of a MF radio system is significantly bigger and heavier than a typical hand-held UHF or VHF radio and can hardly be carried by miners all the time [90]. That said, MF systems are useful as a secondary system for providing alternate survivable communications paths from a working section to the surface. For example, in an emergency event, MF communication would still be possible through conductors in existing boreholes extended from the surface to the mining sites.

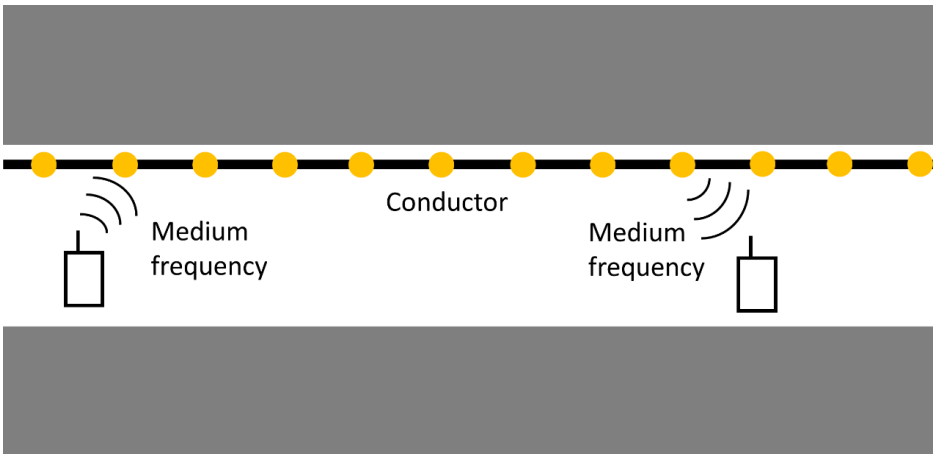

Figure 5.6 A simple medium frequency communication system.

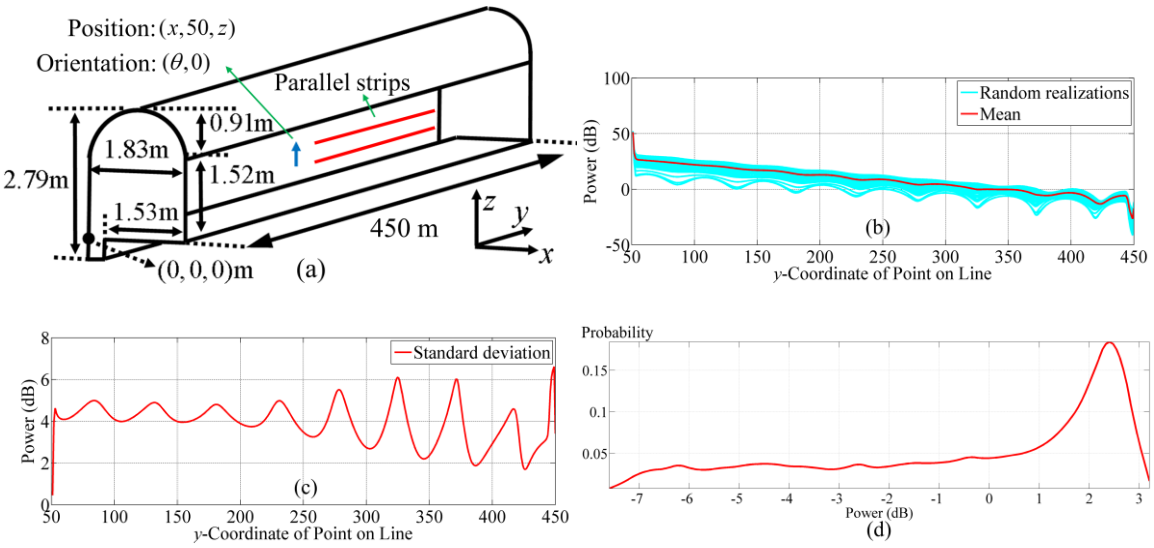

Figure 5.7 (a) Geometry of a 450-meter arched tunnel and the parallel strips modeling conductors. (b) Mean and some random realizations of power values along a line in center of the tunnel. (c) Standard deviation of power values along a line in the center of the tunnel (d) PDF of the power values at a selected receiver.

In order to determine what factors can affect the behavior of MF propagation in coal mines, extensive numerical and analytical modeling is required. The proposed full-wave EM-UQ framework is used to analyze the MF systems illustrated in Fig. This statistical analysis is performed in a 450-meter long arched tunnel with two parallel PEC strips modeling a transmission line inside the tunnel [Figure 5.7 (a)]. These strips, which are 400-m long, infinitesimally thin, 6 cm wide, and separated by 0.6 m, model a transmission line placed near the lateral tunnel wall and are centered at (0.17, 245, 0.87) m and (0.17, 245, 1.47) m. The full wave simulation is performed without FMM-FFT acceleration as the FMM-FFT algorithm is numerically unstable for low frequencies. The electric dipole used to model the transmitter is oriented in $(\theta,0)$ direction and operated at 3 MHz and located at $(x,50,z)$, where θ, x and z are the random variable uniformly

distributed in the range [0, 90], [0.875, 0.945] and [1.0, 1.44], respectively. Mean and standard deviation are obtained by the EM-UQ framework for the power values computed along a line connecting point (0.915, 51, 1.22) m to (0.915, 350, 1.22) m [Figure 5.7 (b)-(c)]. Finally, the PDF of the power values at point (0.915, 320, 1.22) m are computed and presented [Figure 5.7 (d)]. 41 deterministic simulations are required in this example.

5.3.4 Wireless Node-Based Mesh Network

Wireless mesh network systems typically operate at 0.5-6 GHz. It uses small distributed transceivers called nodes to wirelessly transmit and receive signals. Mesh network systems have attracted considerable interest from the mining community. In contrast to a conventional leaky feeder analog UHF or VHF radio system where all the mobile radios may hear the messages in broadcast fashion, the mesh systems enable person-to-person information exchange such as calling and text messaging. Moreover, node-based communication systems are quite flexible. It can use any of the available network topologies to obtain best signal coverage within interested area and can also increase the system survivability by building redundant routes in a wireless network. In a wireless mesh network, transceivers can transmit, receive, act as a signal repeater, and route traffic to other devices within their RF range. A simple wireless mesh network is illustrated in Figure 5.8. During the communication, a mobile device, such as a hand-held radio, can access the network if it is within the service range of a fixed-position node. When a miner talks or sends a text message using his handset, a link is established with a nearby node. Using wireless links between nodes, the network transmits the miner's

information to the desired destination, either inside or outside the mine. For example, the orange dash line indicates the propagation of the signal between nodes and finally to the hand-held radio receiver. The topologies of this kind of network include line, bus, tree, ring, star, partial and full mesh. However, due to the complex layouts of mine environments, it is not practical to link the nodes into structured topologies, such as ring or line, or link each node to every other node to form a full mesh. Hence, partial mesh network is most commonly used in mines. In this section, the proposed EM-UQ framework will be used to analyze the partial mesh wireless systems.

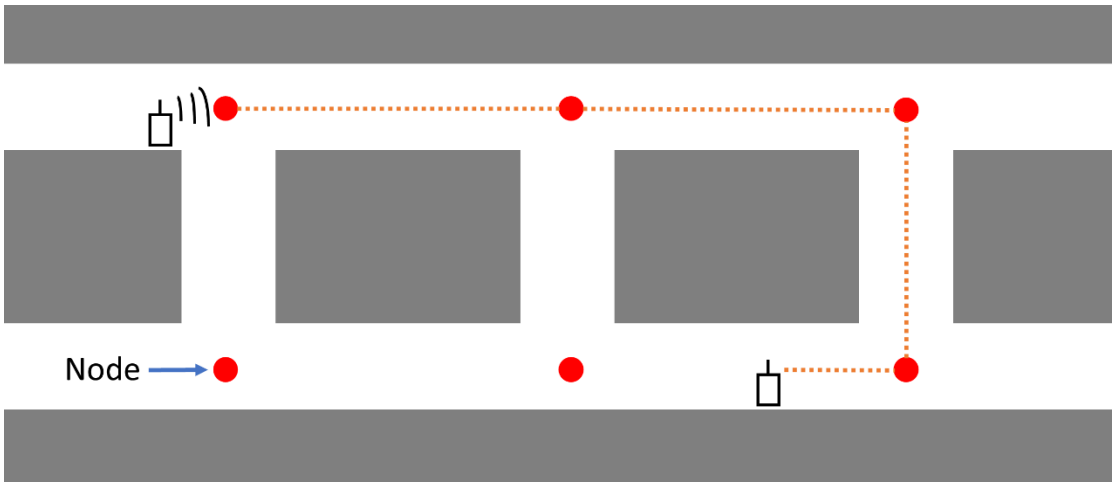

Figure 5.8 Cutaway view of mine with a wireless mesh node-based communications system

In the UQ example, the proposed EM-UQ is used to characterize the wave propagation of a wireless network in a mine gallery formed by six tunnels. In this gallery, three rectangular tunnels are extended along $x-$direction and are intersected with the other three tunnels extended along $y-$direction [Figure 5.9 (a)]. The height, width and length of these rectangular tunnels are 2.24 m, 1.85 m, and 45.55 m. The wireless

network is formed by four nodes operated at 900 MHz (IEEE 802.15.4 specification), each of which is modeled by a vertically place dipole with unit moment [Figure 5.9 (b)]. The positions of the three nodes are set as variables and listed in Table 5-5. The observables are the signal power received by two receivers located at $(45.0, 0.925, 1.12)$ m and $(32.775, -10.925, 1.12)$ m, respectively. Table 5-6 present these observables' averages and standard deviations computed by the proposed EM-UQ framework. Additionally, probability density functions of the observables are estimated via 5000-point MC simulation performed on the surrogate model constructed by our UQ framework [Figure 5.10 (a)-(b)]. A total of 61 simulations are required by the framework to build the surrogate model.

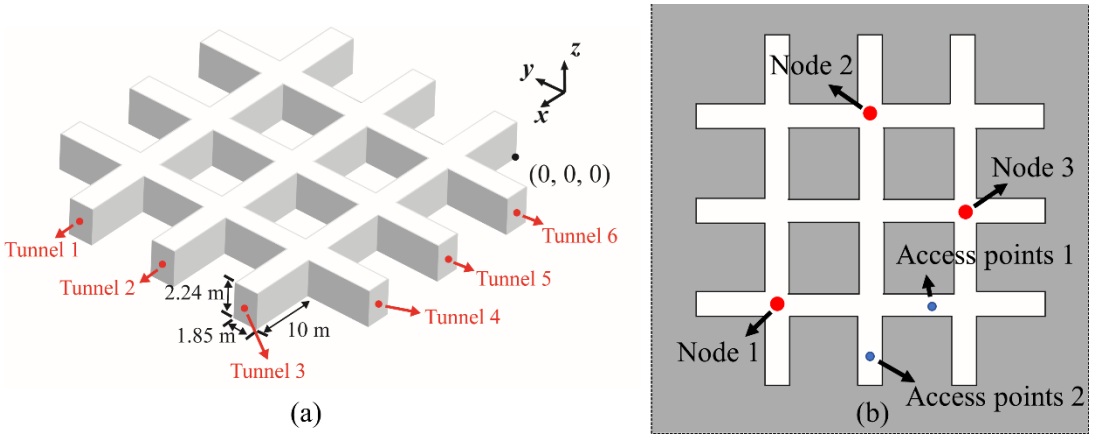

Figure 5.9 (a) Geometry of the mine gallery. (b) Approximate node locations and access points.

	Location	Variable	Distribution
Node 1	$(x_1, 0.925, 1.12)$	x_1	U(15.425, 16.425)
Node 2	$(32.775, y_2, 1.12)$	y_2	U(34.125, 35.125)
Node 3	$(x_3, 17.775, 1.12)$	x_3	U(49.225, 50.225)

Table 5-5 Variables defined in the location of nodes. U stands for uniform distribution.

Access Point No.	Statistics	Results by Proposed Framework
1	Mean	42.10 dB
	Standard Deviation	1.71
2	Mean	40.08 dB
	Standard Deviation	1.66

Table 5-6 Comparison of statistics and number of deterministic simulations obtained via the proposed framework.

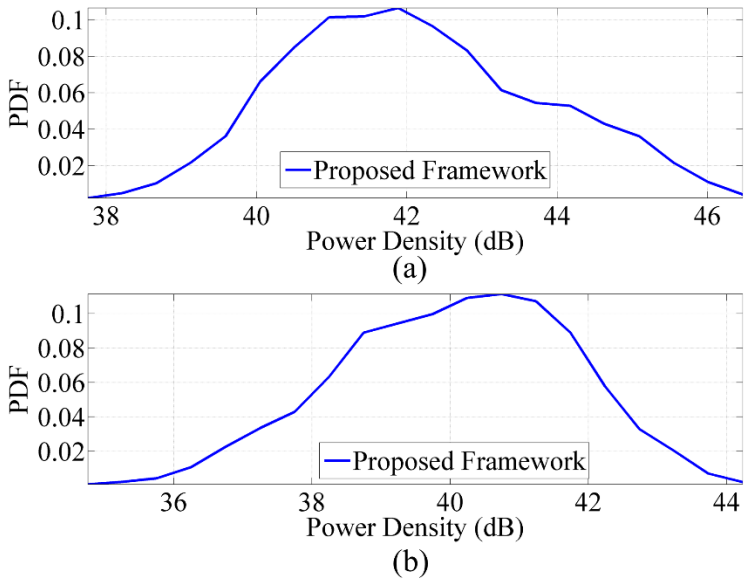

Figure 5.10 The probability density functions for power densities at (a) access point 1 and (b) access point 2.

5.4 Chapter Conclusion

The EM-UQ framework leveraging a ME-PC enhanced HDMR method in conjunction with proposed full-wave EM simulators tailored for statistically characterizing EM wave propagation in mine tunnels was presented. The technique yields PDFs of receiver field strengths accounting for uncertainty in mine layout and composition and can aid in to assess network reliability during normal operations. The framework allows for modeling of complete mines involving complex galleries and mile-long tunnels through the full-wave simulators and permits fast and faithful statistics analysis via the UQ tool. The simulations results demonstrated that the framework can successfully solve UQ problems for communications systems in mine environments.

CHAPTER 6
Compression of Scattering Matrices in Domain Decomposition Based Surface Integral Equation Simulator via Hierarchically Off-Diagonal Butterfly Factorization

6.1 Chapter Introduction

The design, (re)configuration, and EMC certification of wireless communication systems in underground mines call for powerful simulators capable of analyzing electromagnetic (EM) wave propagation in electrically large and complex mine tunnels and galleries. Full-wave EM simulators are a perfect fit for this task since they permit high-fidelity modeling of realistic mine environments and can be operated at desired frequencies. That said, full-wave EM simulators require enormous computational resources when used in EM analyses with multiple excitations, which arise in uncertainty quantifications and communication network optimizations. To reduce their costs, a memory and CPU efficient, full-wave, domain decomposition (DD)-based surface integral equation (SIE) simulator was proposed by Sheng et al [52, 70]. This simulator first divides mine tunnels or galleries into subdomains and defines equivalent surfaces for each subdomain using Huygens principle. Next, it proceeds to the offline stage that

computes scattering matrices to characterize EM wave propagation in each subdomain separately. Finally, it comes to the online stage to construct and solve a global inter-domain system that accounts for EM interactions between subdomains and has significantly less degrees of freedom compared to those of conventional fast simulators. When used for EM analyses with multiple excitations, the DD based SIE simulator oftentimes is significantly faster than conventional full-wave simulators since it only needs to update the right-hand side of the reduced inter-domain system and solve the reduced system for each different excitation during its online stage.

Unfortunately, the above simulator remains slow when applied to tunnels and galleries with electrically large cross sections, a situation that often arises when analyzing high frequency communication systems. The principal culprit is the high computational complexity of operations involving full scattering matrices. Indeed, the naïve solution of inter-domain systems requires $O(N_p^2 N_{sur})$ and $O(N_p^2)$ computational and memory resources, respectively; here N_p is the number of basis functions used to discretize one equivalent surface and N_{sur} is the number of equivalent surfaces. To alleviate the computational burden, the hierarchically off-diagonal butterfly factorization (HODBF) technique [91] is used to compress the scattering matrices and reduce the computational and memory requirements of iteratively solving inter-domain system to $O(N_p^{1.25} \log^2 N_p N_{sur})$ and $O(N_p^{1.25} \log^2 N_p)$, respectively. The idea of the HODBF technique is to hierarchically compress the off-diagonal blocks of a scattering matrix using a fast and efficient butterfly scheme [53, 66] that exploits the hierarchical low rank nature of those off-diagonal blocks to construct their multilevel sparse decompositions.

The compressed scattering matrices are constructed via a randomized scheme [91] requiring only "black box" matrix-vector multiplications of scattering matrices with structured random vectors. The accuracy, efficiency and applicability of the proposed HODBF enhanced DD based SIE simulator are demonstrated via characterization of EM wave propagation in various electrically large mine tunnels and galleries.

6.2 Scattering Matrices in DD Based SIE Simulator

The scattering matrices in DD based SIE simulator characterize the relation between input currents and output fields on the equivalent surface. Consider a tunnel that is surrounded by ore and split into four subdomains [Figure 6.1 (a)]. For subdomain Ω_b with two attached equivalent surfaces S_1 and S_2 [Figure 6.1 (b)], the scattering matrix $\mathbf{Z}^b$ of Ω_b is defined as [70]

$$\mathbf{Z}^b\mathbf{I}=\begin{bmatrix}\mathbf{Z}_{11}^b & \mathbf{Z}_{12}^b\\ \mathbf{Z}_{21}^b & \mathbf{Z}_{22}^b\end{bmatrix}\begin{bmatrix}\mathbf{I}_1\\ \mathbf{I}_2\end{bmatrix}=\begin{bmatrix}\mathbf{V}_1^{sca}\\ \mathbf{V}_2^{sca}\end{bmatrix}, \tag{6.1}$$

where the scattering matrix $\mathbf{Z}^b$ is formed by 2×2 scattering submatrices. $\mathbf{I}_p$ is the vector holding the unknown expansion coefficients of the RWG basis function discretized currents on S_p, $p\in\{1,2\}$. $\mathbf{V}_q^{sca}$ is the vector formed by the vectors of scattering electric fields $\mathbf{E}_q^{sca}$ and scattering magnetic fields $\mathbf{H}_q^{sca}$ tested on S_q, as $\mathbf{V}_q^{sca}=[\mathbf{E}_q^{sca};\mathbf{H}_q^{sca}]$, $q\in\{1,2\}$. The scattering submatrix $\mathbf{Z}_{qp}^b$, $q,p\in\{1,2\}$, maps the

currents on S_p to the scattered fields on S_q by accounting for the wave propagation characteristics of Ω_b.

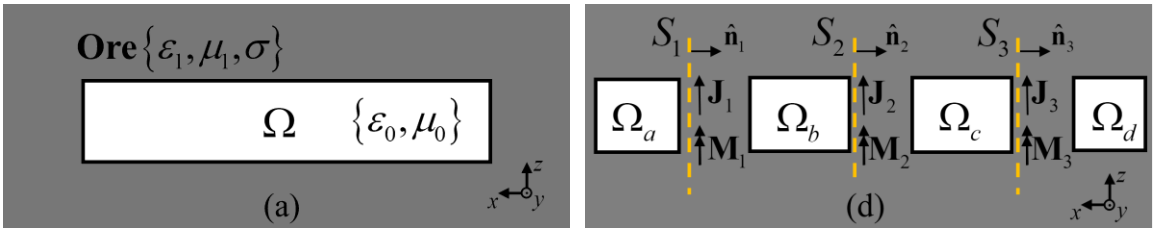

Figure 6.1 (a) A tunnel surrounded by ore. (b) subdomains and associated equivalent surfaces

By obtaining the scattering matrices for all subdomains of this tunnel, the inter-domain system that accounts for the interaction between subdomains can be formed as [70]

$$\begin{bmatrix} \mathbf{Z}_{11}^a + \mathbf{Z}_{11}^b & \mathbf{Z}_{12}^b & 0 \\ \mathbf{Z}_{21}^b & \mathbf{Z}_{22}^b + \mathbf{Z}_{22}^c & \mathbf{Z}_{23}^c \\ 0 & \mathbf{Z}_{32}^c & \mathbf{Z}_{33}^c + \mathbf{Z}_{33}^d \end{bmatrix} \begin{bmatrix} \mathbf{I}_1 \\ \mathbf{I}_2 \\ \mathbf{I}_3 \end{bmatrix} = \begin{bmatrix} \mathbf{V}_1^{inc} \\ \mathbf{V}_2^{inc} \\ \mathbf{V}_3^{inc} \end{bmatrix}, \tag{6.2}$$

where $\mathbf{V}_p^{inc}$ is the vector of tested incident electric and magnetic fields on S_p due to impressed sources in the subdomains touching to S_p. Note that only equivalent surfaces touching the same subdomain can interact due to the highly lossy background. The inter-domain system is solved to obtain the unknown coefficients of the currents on S_p, $p = 1,...,3$, which are then used to compute the currents on Ω_i, $i = a,...,d$, and hence fields anywhere inside the tunnel.

To iteratively solve the inter-domain system, one must perform a number of matrix-vector multiplications on the scattering matrices in (6.2). The computational and memory

complexity of these operations involving full scattering matrices scales as $O(N_p^2)$, where N_p is the number of basis functions used to discretize one equivalent surface. When it comes to tunnels and galleries with electrically large cross sections, this computational cost becomes high and can greatly slow down the solution of inter-domain system.

6.3 Compression of Scattering Matrices

To alleviate the computational burden, the HODBF method is proposed to compress the scattering matrices and reduce the computational and memory requirements. The HODBF matrices, as one class of the hierarchical matrices, are used as data-sparse approximations of dense matrices [92]. In this section, the scattering matrix in Eq. are compressed into the HODBF structure with the butterfly compressed off-diagonal blocks. To do so, the scheme first hierarchically bisects the two equivalent surfaces into several levels according to a specific partition strategy. Next, it uses a randomized scheme to obtain the butterfly factorization for the off-diagonal blocks of the scattering matrix.

6.3.1 Partition Strategy

The defining characteristics of HODBF matrices is that the off-diagonal blocks representing interactions between two non-intersecting subscatterers can be efficiently compressed. Hence, the partition strategy proceeds as follows. In the first level, the two equivalent surfaces are separated since they only have far-field interactions. In the second level, the tunnel interfaces and the rest of the surfaces are separated. The other levels then hierarchically divide the geometry into two halves until the finest-level blocks contain

only $O(1)$ basis functions. The strategy is illustrated via an example of 6-level partition of the two equivalent surfaces [Figure 6.2].

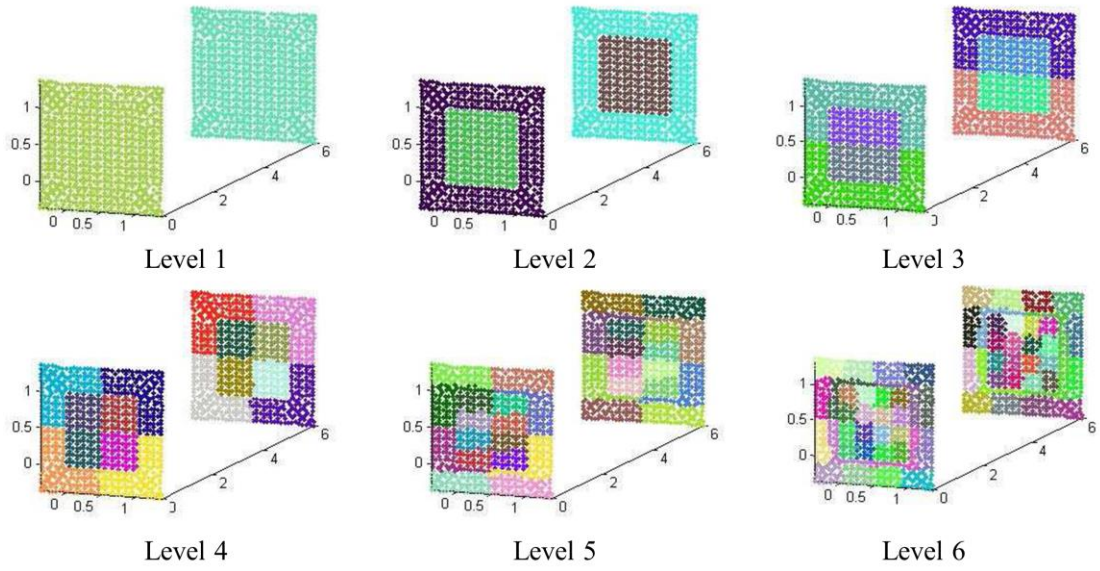

Figure 6.2 An example of 6-level partition of two equivalent surfaces

6.3.2 HODBF Structure

The HODBF matrix is better illustrated using an example. A 2-level HODBF structure of the scattering matrix can be written as [92]

$$\mathbf{Z}=\begin{bmatrix}\mathbf{K}_1^1 & \mathbf{K}_{1,2}^1\\ \mathbf{K}_{2,1}^1 & \mathbf{K}_2^1\end{bmatrix}=\begin{bmatrix}\begin{bmatrix}\mathbf{K}_1^2 & \mathbf{K}_{1,2}^2\\ \mathbf{K}_{2,1}^2 & \mathbf{K}_2^2\end{bmatrix} & \mathbf{K}_{1,2}^1\\ \mathbf{K}_{2,1}^1 & \begin{bmatrix}\mathbf{K}_3^2 & \mathbf{K}_{3,4}^2\\ \mathbf{K}_{4,3}^2 & \mathbf{K}_4^2\end{bmatrix}\end{bmatrix}. \tag{6.3}$$

Let $\mathbf{K}_i^l$ represent the ith diagonal blocks at l-level and $\mathbf{K}_{i,j}^l$ represent the off-diagonal blocks that are to be compressed, a L-level HODBF matrix is the one with its ith diagonal blocks at l-level written as

$$\mathbf{K}_i^l = \begin{bmatrix} \mathbf{K}_{2i-1}^{l+1} & \mathbf{K}_{2i-1,2i}^{l+1} \\ \mathbf{K}_{2i,2i-1}^{l+1} & \mathbf{K}_{2i}^{l+1} \end{bmatrix}, \tag{6.4}$$

where $l = 0, ..., L-1$ and $i = 1, ..., 2^l$. The pictorial representation of a 2-level hierarchical matrix structure is shown in Figure 6.3.

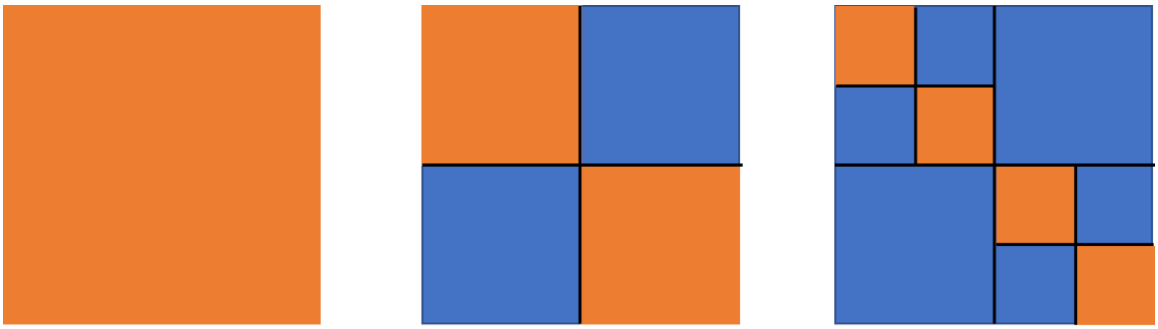

Figure 6.3 2-level HODBF matrix structure. Blue area represents off-diagonal blocks to be compressed via butterfly factorization, while orange area represents full matrix blocks.

The off-diagonal blocks of the scattering matrix may be compressed via either low-rank algorithms or butterfly algorithm. However, the computational and memory complexities of low-rank algorithms can deteriorate to $O(N^{\alpha}\log^{\beta} N)$ ($\alpha \geq 1.5$, $\beta \geq 1$) and $O(N^{\alpha}\log N)$ ($\alpha \geq 1.5$) for applying the LR-compressed blocks to matrix-vector multiplications since the scattering matrices in DD based SIE simulator represent EM interactions on electrically large objects [53, 91]. In contrast, the butterfly scheme can exploit the hierarchical low-rank nature of the off-diagonal blocks in high frequency regime and efficiently apply the multilevel sparse decompositions of these blocks to matrix-vector multiplications in $O(N^{1.25}\log^2 N)$ computational and memory complexities [91].

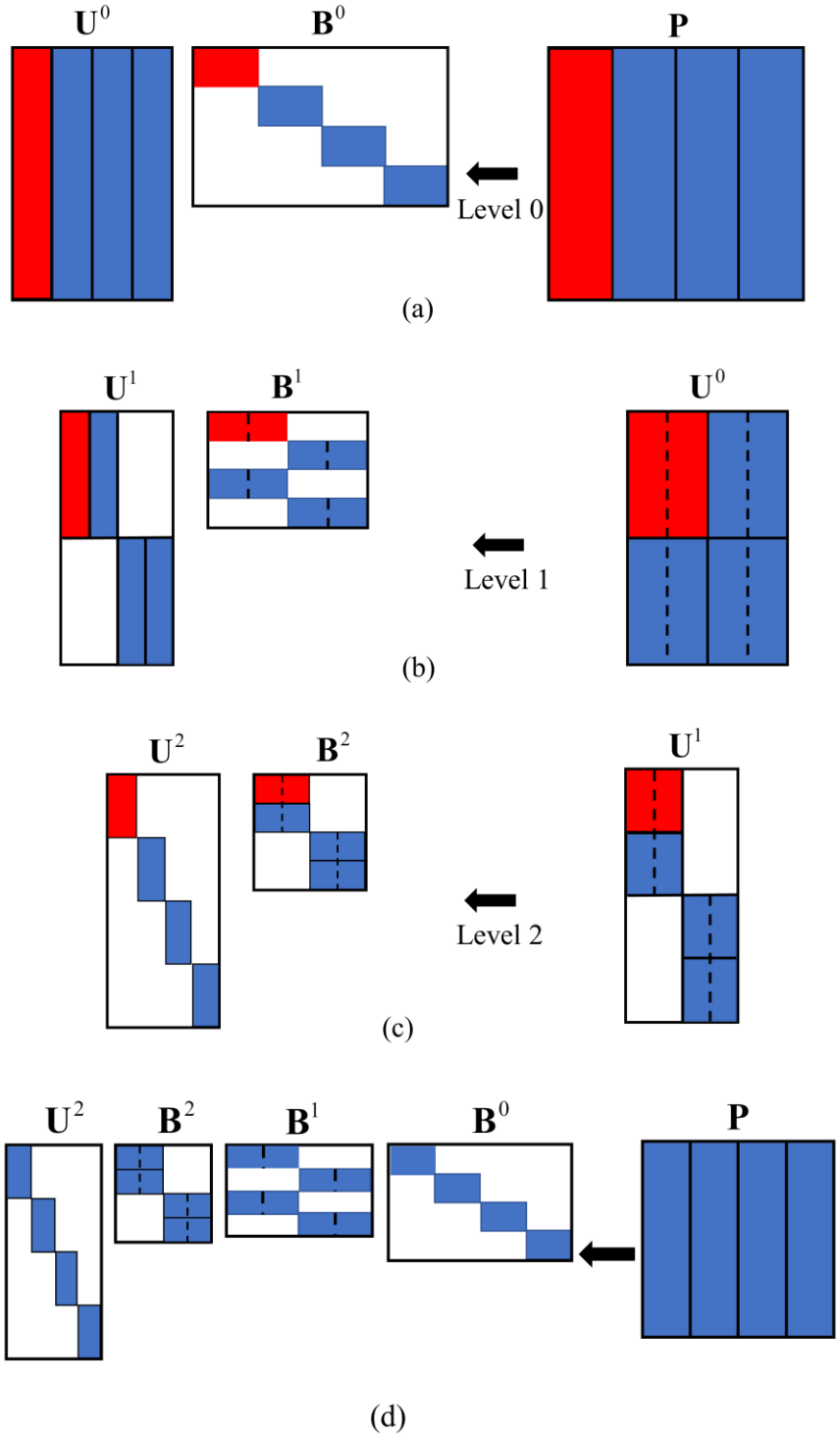

Figure 6.4 Pictorial illustration of butterfly factorization: (a) level-0 factorization, (b) level-1 factorization, (c) level-2 factorization, and (d) 2-level butterfly factorization.

To illustrate the butterfly factorization of an off-diagonal block, consider a l-level $m \times n$ block $\mathbf{P} = \mathbf{K}_{1,2}^{l}$ with $m \approx n \approx N_p / 2^l$ as an example. Let $C = \{1, ..., n\}$ be the column index set and $R = \{1, ..., m\}$ be the row index set. C and R are recursively bisected into a binary tree structure with $V = L - l$ butterfly levels (in practice, however, the number of butterfly levels are adjusted according to empirical knowledge of ranks at each HODBF level). At level $v \in \{0, ..., V\}$, there are 2^v column index subsets C_j^v, $j = 1, ..., 2^v$, and row index subsets R_i^v, $i = 1, ..., 2^v$, of approximate size $n/2^v$ and $m/2^v$, respectively. Let $\mathbf{P}_{i,j}^v = \mathbf{P}_{R_i^v, C_j^{V-v}}$ be the submatrix of $\mathbf{P}$ corresponding to R_i^v and C_j^{V-v}, the butterfly factorization of $\mathbf{P}$ can be constructed by applying low-rank decomposition to $\mathbf{P}_{i,j}^v$ (after the level 0, it is reduced-order representation of $\mathbf{P}_{i,j}^v$). The low-rank decomposition is not necessarily unique and can be constructed via interpolative decomposition [93], adaptive cross approximation [66, 94], and so on. Denoting the maximum rank for all submatrices $\mathbf{P}_{i,j}^v$ as k, the butterfly factorization of $\mathbf{P}$ is described level by level in what follows [53, 91] (As an example, a 2-level butterfly factorization of a block is shown in Figure 6.4).

At level 0, the submatrices $\mathbf{P}_{1,j}^0$, $j = 1, ..., 2^V$, are decomposed as $\mathbf{P}_{1,j}^0 = \mathbf{U}_{1,j}^0 \mathbf{B}_{1,j}^0$, where $\mathbf{U}_{1,j}^0$ is of size $m \times k$ and $\mathbf{B}_{1,j}^0$ is of size $k \times n/2^V$. Note that the subscripts and superscript of $\mathbf{U}_{i,j}^v$ and $\mathbf{B}_{i,j}^v$ are only for numbering and do not necessarily relate to R_i^v and C_j^v. The resulting factorization of $\mathbf{P}$ is [Figure 6.4 (a)]

$$\mathbf{P} = \mathbf{U}^0 \mathbf{B}^0, \tag{6.5}$$

where $\mathbf{U}^0 = \begin{bmatrix} \mathbf{U}^0_{1,1} & \cdots & \mathbf{U}^0_{1,2^V} \end{bmatrix}$ and $\mathbf{B}^0 = diag(\mathbf{B}^0_{1,1}, ..., \mathbf{B}^0_{1,2^V})$.

At level 1, the submatrices $\mathbf{U}^0_{1,j}$, $j = 1,...,2^V$, are first row-wise bisected as $\mathbf{U}^0_{1,j} = (\mathbf{U}^1_{1,j}; \mathbf{U}^1_{2,j})$, $j = 1,...,2^V$. Next, $\mathbf{U}^1_{i,j}$ are column-wise paired as $\mathbf{N}^1_{i,j} = (\mathbf{U}^1_{i,2j-1}, \mathbf{U}^1_{i,2j})$, $i = 1,2$, $j = 1,...,2^{V-1}$. Here, $(\cdot;\cdot)$ and $(\cdot,\cdot)$ denote the column and row concatenation, respectively. The new submatrices $\mathbf{N}^1_{i,j}$ are then factorized as $\mathbf{N}^1_{i,j} = \mathbf{U}^1_{i,j}\mathbf{B}^1_{i,j}$, $i = 1,2$, $j = 1,...,2^{V-1}$, where $\mathbf{U}^1_{i,j}$ are of size $m/2 \times k$ and $\mathbf{B}^1_{i,j}$ are of size $k \times 2k$. At this level, the factorization of $\mathbf{P}$ becomes [Figure 6.4 (b)]

$$\mathbf{P} = \mathbf{U}^1\mathbf{B}^1\mathbf{B}^0 , \tag{6.6}$$

where $\mathbf{U}^1 = diag(\mathbf{U}^1_1, \mathbf{U}^1_2)$ and $\mathbf{U}^1_i = \begin{bmatrix} \mathbf{U}^1_{i,1} & \cdots & \mathbf{U}^1_{i,2^{V-1}} \end{bmatrix}$. $\mathbf{B}^1 = (\mathbf{B}^1_1; \mathbf{B}^1_2)$ and $\mathbf{B}^1_i = diag(\mathbf{B}^1_{i,1}, ..., \mathbf{B}^1_{i,2^{V-1}})$.

At level $v = 2,...,V$, the method proceeds in a similar manner. It first row-wise bisects submatrices $\mathbf{U}^{v-1}_{i,j}$ as $(\mathbf{U}^v_{2i-1,j}; \mathbf{U}^v_{2i,j})$, $j = 1,...,2^{V-v+1}$ and column-wise pairs them to form new submatrices as $\mathbf{N}^v_{i,j} = (\mathbf{U}^v_{i,2j-1}, \mathbf{U}^v_{i,2j})$, $i = 1,..,2^v$, $j = 1,...,2^{V-v}$. Then it factorize $\mathbf{N}^v_{i,j}$ as $\mathbf{N}^v_{i,j} = \mathbf{U}^v_{i,j}\mathbf{B}^v_{i,j}$, $i = 1,..,2^v$, $j = 1,...,2^{V-v}$, where $\mathbf{U}^v_{i,j}$ are of size $m/2^v \times k$ and $\mathbf{B}^v_{i,j}$ are of size $k \times 2k$. Finally, the butterfly factorization for the block $\mathbf{P}$ is (level-2 structure is shown as an example in Figure 6.4 (c)).

$$\mathbf{P} = \mathbf{U}^V\mathbf{B}^V \cdots \mathbf{B}^1\mathbf{B}^0, \tag{6.7}$$

where $\mathbf{U}^V = diag(\mathbf{U}^V_{1,1}, \cdots, \mathbf{U}^V_{2^V,1})$. $\mathbf{B}^v = diag((\mathbf{B}^v_1; \mathbf{B}^v_2), \cdots, (\mathbf{B}^v_{2^v-1}; \mathbf{B}^v_{2^v}))$ and $\mathbf{B}^v_i = diag(\mathbf{B}^v_{i,1}, ..., \mathbf{B}^v_{i,2^{V-v}})$, $v = 0, ..., V$. Figure 6.4 (d) shows the pictorial representation of a 2-level butterfly factorization.

6.3.3 Randomized Scheme

As demonstrated in previous literature [91], it is computationally expensive to obtain the HODBF structure for a scattering matrix by directly compressing its full matrix since its entries are computed via matrix-vector multiplications. In this section, a fast scheme that relies on multiplications of the scattering matrix and random vectors is used to construct its HODBF structure and alleviate the computational burden.

A repeatedly used algorithm in the construction of HODBF is the randomized butterfly scheme that constructs butterfly factorization for a matrix. For the $m \times n$ block $\mathbf{P}$ with butterfly rank k, the algorithm to construct its V level butterfly factorization is described as follows [53, 91]:

Step 1: Generate an auxiliary butterfly-factorized matrix $\mathbf{T}$ such that

$$\mathbf{T} = \mathbf{L}^V \mathbf{R}^V \cdots \mathbf{R}^1 \mathbf{R}^0 . \tag{6.8}$$

The matrix $\mathbf{L}^V$ and $\mathbf{R}^v$, $v = 1, ..., V$, respectively, have the same dimension and structure as $\mathbf{U}^V$ and $\mathbf{B}^v$, $v = 1, ..., V$, in (6.7) and their entries are filled with independent and identically distributed (i.i.d) standard Gaussian random variables. Let $v_c = \lfloor V/2 \rfloor$ with $\lfloor \cdot \rfloor$ rounding downwards.

Step 2: For $v = 0,...,v_c$; For $i = 1,...,2^v$; Generate a $k \times m$ structured matrix $\mathbf{G}_1$ whose columns are i.i.d Gaussian random variables if they belong to $\mathbf{R}_{i,j}^v$ (or $\mathbf{B}_{i,j}^v$), $j = 1,...,2^{V-v}$, and zero otherwise. Compute $\mathbf{Q}_o^{'}$ as

$$\mathbf{Q}_o^{'} = \mathbf{G}_1 \mathbf{P} (\mathbf{R}^0)^T \cdots (\mathbf{R}^{v-1})^T , \tag{6.9}$$

and compute $\mathbf{Q}_i^{'} = \mathbf{Q}_o^{'} (\mathbf{R}^v)^T$. Note that $\mathbf{Q}_o^{'} = \mathbf{G}_1 \mathbf{P}$ when $v = 0$. Next, extract a $k \times k$ submatrix $\mathbf{Q}_i$ and a $k \times 2k$ submatrix $\mathbf{Q}_o$ from entries in $\mathbf{Q}_i^{'}$ and $\mathbf{Q}_o^{'}$ that belong to $\mathbf{R}_{i,j}^v$, and compute $\mathbf{B}_{i,j}^v$ as $\mathbf{B}_{i,j}^v = \mathbf{Q}_i^{\dagger} \mathbf{Q}_o$, where † stands for the pseudoinverse and $j = 1,...,2^{V-v}$.

Step 3: For $v = V+1,...,v_c+1$; For $i = 1,...,2^{V-v}$; Generate a $n \times k$ structured matrix $\mathbf{G}_2$ whose columns are i.i.d Gaussian random variables if they belong to $\mathbf{R}_{i,j}^v$ (or $\mathbf{B}_{i,j}^v$), $j = 1,...,2^{V-v}$ and zero otherwise. Compute $\mathbf{Q}_o^{'}$ as

$$\mathbf{Q}_o^{'} = (\mathbf{R}^{v+1})^T \cdots (\mathbf{L}^V)^T \mathbf{P} \mathbf{G}_2 . \tag{6.10}$$

In addition, compute $\mathbf{Q}_i^{'} = \mathbf{B}^{v_c} \cdots \mathbf{B}^0 \mathbf{G}_2$ when $v = v_c + 1$ and $\mathbf{Q}_i^{'} = (\mathbf{R}^v)^T \mathbf{Q}_o^{'}$ otherwise. Note that $\mathbf{Q}_o^{'} = \mathbf{P} \mathbf{G}_2$ and $\mathbf{Q}_o^{'} = \mathbf{L}^V \mathbf{P} \mathbf{G}_2$ when $v = V+1$ and $v = V$, respectively. Next, extract a $k \times k$ submatrix $\mathbf{Q}_i$ and a $2k \times k$ submatrix $\mathbf{Q}_o$ from entries in $\mathbf{Q}_i^{'}$ and $\mathbf{Q}_o^{'}$ that belong to $\mathbf{R}_i^v$, and compute $\mathbf{B}_i^v$ as $\mathbf{B}_i^v = \mathbf{Q}_o \mathbf{Q}_i^{\dagger}$ (or $\mathbf{U}_{i,1}^V$ when $v = V+1$), where † stands for the pseudoinverse and $j = 1,...,2^{V-v}$.

Upon completion of above three steps, the butterfly factorization of block $\mathbf{P} = \mathbf{U}^V \mathbf{B}^V \cdots \mathbf{B}^1 \mathbf{B}^0$ is constructed. The HODBF structure of a scattering matrix can then be constructed by repeatedly using this randomized butterfly algorithm for all the off-diagonal blocks. For example, to obtain the butterfly factorization for the block $\mathbf{K}_{1,2}^1$, we simply multiply the scattering matrix with the random vectors required by the randomized butterfly scheme. This can be done by performing:

$$\mathbf{ZI} = \begin{bmatrix} \mathbf{K}_1^1 & \mathbf{K}_{1,2}^1 \\ \mathbf{K}_{2,1}^1 & \mathbf{K}_2^1 \end{bmatrix} \begin{bmatrix} 0 \\ \mathbf{I}_1 \end{bmatrix} = \begin{bmatrix} \mathbf{K}_{1,2}^1 \mathbf{I}_1 \\ \mathbf{K}_2^1 \mathbf{I}_1 \end{bmatrix}, \text{ and} \tag{6.11}$$

$$\mathbf{I}^T \mathbf{Z} = \begin{bmatrix} \mathbf{I}_2 & 0 \end{bmatrix} \begin{bmatrix} \mathbf{K}_1^1 & \mathbf{K}_{1,2}^1 \\ \mathbf{K}_{2,1}^1 & \mathbf{K}_2^1 \end{bmatrix} = \begin{bmatrix} \mathbf{I}_2 \mathbf{K}_1^1 & \mathbf{I}_2 \mathbf{K}_{1,2}^1 \end{bmatrix}, \tag{6.12}$$

where $\mathbf{I}_1$ and $\mathbf{I}_2$ are random vectors used in the randomized butterfly algorithm (such as $\mathbf{G}_2$ and $\mathbf{G}_1$). By extracting the parts related to $\mathbf{K}_{1,2}^1$ in right-hand sides of (6.11) and (6.12), we can obtain the information (matrix-vector multiplication results) required by the randomized butterfly algorithm and consequently obtain the butterfly factorization for $\mathbf{K}_{1,2}^1$. Other off-diagonal blocks in the scattering matrix can be compressed using the similar procedure. More details are referred to [95].

6.3.4 Cost Analysis

The CPU and memory complexities to construct the butterfly factorization for the off-diagonal blocks and apply the factorization to matrix-vector multiplication depend on the butterfly rank k. For the off-diagonal blocks that represents only far-field interactions,

k is approximately constant. Based on this assumption, previous literature [53, 91, 96] proved that the CPU and memory requirements for constructing the butterfly factorizations of such blocks are $O(n^{1.5}\log n)$ and $O(n\log n)$, while applying the factorization to matrix-vector multiplications requires $O(n\log^2 n)$ CPU and memory resources. That said, in the HODBF structure, the butterfly rank will increase as the off-diagonal blocks hold near-field interactions (except the first level). Generally, the butterfly rank k is dominated by the ranks of the submatrices at the center level $V/2$, which actually represent the interaction between a group of $O(n^{0.5})$ observers and a group of $O(n^{0.5})$ sources on the surface. Although the ranks for well-separated or corner-sharing pairs are approximately constant (up to a logarithmic factor), the ranks for edge-sharing pairs scale as $O(n^{0.25})$ as there are $O(n^{0.25})$ sources and observers have near-field interactions. Hence, the CPU and memory complexities for obtaining the butterfly factorization for the off-diagonal blocks in HODBF structure are $O(n^{1.75}\log n)$ and $O(n^{1.25}\log n)$, respectively, while $O(n^{1.25}\log^2 n)$ CPU and memory resources are required to apply the compressed blocks to matrix-vector multiplications. As a result, the overall computational and memory requirements for applying HODBF compressed scattering matrix to matrix-vector multiplications are $O(N_p^{1.25}\log^2 N_p)$.

6.4 Numerical Results

This section first demonstrates the efficiency of the proposed HODBF enhanced DD based SIE simulator via comparing the computational cost and memory requirement

of the enhanced simulator with those of the original DD simulator computing full scattering matrices. It next demonstrates the accuracy and applicability of the enhanced simulator via characterization of wave propagation in various mine tunnels. In all examples below, mine tunnels has air inside and are surrounded by ore with relative permittivity $\varepsilon_r = 8.9$, relative permeability $\mu_r = 1$, and conductivity $\sigma = 0.15$ S/m , where ε_r , μ_r , σ are related to ε_1 and μ_1 via $\mu_1 = \mu_r \mu_0$ and $\varepsilon_1 = \varepsilon_0 \varepsilon_r - j\sigma/\omega$. The mine tunnels are excited by an infinitesimal electric dipole with unit moment. The power values obtained by the proposed simulator and other methods are normalized to their maxima and are expressed in logarithmic units. The proposed simulator was implemented using hybrid message passing interface/open multiprocessing (MPI/OpenMP) standards and executed on a cluster of dual hexacore X5650 Intel processors located at the Center for Advanced Computing, University of Michigan, Ann Arbor, MI, USA.

6.4.1 Performance Comparison

To compare the performance of the enhanced and original DD simulator, the wave propagation inside a rectangular straight tunnel is characterized. Hence, the scattering matrices compressed by HODLR method are obtained via characterization of a subdomain with two equivalent surfaces. In all simulations below, the tunnel is decomposed into 11 identical subdomains and a TFQMR iterative solver [36] is used to solve the inter-domain system. Both the full scattering matrices and HODLR compressed scattering matrices are used to construct the inter-domain systems. The average CPU time per iteration and the memory requirement for each iterative solution are measured for comparing the computational and memory complexities.

First, the cross section of the tunnel is set as 1.85 m × 2.24 m. The size of scattering matrix is varied by fixing the cross section of the tunnel but varying the frequency. The sizes of scattering matrices are 3720 × 3720, 10268 × 10268, 21904 × 21904, and 33072 × 33072, obtained at 150 MHz, 300 MHz, 455 MHz, and 600 MHz, respectively. Memory requirement and average CPU time per iteration are compared between the enhanced and original simulator [Figure 6.5 (a)-(b)]. Apparently, HODBF method reduced the computational and memory requirements of iterative solutions of the inter-domain system.

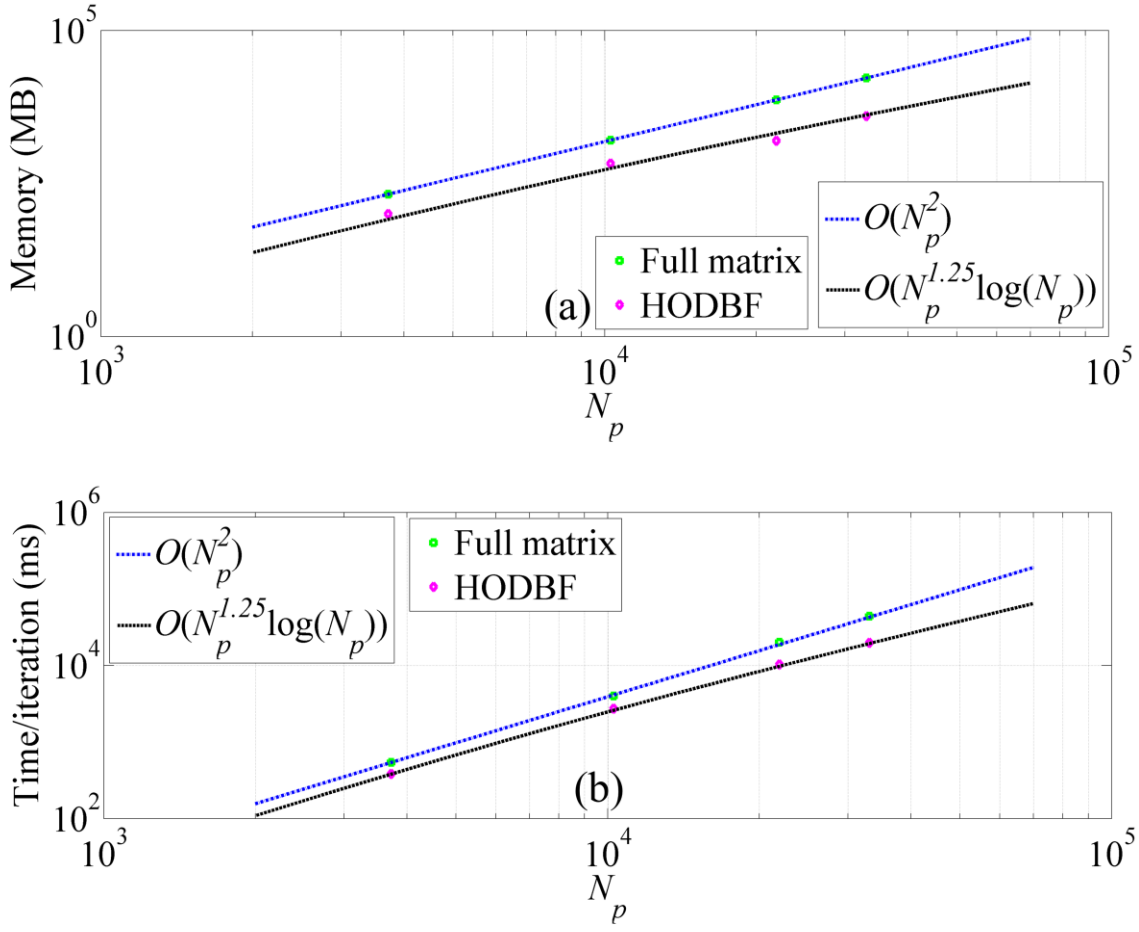

Figure 6.5 Comparison of (a) memory and (b) average CPU time per iteration for different frequencies.

Second, the size of scattering matrix is varied by fixing the frequency but varying the size of tunnel's cross section. The sizes of scattering matrices are 13252 × 13252, 21904 × 21904, 30720 × 30720, and 47592 × 47592, obtained with cross section's size of 1.48 m × 1.79 m, 1.85 m × 2.24 m, 2.22 m × 2.69 m, and 2.78 m × 3.36 m respectively. Memory requirement and average CPU time per iteration are compared between the enhanced and original simulator [Figure 6.6 (a)-(b)]. Again, HODBF method reduced the computational and memory requirements when solving the inter-domain system.

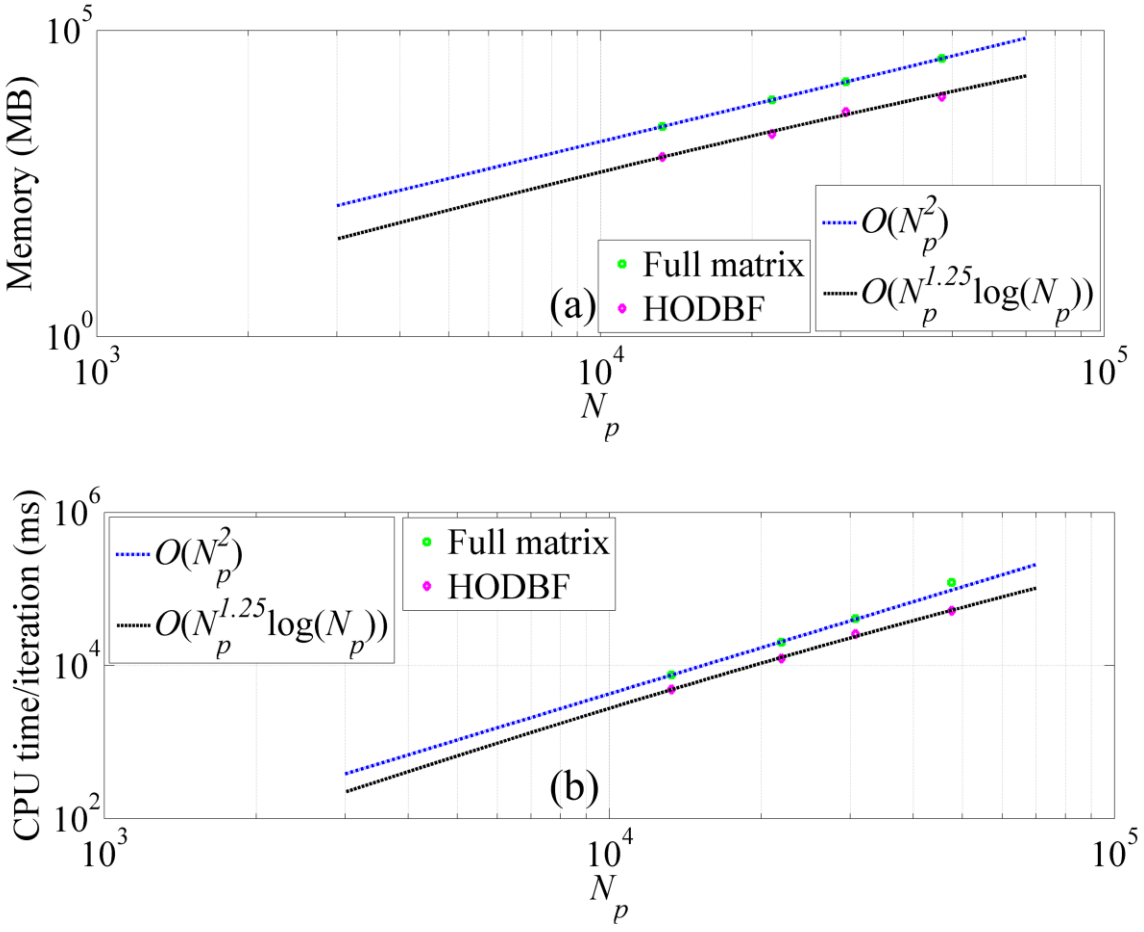

Figure 6.6 Comparison of (a) memory and (b) average CPU time per iteration for different sizes of cross section.

6.4.2 Wave Propagation in Tunnels

In this section, the accuracy and applicability of the proposed HODBF enhancement of DD based SIE simulator is demonstrated via characterization of EM wave propagations in straight rectangular and arched tunnels. In all scenarios, the threshold of the TFQMR iterative solver is 1×10^{-6} [36].

6.4.2.1 Rectangular Tunnels

A 450 m - long rectangular tunnel is excited by a $z-$ (vertically) oriented dipole at 455 MHz or 600 MHz [Figure 6.7 (a)]. In this scenario, the tunnel is decomposed into 150 identical 3 m - long subdomains for analysis at 455 MHz and 180 identical 2.5 - m long subdomains for analysis at 600 MHz; only one scattering matrix is computed for each frequency. At lower and higher frequencies, subdomains are discretized using 45648 and 66048 RWG basis functions, while the equivalent surfaces are discretized using 10952 and 33072 RWG basis functions, respectively. Power values on a line connecting (51.2, 0.915, 1.22) m and (450, 0.915, 1.22) m computed by the proposed simulator are compared with the multi-modal decomposition [39] after applying the normalizations accounting for different excitation mechanism [Figure 6.7 (b)-(c)]. Power values computed by the HODBF enhanced DD based SIE simulator are in good agreement with the multi-modal decomposition results, demonstrating the accuracy of the proposed simulator. The dynamic ranges of the simulator are around 110 dB and are reflected in Figure 6.7 (b) and (c).

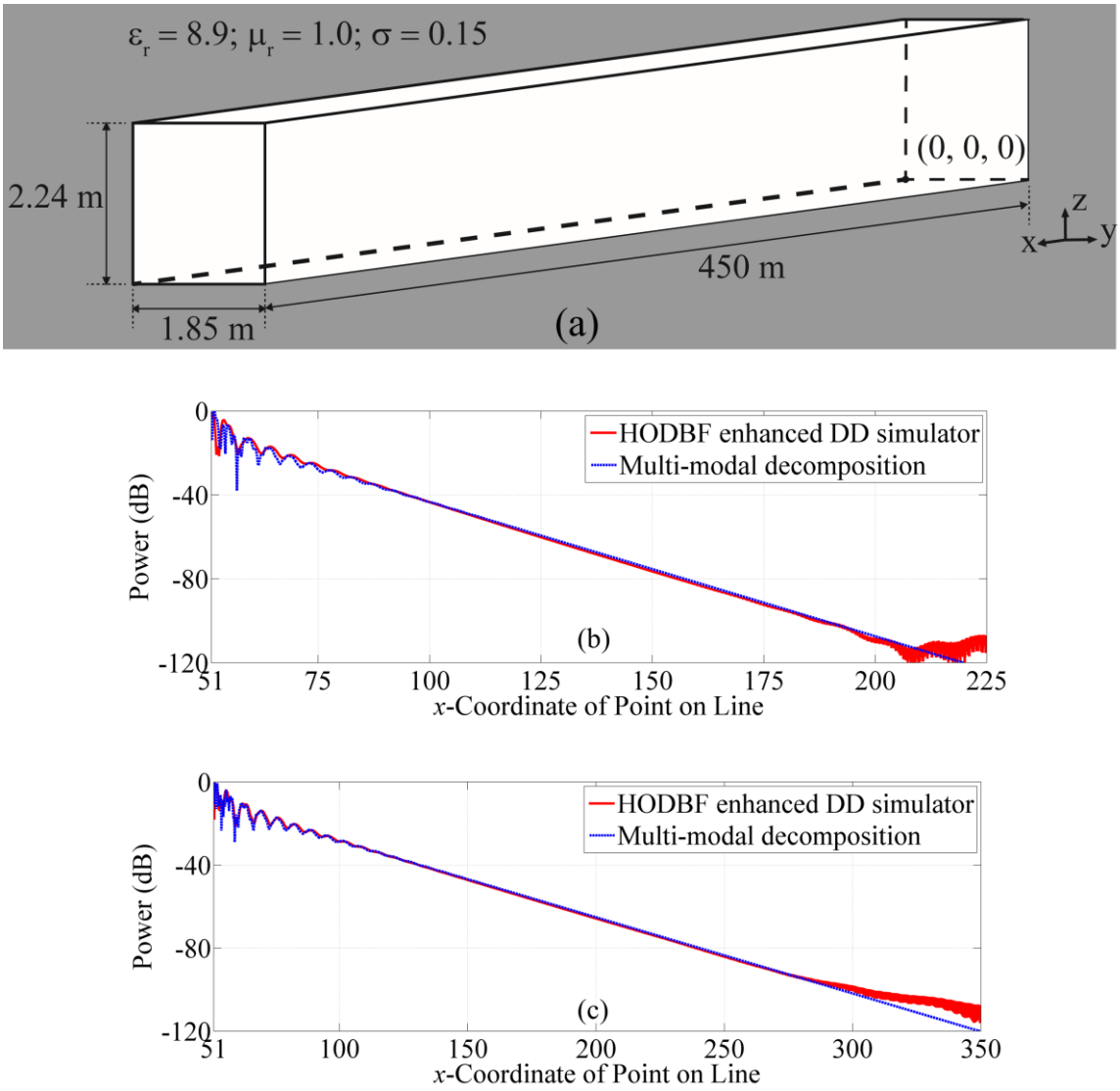

Figure 6.7 (a) Geometry of a 450-m rectangular tunnel. Power values computed by the enhanced DD simulator and multi-modal decomposition at (b) 455 MHz and (c) 600 MHz.

6.4.2.2 Arched Tunnels

A 600 m - long arched tunnel is excited by a $z-$ (vertically) oriented dipole at 455 MHz [Figure 6.8 (a)]. In this scenario, the tunnel is decomposed into 200 identical 3 m - long subdomains for analysis and only one scattering matrix is computed for each

frequency. Subdomains are discretized using 50202 RWG basis functions, while the equivalent surfaces are discretized using 12958 RWG basis functions. Power values on a line connecting (51.2, 0.915, 1.22) m and (600, 0.915, 1.22) m computed by the proposed simulator are compared with the measurement data [67, 68] after applying the normalizations accounting for different excitation mechanism [Figure 6.8 (b)]. Power values computed by the enhanced DD based SIE simulator are in good agreement with the measurement data, again demonstrating the accuracy of the simulator. The dynamic ranges of the simulator are around 120 dB and are reflected in Figure 6.8 (b).

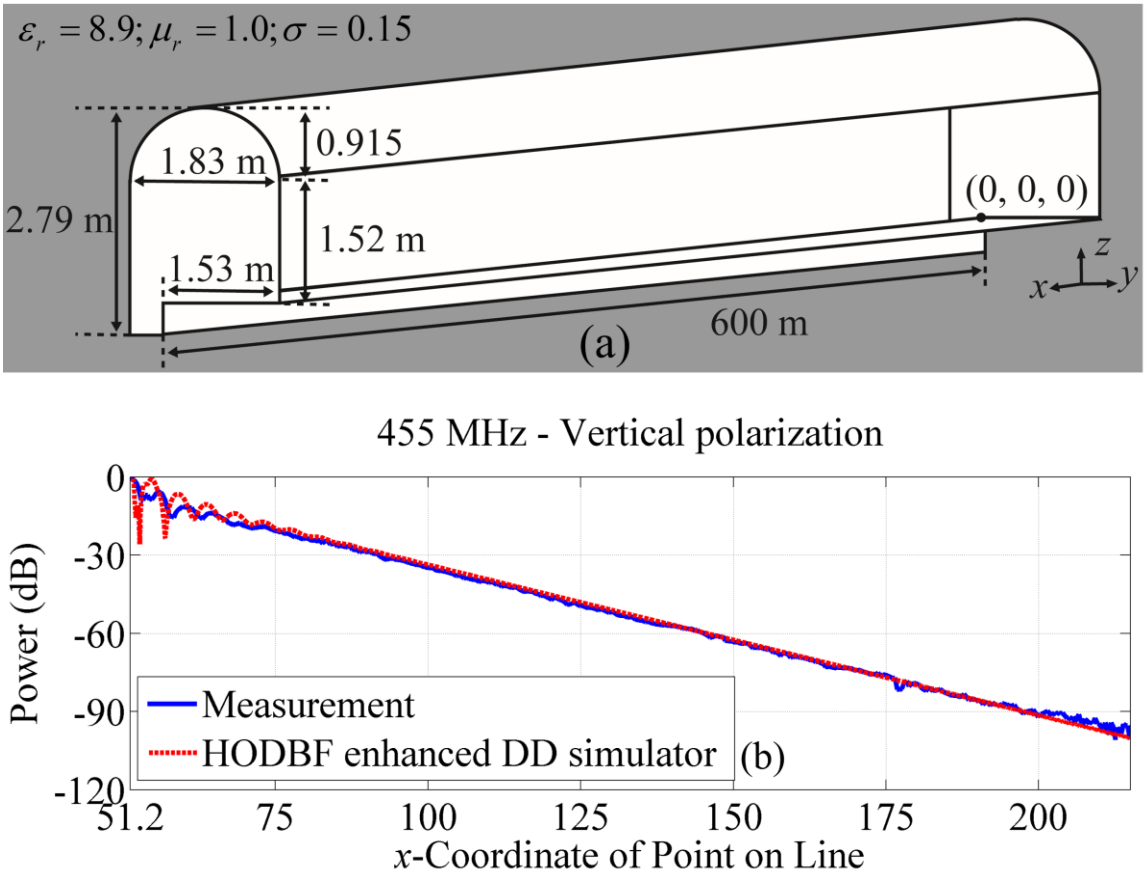

Figure 6.8 (a) Geometry of a 600-m arched tunnel. (b) Power values computed by the enhanced DD simulator and obtained from measurement data.

6.5 Chapter Conclusion

A HODBF method is proposed to compress the scattering matrices in the DD based SIE simulator in a hierarchically butterfly compressed format and reduce the CPU and memory requirements for the iterative solution of inter-domain system solved by the DD simulator. Numerical results demonstrate that the proposed HODBF enhancement of the DD simulator achieves significant improvement over its predecessors for characterizing EM wave propagations in mine tunnels with electrically large cross sections.

CHAPTER 7
Conclusions

7.1 Summary

This thesis presents an EM framework that can efficiently and accurately perform optimizations and uncertainty quantifications for communication systems in realistic and electrically large mine environments.

First, a fast FMM-FFT-SIE simulator for analyzing EM wave propagation in electrically large and realistically loaded mine environments is presented. The simulator leverages Muller and combined field SIEs to model scattering from mine walls and perfect electrically conducting (PEC) objects residing inside mine tunnels and galleries. A FMM-FFT acceleration scheme is used to accelerate the computation. It also uses singular value and Tucker decomposition to reduce the memory requirements of the simulator.

Second, a DD based SIE simulator tailored for efficiently analyzing EM wave propagation in large mine environments with multiple excitations is presented. It alleviates the computational burden of full wave EM simulators by dividing the mine tunnels or galleries into subdomains that are characterized separately and constructing an

inter-domain system assembling the solutions of subdomains. The inter-domain system can be efficiently solved by judiciously combining subdomains. The simulator can be more than 10 times faster than traditional EM simulators such as FMM-FFT-SIE simulator when used to solve problems with multiple excitations.

Third, a DIRECT optimization algorithm is presented and incorporated with the DD based SIE simulator for efficient optimization and/or reconfiguration of wireless communication networks in mine environments. The DIRECT algorithm is a modified version of Lipschitzian optimization methods and is efficient for wireless network optimizations. Numerical results demonstrated that the optimization framework can efficiently and reasonably place transmitters in a mine environment.

Next, a HDMR-MEPC uncertainty quantification scheme is presented and incorporated with the two EM simulators in previous chapters. The HDMR-MEPC scheme permits the accurate and efficient construction of surrogate models for EM observables in high dimensions. Numerical results demonstrated the efficiency and accuracy of the UQ framework.

Finally, a HODBF matrix compression scheme is applied to the DD based SIE simulator for rapid mathematical operations of the scattering matrix computed for each subdomain. HODBF scheme can efficiently and accurately compress the scattering matrix and reduce the computational complexity of matrix-vector multiplications.

7.2 Future Work

The current HODBF scheme is serially implemented and hence unable to compress very large scattering matrices that are inevitable when analyzing EM problems in high frequencies. Hence, the HODBF scheme will be parallelized and incorporated with the DD based SIE simulator to characterize EM wave propagations for high-frequency wireless communication systems (such as WLAN systems) in large mine environments. On the other hand, the current HODBF method only achieves $O(N_p^{1.25}\log^2 N_p)$ CPU and memory complexities when applying the HODBF compressed scattering matrices to matrix vector multiplications. It can be further reduced to $O(N_p \log^2 N_p)$ by using other hierarchical matrix structures, or the butterfly plus scheme. The implementation of the butterfly plus scheme to the HODBF structure will be investigated. Other applications of the two efficient EM simulators are also being researched.

7.3 Contributions

The following journal papers and conference papers/abstracts related to the work presented in this thesis are either published, submitted, or currently being prepared.

7.3.1 Journal Papers

[1] W. Sheng, A. C. Yucel, Yang Liu, Han Guo, and E. Michielssen, “A Domain Decomposition based Surface Integral Equation Simulator for Characterizing EM Wave Propagation in Mine Environments”, in preparation

[2] W. Sheng, A. C. Yucel, Yang Liu, Han Guo, and E. Michielssen, “Optimization of Wireless Communication Network in Mine Environments Using Full Wave EM Simulator”, in preparation

[3] A. C. Yücel, W. Sheng, C. Zhou, Y. Liu, H. Bağcı, and E. Michielssen, "An FMM-FFT Accelerated SIE Simulator for Analyzing EM Wave Propagation in Mine Environments Loaded with Conductors," *IEEE J. Multiscale Multiphys. Comput. Tech.,* under review.

7.3.2 Conference Papers

[1] W. Sheng, A. C. Yucel, and E. Michielssen, “Optimization of Wireless Network Configurations in Mine Environments,” in *Proc CNC-USNC/URSI National Radio Sci. Meet.,* 2016

[2] W. Sheng, A. C. Yucel, and E. Michielssen, “A Domain Decomposition based Surface Integral Equation Solver for Characterizing Electromagnetic Wave Propagation in Mine Environments”, in *Proc. IEEE Int. Symp. Antennas Propagat.,* 2016.

[3] L. J. Gomez, W. Sheng, A. C. Yucel, and E. Michielssen, “Fast Statistical Characterization of Rough Surface Scattering via Tensor Train Decompositions”, in *Proc CNC-USNC/URSI National Radio Sci. Meet.,* 2016

[4] W. Sheng, Han Guo, Yang Liu, A. C. Yucel, and E. Michielssen, “A Butterfly-Based Domain Decomposition SIE Simulator for EM Analysis of Wireless Communication Systems in Mine Environments”, in *Proc CNC-USNC/URSI National Radio Sci. Meet.,* 2017

[5] W. Sheng, A. C. Yucel, and E. Michielssen, “Tucker Compressed Muller-SIE for EM Analysis of Mine Communication Systems,” in *Proc CNC-USNC/URSI National Radio Sci. Meet.*, 2017

REFERENCES

[1] A. E. Forooshani, S. Bashir, D. G. Michelson, and S. Noghanian, "A survey of wireless communications and propagation modeling in underground mines," *IEEE Commun. Surveys Tuts.*, vol. 15, pp. 1524-1545, 2013.

[2] "Mine Improvement and New Emergency Response Act of 2006 (MINER Act)," ed: Pub. L. No. 108-236 (S 2803), 2006.

[3] A. Emslie, R. Lagace, and P. Strong, "Theory of the propagation of UHF radio waves in coal mine tunnels," *IEEE Trans. Antennas Propag.*, vol. 23, pp. 192-205, 1975.

[4] Z. Sun and I. F. Akyildiz, "Channel modeling and analysis for wireless networks in underground mines and road tunnels," *IEEE Trans. Commun.*, vol. 58, pp. 1758-1768, 2010.

[5] S. F. Mahmoud and J. R. Wait, "Geometrical optical approach for electromagnetic wave propagation in rectangular mine tunnels," *Radio Sci.*, vol. 9, pp. 1147–1158, 1974.

[6] D. Didascalou, T. M. Schfer, F. Weinmann, and W. Wiesbeck, "Ray density normalization for ray-optical wave propagation modeling in arbitrarily shaped tunnels," *IEEE Trans. Antennas Propag.*, vol. 48, pp. 1316-1325, 2000.

[7] Y. Hwang, Y. P. Zhang, and R. G. Kouyoumjian, "Ray-optical prediction of radio-wave propagation characteristics in tunnel environments-Part 1:Theory," *IEEE Trans. Antennas Propag.*, vol. 46, pp. 1328–1336, 1998.

[8] M. Ndoh, G. Y. Delisle, and R. Le, "A novel approach to propagation prediction in confined and diffracting rough surfaces," *Int. J. Numer. Model.*, vol. 16, pp. 535–555, 2003.

[9] L. Ramirez, F. Hasselmann, and Y. Zhang, "Channel characteristics in tunnels: FDTD simulations and measurement," *J. Microw. Opt. Electromag. Appl.,* vol. 10, pp. 121-130, 2011.

[10] G. S. Ching, K. Tsuda, and Y. Kishiki, "Analysis of path gain inside tunnels based on FDTD and ray tracing methods," presented at the Proc. Int. Symp. EM Theory, 2013.

[11] Y. Wu, M. Lin, and I. J. Wassell, "Modified 2D finite-difference timedomain based tunnel path loss prediction for wireless sensor network applications," *J. Commun.,* vol. 4, pp. 214–223, 2009.

[12] M. F. Hadi and S. F. Mahmoud, "Modeling wireless propagation in a rectangular tunnel with the compact-FDTD method," presented at the Proc. IEEE RWS, 2008.

[13] D. E. Brocker, P. E. Sieber, P. L. Werner, and D. H. Werner, "A hybrid approach for large-scale optimizations of medium frequency propagation in coal mines," presented at the Proc. IEEE Int. Symp. Antennas Propagat., 2011.

[14] K. Deb, A. Pratap, S. Agarwal, and T. Meyarivan, "A fast and elitist multiobjective genetic algorithm: NSGA-II," *IEEE Trans. Evol. Comput.,* vol. 6, pp. 182-197, 2002.

[15] J. Kennedy, "Particle swarm optimization," in *Encyclopedia of machine learning*, ed: Springer, 2011, pp. 760-766.

[16] R. W. Wedderburn, "Quasi-likelihood functions, generalized linear models, and the Gauss—Newton method," *Biometrika,* vol. 61, pp. 439-447, 1974.

[17] N. K. Georgieva, S. Glavic, M. H. Bakr, and J. W. Bandler, "Feasible adjoint sensitivity technique for EM design optimization," *IEEE Trans. Microwave Theory Tech.,* vol. 50, pp. 2751-2758, 2002.

[18] J. A. Nelder and R. Mead, "A Simplex Method for Function Minimization," *The Computer Journal,* vol. 7, pp. 308-313, 1965.

[19] R. Hooke and T. A. Jeeves, "`` Direct Search" Solution of Numerical and Statistical Problems," *J. ACM,* vol. 8, pp. 212-229, 1961.

[20] D. E. Finkel, "DIRECT optimization algorithm user guide," Center for Research in Scientific Computation, North Carolina State University2003.

[21] J. M. Gablonsky, "Modifications of the DIRECT Algorithm," Ph.D. Thesis, Department of Mathematics, North Carolina State University, 2001.

[22] D. R. Jones, C. D. Perttunen, and B. E. Stuckman, "Lipschitzian optimization without the Lipschitz constant," *J. Optim. Theory Appl.,* vol. 79, pp. 157-181, 1993.

[23] D. Xiu and G. E. Karniadakis, "The Wiener--Askey polynomial chaos for stochastic differential equations," *SIAM J. Sci. Comput.,* vol. 24, pp. 619-644, 2002.

[24] A. C. Yucel, H. Bagci, and E. Michielssen, "An adaptive multi-element probabilistic collocation method for statistical EMC/EMI characterization," *IEEE Trans. Electromagn. Compat.,* vol. 55, pp. 1154-1168, 2013.

[25] A. C. Yücel, H. Bağcı, and E. Michielssen, "An ME-PC enhanced HDMR method for efficient statistical analysis of multiconductor transmission line networks," *IEEE Trans. Compon. Packag. Manuf. Technol.,* vol. 5, pp. 685-696, 2015.

[26] A. E. Forooshani, S. Bashir, D. G. Michelson, and S. Noghanian, "A survey of wireless communications and propagation modeling in underground mines," *IEEE Commun. Surv. Tutorials,* vol. 15, pp. 1524-1545, 2013.

[27] R. L. Wagner, S. Jiming, and W. C. Chew, "Monte Carlo simulation of electromagnetic scattering from two-dimensional random rough surfaces," *IEEE Trans. Antennas Propagat.,* vol. 45, pp. 235-245, 1997.

[28] C. Waltz, K. Sertel, M. A. Carr, B. C. Usner, and J. L. Volakis, "Massively parallel fast multipole method solutions of large electromagnetic scattering problems," *IEEE Trans. Antennas Propagat.,* vol. 55, pp. 1810-1816, 2007.

[29] A. C. Yucel, L. J. Gomez, and E. Michielssen, "Compression of translation operator tensors in FMM-FFT accelerated SIE solvers via Tucker decomposition," *IEEE Antennas Wireless Propag. Lett.,* (in press), 2017.

[30] C. Müller, *Foundations of the mathematical theory of electromagnetic waves* vol. 155: Springer Science & Business Media, 2013.

[31] S. M. Rao, D. R. Wilton, and A. W. Glisson, "Electromagnetic scattering by surfaces of arbitrary shape," *IEEE Trans. Antennas Propagat.,* vol. 30, pp. 409-418, May 1982.

[32] W. C. Chew, E. Michielssen, J. M. Song, and J. M. Jin, *Fast and efficient algorithms in computational electromagnetics*. Norwood, MA, USA: Artech House, Inc., 2001.

[33] J. M. Taboada, L. Landesa, F. Obelleiro, J. L. Rodriguez, J. M. Bertolo, M. G. Araujo, *et al.*, "High scalability FMM-FFT electromagnetic solver for

supercomputer systems," *IEEE Antennas Propagat. Mag.,* vol. 51, pp. 20-28, 2009.

[34] L. D. Lathauwer, B. D. Moor, and J. Vandewalle, "A multilinear singular value decomposition," *SIAM J. Matrix Anal. Appl.,* vol. 21, pp. 1253-1278, 2000.

[35] T. G. Kolda and B. W. Bader, "Tensor decompositions and applications," *SIAM Rev.,* vol. 51, pp. 455-500, 2009.

[36] R. W. Freund, "A Transpose-Free Quasi-Minimal Residual Algorithm for Non-Hermitian Linear Systems," *SIAM J. Sci. Comput.,* vol. 14, pp. 470-482, 1993.

[37] L. Tsang, J. A. Kong, K.-H. Ding, and C. O. Ao, *Scattering of electromagnetic waves, numerical simulations*. John Wiley & Sons, 2004.

[38] A. Emslie, R. Lagace, and P. Strong, "Theory of the propagation of UHF radio waves in coal mine tunnels," *IEEE Trans. Antennas Propagat.,* vol. 23, pp. 192-205, 1975.

[39] Z. Sun and I. F. Akyildiz, "Channel modeling and analysis for wireless networks in underground mines and road tunnels," *IEEE Trans. Commun.,* vol. 58, pp. 1758-1768, 2010.

[40] D. Didascalou, T. Schafer, F. Weinmann, and W. Wiesbeck, "Ray-density normalization for ray-optical wave propagation modeling in arbitrarily shaped tunnels," *IEEE Trans. Antennas Propagat.,* vol. 48, pp. 1316-1325, 2000.

[41] Y. Hwang, Y. P. Zhang, and R. G. Kouyoumjian, "Ray-optical prediction of radio-wave propagation characteristics in tunnel environments. 1. Theory," *IEEE Trans. Antennas Propagat.,* vol. 46, pp. 1328-1336, 1998.

[42] S. F. Mahmoud and J. R. Wait, "Geometrical optical approach for electromagnetic wave propagation in rectangular mine tunnels," *Radio Sci.,* vol. 9, pp. 1147-1158, 1974.

[43] M. F. Hadi and S. F. Mahmoud, "Modeling wireless propagation in a rectangular tunnel with the compact-FDTD method," in *Proc. IEEE RWS*, 2008, pp. 339-342.

[44] L. Ramirez, F. Hasselmann, and Y. Zhang, "Channel characteristics in tunnels: FDTD simulations and measurement," *J. Microw. Opt. Electromag. Appl.,* vol. 10, pp. 121-130, 2011.

[45] Y. Wu, M. Lin, and I. J. Wassell, "Modified 2D finite-difference time-domain based tunnel path loss prediction for wireless sensor network applications," *J. Commun.,* vol. 4, pp. 214-223, 2009.

[46] G. S. Ching, K. Tsuda, and Y. Kishiki, "Analysis of path gain inside tunnels based on FDTD and ray tracing methods," in *Proc. Int. Symp. EM Theory*, 2013, pp. 644-647.

[47] D. E. Brocker, P. E. Sieber, P. L. Werner, and D. H. Werner, "A hybrid approach for large-scale optimizations of medium frequency propagation in coal mines," in *Proc. IEEE Int. Symp. Antennas Propagat.*, 2011, pp. 2391-2394.

[48] O. Bakir, A. C. Yucel, E. Michielssen, and H. Bagci, "Statistical characterization of wave propagation in mine environments," in *Proc. IEEE Int. Symp. Antennas Propagat.*, 2012, pp. 1-2.

[49] A. C. Yücel, Y. Liu, H. Bağcı, and E. Michielssen, "An FMM-FFT accelerated integral equation solver for characterizing electromagnetic wave propagation in mine tunnels and galleries loaded with conductors," in *Proc. CNC-USNC/URSI National Radio Sci. Meet.*, 2014, pp. 65-65.

[50] A. C. Yücel, W. Sheng, C. Zhou, Y. Liu, H. Bağcı, and E. Michielssen, "An FMM-FFT Accelerated SIE Simulator for Analyzing EM Wave Propagation in Mine Environments Loaded with Conductors," *IEEE J. Multiscale Multiphys. Comput. Tech.*, under review.

[51] A. C. Yücel, Y. Liu, H. Bağci, and E. Michielssen, "Statistical Characterization of Electromagnetic Wave Propagation in Mine Environments," *IEEE Antennas Wireless Propagat. Lett.*, vol. 12, pp. 1602-1605, 2013.

[52] W. Sheng, A. C. Yücel, and E. Michielssen, "Optimization of wireless network configurations in mine environments," in *Proc. CNC-USNC/URSI National Radio Sci. Meet.*, 2016.

[53] H. Guo, Y. Liu, J. Hu, and E. Michielssen, "A Butterfly-Based Direct Integral-Equation Solver Using Hierarchical LU Factorization for Analyzing Scattering From Electrically Large Conducting Objects," *IEEE Trans. Antennas Propagat.*, vol. 65, pp. 4742-4750, 2017.

[54] A. C. Yücel, "Uncertainty Quantification for Electromagnetic Analysis via Efficient Collocation Methods," Ph.D. Thesis, EECS Department, University of Michigan, Ann Arbor, MI, 2013.

[55] A. C. Yücel, L. J. Gomez, and E. Michielssen, "Compression of Translation Operator Tensors in FMM-FFT-Accelerated SIE Solvers via Tucker Decomposition," *IEEE Antennas Wireless Propagat. Lett.*, vol. 16, pp. 2667-2670, 2017.

[56] Z. Peng, K.-H. Lim, and J.-F. Lee, "Nonconformal domain decomposition methods for solving large multiscale electromagnetic scattering problems," *Proc. IEEE,* vol. 101, pp. 298-319, 2013.

[57] M. K. Li, W. C. Chew, and L. J. Jiang, "A domain decomposition scheme based on equivalence theorem," *Microwave Opt. Technol. Lett.,* vol. 48, pp. 1853-1857, 2006.

[58] M.-K. Li and W. C. Chew, "Multiscale simulation of complex structures using equivalence principle algorithm with high-order field point sampling scheme," *IEEE Trans. Antennas Propagat.,* vol. 56, pp. 2389-2397, 2008.

[59] C.-C. Lu and W. C. Chew, "The use of Huygens' equivalence principle for solving 3-D volume integral equation of scattering," *IEEE Trans. Antennas Propagat.,* vol. 43, pp. 500-507, 1995.

[60] M. A. Jensen and J. D. Freeze, "A recursive Green's function method for boundary integral analysis of inhomogeneous domains," *IEEE Trans. Antennas Propagat.,* vol. 46, pp. 1810-1816, 1998.

[61] H. Shao, J. Hu, Z.-P. Nie, G. Han, and S. He, "Hybrid tangential equivalence principle algorithm with MLFMA for analysis of array structures," *Prog. Electromagn. Res.,* vol. 113, pp. 127-141, 2011.

[62] P. Ylä-Oijala and M. Taskinen, "Electromagnetic scattering by large and complex structures with surface equivalence principle algorithm," *Waves Random Complex Medium,* vol. 19, pp. 105-125, 2009/02/11 2009.

[63] A. Barka and P. Caudrillier, "Domain decomposition method based on generalized scattering matrix for installed performance of antennas on aircraft," *IEEE Trans. Antennas Propagat.,* vol. 55, pp. 1833-1842, 2007.

[64] S. Rao, D. Wilton, and A. Glisson, "Electromagnetic scattering by surfaces of arbitrary shape," *IEEE Trans. Antennas Propagat.,* vol. 30, pp. 409-418, 1982.

[65] W. C. Chew, E. Michielssen, J. Song, and J.-M. Jin, *Fast and efficient algorithms in computational electromagnetics*: Artech House, Inc., 2001.

[66] E. Michielssen and A. Boag, "A multilevel matrix decomposition algorithm for analyzing scattering from large structures," *IEEE Trans. Antennas Propagat.,* vol. 44, pp. 1086-1093, 1996.

[67] C. Zhou and J. Waynert, "The equivalence of the ray tracing and modal methods for modeling radio propagation in lossy rectangular tunnels," *IEEE Antennas Wireless Propagat. Lett.,* vol. 13, pp. 615-618, 2014.

[68] C. Zhou, J. Waynert, T. Plass, and R. Jacksha, "Attenuation constants of radio waves in lossy-walled rectangular waveguides," *Prog. Electromagn. Res.*, vol. 142, pp. 75-105, 2013.

[69] N. Garcia and E. Stoll, "Monte Carlo calculation for electromagnetic-wave scattering from random rough surfaces," *Phys. Rev. Lett.*, vol. 52, p. 1798, 1984.

[70] W. Sheng, E. Michielssen, and A. C. Yücel, "A domain decomposition based surface integral equation solver for characterizing electromagnetic wave propagation in mine environments," in *Proc. IEEE Int. Symp. Antennas Propagat.*, 2016, pp. 45-46.

[71] H. D. Sherali, C. M. Pendyala, and T. S. Rappaport, "Optimal location of transmitters for micro-cellular radio communication system design," *IEEE J. Sel. Areas Commun.*, vol. 14, pp. 662-673, 1996.

[72] S. J. Fortune, D. M. Gay, B. W. Kernighan, O. Landron, R. A. Valenzuela, and M. H. Wright, "WISE design of indoor wireless systems: practical computation and optimization," *IEEE Comput. Sci. Eng.*, vol. 2, pp. 58-68, 1995.

[73] M. H. Wright, "Optimization methods for base station placement in wireless applications," in *Vehicular Technology Conference, 1998. VTC 98. 48th IEEE*, 1998, pp. 387-391.

[74] Z. Yun, S. Lim, and M. F. Iskander, "An integrated method of ray tracing and genetic algorithm for optimizing coverage in indoor wireless networks," *IEEE Antennas Wireless Propagat. Lett.*, vol. 7, pp. 145-148, 2008.

[75] J. He, A. A. Verstak, L. T. Watson, C. A. Stinson, N. Ramakrishnan, C. A. Shaffer, *et al.*, "Globally optimal transmitter placement for indoor wireless communication systems," *IEEE Trans. Wireless Commun.*, vol. 3, pp. 1906-1911, 2004.

[76] L. Zhang, G. Barakat, and A. Yassine, "Design and optimal sizing of hybrid PV/wind/diesel system with battery storage by using DIRECT search algorithm," in *2012 15th Int. EPE/PEMC*, 2012, pp. DS3b. 19-1-DS3b. 19-7.

[77] S. E. Cox, R. T. Haftka, C. A. Baker, B. Grossman, W. H. Mason, and L. T. Watson, "A comparison of global optimization methods for the design of a high-speed civil transport," *J. Global Optim.*, vol. 21, pp. 415-432, 2001.

[78] B. O. Shubert, "A sequential method seeking the global maximum of a function," *SIAM J. Numer. Anal.*, vol. 9, pp. 379-388, 1972.

[79] J. M. Gablonsky and C. T. Kelley, "A locally-biased form of the DIRECT algorithm," *J. Global Optim.*, vol. 21, pp. 27-37, 2001.

[80] B. Svensson, N. K. Nia, F. Danielsson, and B. Lennartson, "Sheet-metal press line parameter tuning using a combined DIRECT and Nelder-Mead algorithm," in *2011 IEEE 16th Conf. on ETFA*, 2011, pp. 1-8.

[81] "MATLAB R2014a," ed: The MathWorks, Natick, 2014.

[82] L. J. Gomez, A. C. Yücel, L. Hernandez-Garcia, S. F. Taylor, and E. Michielssen, "Uncertainty Quantification in Transcranial Magnetic Stimulation via High-Dimensional Model Representation," *IEEE Trans. Biomed. Eng.*, vol. 62, pp. 361-372, 2015.

[83] Z. Gao and J. S. Hesthaven, "On ANOVA expansions and strategies for choosing the anchor point," *Appl. Math. Comput.*, vol. 217, pp. 3274-3285, 2010/12/01/ 2010.

[84] I. M. Sobol, "Theorems and examples on high dimensional model representation," *Reliab. Eng. Syst. Saf.*, vol. 79, pp. 187-193, 2003/02/01/ 2003.

[85] Z. Zhang, M. Choi, and G. E. Karniadakis, "Anchor Points Matter in ANOVA Decomposition," in *Spectral and High Order Methods for Partial Differential Equations: Selected papers from the ICOSAHOM '09 conference, June 22-26, Trondheim, Norway*, J. S. Hesthaven and E. M. Rønquist, Eds., ed Berlin, Heidelberg: Springer Berlin Heidelberg, 2011, pp. 347-355.

[86] F. Zhang, "Analysis of antenna radiation characteristics in mine tunnels," in *Proceedings of the 9th International Symposium on Antennas, Propagation and EM Theory*, 2010, pp. 327-330.

[87] X. Yang, S. Feng, X. Zhang, X. Ren, and W. Li, "Research of Single Mode Radiation Leaky Coaxial Cable Used for Ultra Wide-band Communication," in *2006 International Conference on Communications, Circuits and Systems*, 2006, pp. 1261-1264.

[88] J. H. Wang and K. K. Mei, "Theory and analysis of leaky coaxial cables with periodic slots," *IEEE Trans. Antennas Propagat.*, vol. 49, pp. 1723-1732, 2001.

[89] S. P. Morgan, "Prediction of indoor wireless coverage by leaky coaxial cable using ray tracing," *IEEE Trans. Veh. Technol.*, vol. 48, pp. 2005-2014, 1999.

[90] *Advanced Tutorial on Wireless Communication and Electronic Tracking*. Available:

https://www.cdc.gov/niosh/mining/content/emergencymanagementandresponse/commtracking/advcommtrackingtutorial1.html

[91] Y. Liu, H. Guo, and E. Michielssen, "An HSS Matrix-Inspired Butterfly-Based Direct Solver for Analyzing Scattering From Two-Dimensional Objects," *IEEE Antennas Wireless Propagat. Lett.*, vol. 16, pp. 1179-1183, 2017.

[92] S. Ambikasaran, "Fast algorithms for dense numerical linear algebra and applications," Stanford University Stanford, 2013.

[93] M. Tygert, "Fast algorithms for spherical harmonic expansions, III," *J. Comput. Phys.*, vol. 229, pp. 6181-6192, 2010.

[94] E. Michielssen and A. Boag, "Multilevel evaluation of electromagnetic fields for the rapid solution of scattering problems," *Microwave Opt. Technol. Lett.*, vol. 7, pp. 790-795, 1994.

[95] L. Lin, J. Lu, and L. Ying, "Fast construction of hierarchical matrix representation from matrix–vector multiplication," *J. Comput. Phys.*, vol. 230, pp. 4071-4087, 2011.

[96] Y. Liu, H. Guo, and E. Michelssen, "A new butterfly reconstruction method for MLMDA-based direct integral equation solvers," in *Proc. IEEE Int. Symp. AP-S/URSI, 2016*, 2016.